DOI: 10.14750/ME.2023.031

UNIVERSITY OF MISKOLC
FACULTY OF MECHANICAL ENGINEERING AND INFORMATICS

ANALYSIS AND EVALUATION OF COATING CHARACTERISTICS

PHD THESES

Prepared by

Okhunjon Sayfidinov
Mechanical Engineering (BSc),
Mechanical Engineering (MSc)

ISTVÁN SÁLYI DOCTORAL SCHOOL OF MECHANICAL ENGINEERING SCIENCES
TOPIC FIELD OF DESIGN OF MACHINES AND STRUCTURES
TOPIC GROUP OF PRODUCT DEVELOPMENT AND DESIGN

Head of Doctoral School

Dr. Gabriella Bognár
DSc, Full Professor

Head of Topic Group

Dr. Gabriella Bognár
DSc, Full Professor

Scientific Supervisor

Dr. Gabriella Bognár
DSc, Full Professor

Miskolc
2023

DOI: 10.14750/ME.2023.031

CONTENTS

DOI: 10.14750/ME.2023.031

DOI: 10.14750/ME.2023.031

SUPERVISOR'S RECOMMENDATIONS

PhD candidate Okhunjon Sayfidinov has been under my supervision for almost four years. Since September 2019, he has been pursuing his PhD studies at the Institute of Mechanical and Product Design at the Sályi István Sályi School of Mechanical Engineering, part of the Faculty of Mechanical Engineering and Informatics, under the "Stipendium Hungaricum" scholarship programme. His research work on the analysis of the Kardar-Parisi Zhang equation is a very active research area today.

The results of the candidate's research have been published and presented in scientific journals, doctoral seminars, doctoral forums and international conferences, as well as in conference proceedings. His publications have appeared in scientific journals. The work has room for extension, as additional questions that could not be answered within the scope of the PhD training were raised during the work and further results are in the process of being published.

In 2021, he successfully passed the complex examination. He obtained the pre-degree certificate with 292 credits on 24 March 2023. He successfully passed the departmental discussion on 22 March 2023.

The candidate worked independently and very often took the initiative, always following instructions. During his doctoral studies he further developed his knowledge, research affinity and presentation skills. He has acquired new knowledge and competences which he will be able to use in his future academic life.

02 May 2023

Supervisor

DOI: 10.14750/ME.2023.031

LIST OF SYMBOLS AND ABBREVIATIONS

GREEK LETTERS

α and β – growth exponents
γ – roughness exponent
δ - Dirac function
ε – positive infinitesimal value
ζ – similarity variable
$\eta(x,t)$ – noise term
θ – discrete Heaviside function
λ – nonlinear coefficient representing lateral growth
ν – the diffusion coefficient
ξ – growth variance in the surface height
ρ – particle
φ – smooth function
χ – roughness coefficient
ω – variable

LATIN LETTERS

Δt – time interval
Δx – space interval
A – amplitude
a – constant
A_k – coefficient
C – an arbitrary positive value
C_r – comulation function
c_1, c_2 n, c – constants
D – the fractal dimensionality
d – dimension
F – force
g – universal function
H – boundary condition shape
h_t – the space-averaged height
$h(x,t)$ – the height function
$\{h_i\}$ – discrete height configuration
$I_d(\varphi)$, $I_d(\varphi)$ – modified Bessel function
i, j – iteration
K – rescaling factor
L – length
M – number of deposited particle
N – lattice sites number
N_B – border of lattice sites
P – probability distribution
$R(t)$ – uniform distribution
S – surface thickness
Δt – time
v_t – averaged velocity
$W(t)$ – interface width function
x, y – coordinates
Δx – space step
z – diffusion coefficient or saturation exponent

DOI: 10.14750/ME.2023.031

1. INTRODUCTION

One of the successful equations for describing a class of dynamic nonlinear phenomena is the Kardar–Parisi–Zhang (KPZ) equation [1]. The application of this equation varies widely in topics such as vapour deposition, directed polymers, bacterial colony growth and superconductors [2], [3]. There are a number of computational studies related to discrete model simulations such as the Eden model, ballistic deposition models [4] and directed polymer model. All of these provide important features in the physical processes through simulation efficiency. The introduction of direct numerical integration is also an important point that requires more intensive computations. The first large scale numerical integration of the KPZ equation was performed by Amar and Family and the discrete Gaussian model was verified in [5]. Later, Moser improved his accuracy with further works [6], [7]. However, the KPZ equation is not just a nonlinear equation that is applied by a similar method. To verify the theoretical predictions, numerical and analytical investigations are performed for the KPZ equation with correlated noise [8] and with quenched noise in anisotropic media [9], or in reaction–diffusion systems with multiplicative noise [10], for the Kuramato–Shivashisky equation (KS) of flame front propagation [11], [12] and for the epitaxial growth equation [13].

In general, the direct approach to studying the growth equation is numerical integration and it can be seen as the ideal form of the equation that allows us to fully control the investigation. Unfortunately, Newman and Bray [14] reported some disadvantageous properties of the conventional numerical integration scheme, such as instability and an unphysical fixed point. Later works [15], [16] reported that during numerical simulation instability can occur even in the case of small time steps. Lam and Shin [17] found that direct numerical integration by conventional finite difference schemes actually do not approximate the continuum KPZ equation. Previously, Amar and Family [18] integrated a similar equation using a generalized nonlinear term. The scaling behaviour of the KPZ equation was in most cases found to be different from the continuum equation. They even explained the results of their studies on KPZ nonlinear terms combining the effects of noise and nonlinearity.

In the last 30 years, different kinds of numerical methods have been proposed for the KPZ equation. These were implemented with various discretizing formulas of the nonlinear term. However, the diffusion term was mostly handled by the most standard Forward Time Centred Space (FTCS), where the time discretisation is based on the explicit Euler method.

The application of the discrete variational formulation to the KPZ equation has been discussed. An alternative approach to other well-known techniques, the variational analytical

solutions of KPZ were introduced by Wio et al. in [19]–[21] and non-equilibrium potential has been obtained to understand radial growth on a growing domain. In [19], a relation between the real-space discretisation schemes was examined. The authors provided discrete schemes of the KPZ equation, and they discussed the role of the Galilean invariance for discrete representations. In [21], the properties of a functional related to the KPZ equation are investigated. The main result is a path integral scheme; and, the authors defined expressions for the probability of entropy production along a trajectory and they obtained integral fluctuation theorems.

The thermodynamic uncertainty relation for the (1 + 1) dimensional Kardar–Parisi–Zhang equation on a finite spatial interval was considered by Niggeman and Seifert [22]. Numerical simulations compared with theoretical predictions showed convincing agreement.

Cartes et al. [23] studied the analytical laws of the scale-dependent correlation time to follow the expected crossover from the short-distance Edwards–Wilkinson scaling to the universal long-distance Kardar–Parisi–Zhang scaling.

In the work [24], the author reviewed KPZ class growth models to investigate roughness scaling using Cayley trees. Height fluctuations have been shown to be a consequence of boundary effects.

The application and analysis of stochastic surface growth processes allows for the development of devices with desired features made from thin films for both technical and medical uses, such as stents. Aside from controlling the thickness, surface roughness, and porosity of the films, the key to preserving mechanical properties in stent devices that use electro-deposited films is managing the coating process and ensuring proper adhesion..

One may pay attention to two significant challenges with these devices: (1) material failure can occur as a result of ruptures caused by the expansion of fatigue cracks and corrosion processes, and (2) accumulation of material deposits on the devices. The repeated strain of tens of millions of loading cycles can also cause fatigue, which could lead to the fracture or failure of the stent. Fatigue-crack development and fracture toughness [25] are extensively established but yet unknown for many materials. In certain applications of stents, such as ureteral stents, prolonged use can result in the buildup of a biomaterial deposit (microbial biofilm).

While numerous experimental studies have been conducted on stent devices both in vivo and in vitro, only a limited number of theoretical studies exist, and none have specifically focused on the theoretical characterization of the surface properties of these materials [26]. Some studies have examined the surface roughness of various coating materials used in stent devices [27]. Theoretical methods and computational tools for simulation and analysis of materials, which are widely utilized in physics and materials science, have not been utilised. Thin films simulations may be widely used in biomaterials investigation due to their low cost and possible uses in the creation of novel materials.

DOI: 10.14750/ME.2023.031

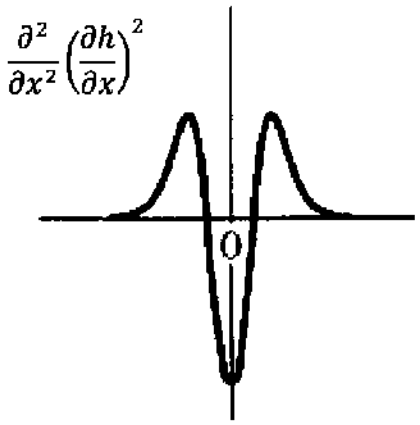

Figure 1.1. Surface segment of the surface [28].

Computational growth models can simulate the fracture of the material in cases of fatigue-crack propagation and cracks, providing insight into the long-term integrity of the stents. Some rupture studies characterize the fragmented material using self-similar notions, and this rupture may be described using directed polymers in random media. The KPZ equation, which gives theoretical insight of the surface, is typically used to map directed polymers in random media [29].

A nonlinear differential equation, unlike the KPZ equation, takes into account nonlinear effects arising from the chemical potential, such as surface diffusion. This equation was initially introduced by Lai and Das Sarma [28], who were inspired by the Molecular Beam Epaxy (MBE) process at high temperatures, where surface diffusion plays a key part in the growth process

$$\frac{\partial h}{\partial t} = \nu\nabla^4 h(x,t) + \lambda\nabla^2(\nabla h)^2 + \eta(x,t). \quad (1.1)$$

As Lai and Das Sarma point out, this Eq.(1.1) takes into consideration surface diffusion and may offer a simplified model for perfect MBE development. The nonlinear expression in one space dimension

$$\frac{\partial^2}{\partial x^2}\left(\frac{\partial h}{\partial x}\right)^2 \quad (1.2)$$

may be understood geometrically as a surface segment, as shown in Fig. 1.1. Eq. (1.2) demonstrates a conserved dynamics with non-conservative noise and is typically represented by the symbol NCN4 (nonlinear conservative dynamics, non-conservative noise) [29]. This equation can be accurately solved using the Renormalization Group analysis, and the exponents for a fractal dimension $d = 2$ are $\alpha = 2/3$, $\beta = 1/5$, and $z = 10/3$.

$$\frac{\partial h}{\partial t}(x,t) = \nu\nabla^2 h + \frac{\lambda}{2}(\nabla h)^2 + \lambda\nabla^2(\nabla h)^2 + F + \eta(x,t). \quad (1.3)$$

The relaxation processes, lateral growth, surface diffusion, and desorption are all taken into consideration in Eq.(1.3).

The mathematical model derived from this equation can serve as a starting point for exploring ultra-thin film coatings with complex properties arising from the film growth process, such as porosity and pinholes. [30]. In terms of medical surface coating applications, such as stent coatings [30], this equation can simulate the process and has potential value in advancing our understanding and improvement of such surface growth. However, since the equation only has exact exponents for one-dimensional cases, additional numerical analysis and simulations are necessary to accurately characterize these processes.

The critical importance of controlling the surface during film deposition is demonstrated by adjusting parameters such as roughness, porosity, and thickness of the films. The use of computer simulations is becoming increasingly useful for precision control, therefore requiring further research to improve thin film deposition techniques and procedures.

DOI: 10.14750/ME.2023.031

2. THE UNIVERSALITY CLASS IN SURFACE GROWTH

2.1. Surface growth universality

The universality class is one of the least studied concepts. It is a quite complex random system that plays major role in research on probability, in statistical mechanics and mathematical physics. There are some findings on studying differences and similarities between ballistic deposition models and the Kardar-Parisi-Zhang universality class in various dimensions [4].

For a long time, the study of surface growth of materials has been a complex area of research. The growth includes a number of disciplines such as microelectronics (growth of nano devices) [31] metallurgy (solidification of alloys), biophysics [32] (growth of proteins, cells and tumours, and cytoskeleton polymerization in the immune system) [33]. These present different problems, obviously in different underlying mechanisms. Therefore, the nature of crystalline is crucial for surface dynamics. Crystalline surfaces exhibit two different structures in the microscale: a rough surface (i) and a smooth or atomically flat surface (ii). Most metals and several organic components are included in the first category, where their melting temperature is reached [34]. In this process, the surface fluctuates strongly, and the concept of a crystalline plane is difficult to define. In the second category, surface atoms or molecules fit perfectly in a smooth atomically flat plane. For example, semiconductors, some metals, and more organic materials fall into this category.

The microscopic nature of the surface is crucial for the physics of crystalline growth. As it presents many unwanted bonds, the addition of new particles to the growing solid is quick for rough solid surface. However, smooth solid or atomically flat solid surface adhesive particles are rare and complicated process. The surface growth can be two-dimensional (2D) caused by adhesion of the atoms to the existing surface layer. This process occurs when cutting a material with poor angle relative to tightly joined plane. It results in two cases those are screw dislocation and vicinal surface. This category is growth problems driven by kinetics. The source phase classified into three prototypes: (i) growth from a solution (this case includes many organic materials, minerals, biological materials, etc.). In this solution, the elementary building blocks diffuse in solution [35] along the surface of the growing material and perform different kinetics, as mentioned above (e.g., nucleation, attachment to pre-existing steps, etc.); (ii) growth from a vapour; and (iii) growth from a beam [36]–[38]. In cases (ii) and (iii), the transport process in the mother phase is not relevant. The latter two categories are ballistic growth or Molecular Beam Epitaxy [39].

The term of ballistic deposition or sticky block was used by Vold [40] in 1959 describing a real growing interface and spatial correlation. The process itself can be presented by blocks that sticks to the first edge against that becomes incident. This process is given in Fig. 2.1 (a, b). It creates overhanging blocks and defines the height function $h(x,t)$ as the maximum height above x occupied by a box in certain time t. Due to radical increase and value of unknown rate of block, an interesting question appears in this deposition model that how this microscopic change manifests itself in certain time.

DOI: 10.14750/ME.2023.031

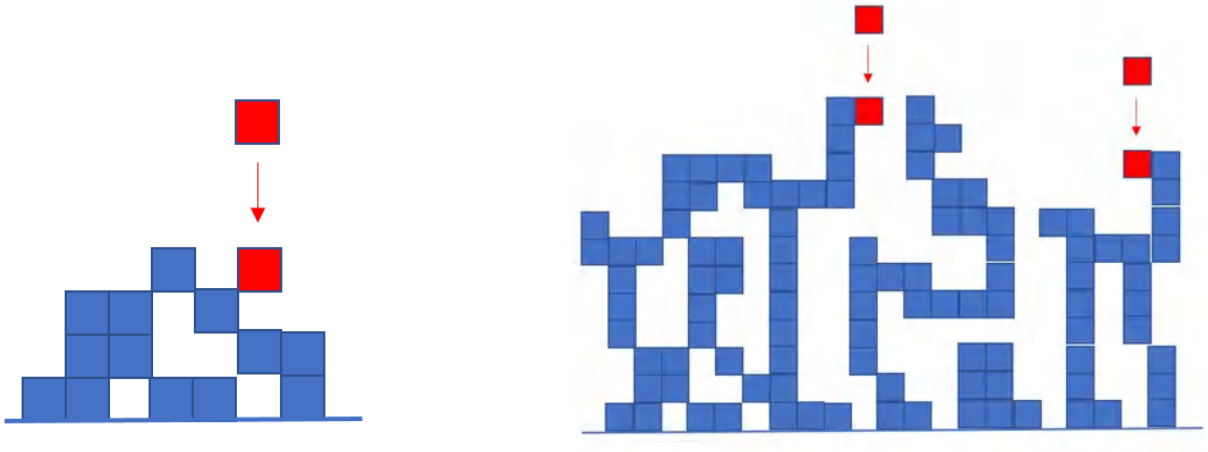

a *b*

Figure 2.1. The result of ballistic deposition models. (a) independently exponentially distributed waiting time, blocks are falling from above. (b) illustrates the result of the deposition model by the same process of falling blocks in longer [32].

The ballistic deposition model is illustrated in Fig. 2.1(a) that in independently exponentially distributed waiting time, blocks are falling from above. Fig. 2.1(b) illustrates the result of the deposition model by the same process of falling blocks in longer time duration. The ballistic deposition model grows considerably faster and smoother top interface than other models [32].

The longer time result that presented in the Fig. 2.2, shows the scale of fluctuations of $u(x,t)$ and the height function $h(x,t)$ remains correlated transversally over a long distance. There are exact conjectures for these fluctuations. They are supposed to grow like $t^{\frac{1}{3}}$ and demonstrate a non-trivial correlation structure in a transversal scale of $t^{\frac{2}{3}}$ [41]. Precise prediction exist to provide the limiting distributions. Until certain constants c_1, and c_2, the sequence of scaled heights

$$c_2 t^{\frac{1}{3}}(h(0,t) - c_1 t) \tag{1.1}$$

should converge as Gaussian Orthogonal Ensemble (GOE) Tracy-Widom random variable. The Tracy-Widom distributions are illustrated as present-time bell curves and are named GOE or GUE (Gaussian Unitary Ensemble) derived from the random matrix ensembles in which these distributions were first observed by Tracy-Widom [42], [43].

It shows the sign of dissimilar integration with a probabilistic system. Apparently, there is a question that how this prediction arises? It came from an analysis of some similar growth processes that happen to be integrable. Ballistic deposition has similar characteristics to these models that are believed to be the key to KPZ class membership [41]:

- Locality: Height function $h(x,t)$ change depends only on neighboring heights.
- Smoothing: Large valleys are quickly filled.
- Non-linear slope dependence: Vertical effective growth rate does not depend linearly on local slope.
- Space-time independent noise: Growth is driven by noise which quickly decorrelates in space/time and is not heavy-tailed.

There is no proof that fully investigated mathematically for the connection between KPZ class solution behavior and the ballistic deposition model. However, the obtained simulation results presented in Fig. 2.1 and Fig. 2.2 suggest that they are in the same class.

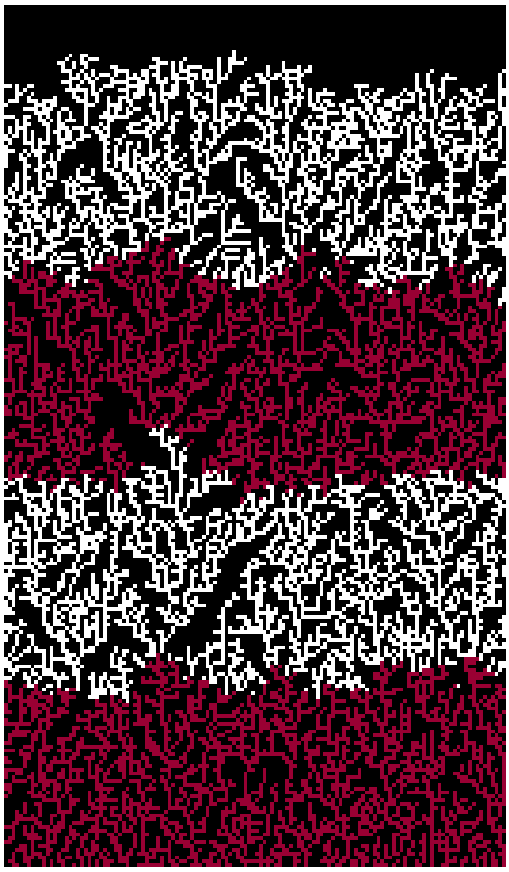

Figure 2.2. Simulation of ballistic deposition models driven by the same process of falling blocks and run for a longer time [41].

The continuum equation that mentioned above is assumed to give the significant dynamics of the ballistic deposition models and it is the famous KPZ equation [1], [38], given in (1+1) dimension by

$$\frac{\partial h}{\partial t}(x,t) = \nu\nabla^2 h(x,t) + \frac{\lambda}{2}(\nabla h)^2 + \eta(x,t), \tag{2.2}$$

where ν is the diffusion coefficient, and λ is nonlinear coefficient representing lateral growth. The noise term is $\eta(x,t)$.

There are currently many suggestions for a direct association between discrete models and continuum equations of motion. There are phenomenological [44] and symmetry, arguments [1], [29], [45], [46] that can be very illuminating. There is also another approach based on the real-space renormalization-group method [47] which can identify relevant microscopic parameters (for example, diffusion) from numerical data when the universality class of the model is already known. Nevertheless, much effort is made to establish a direct relationship between discrete models and continuum equations using formal expansions of discrete equation of motion [48]–[55]. The derivation of the continuum equation is usually based on regularizing and coarse graining

discrete Langevin equations which is taken from a Kramers-Moyal expansion of the master equation. It means that the transition probabilities are calculated from the microscopic rules of the model for any given discrete height configuration $\{h_i\}$ and include the discrete θ (Heaviside) and δ (Dirac) functions. However, the transition probability is presumably a continuous function, requiring some coarse-graining procedure. In detail, this involves expansions of the form

$$\theta(x) = 1 + \sum_{k=1}^{\infty} A_k x^k, \tag{2.3}$$

as initially presented in [56].

There is another suggestion for θ with the following scheme

$$\theta(x) = \frac{1+\tanh(Cx)}{2}, \tag{2.4}$$

where C is an arbitrary positive value with exact $\theta(x)$ function as $C \to \infty$ [26]. Here C is an uncontrolled parameter. In [24], a shifted form is used

$$\theta(x) = \lim_{C\to\infty} \frac{1+\tanh(C\{x+c\})}{2}, \tag{2.5}$$

here $c \in \left(0, \frac{1}{2}\right]$, or using the modified $\arctan(Cx)$ version of [52] or $\mathrm{erf}(Cx)$ [53] instead of $\tan(Cx)$ in Eq.(2.4), in contrast this allows a power expansion that has an infinite radius of convergence [53].

There are some problematic cases with deriving the Kardar-Parisi-Zhang equation from the discrete model known as Ballistic Deposition (BD) [57]. Therefore, a specific case has been developed. The method is based on the discrete Langevin equation. The expansions are used as follows

$$\theta(x-a) = \theta(x) + \sum_{n=1}^{\infty} \frac{a^n}{n} \frac{\partial^n \theta(y)}{\partial y^n}\bigg|_{y=x}. \tag{2.6}$$

Also, closely related Langevin based approach is used to represent the max function [55] in order to reach the KPZ equation from the discrete BD. Recently in [58], using Eq.(2.6), the Edwards-Wilkinson [59]equation was derived from a discrete model using

$$\theta(x) = max\{x+a, 0\} = max\{x\} = \lim_{\varepsilon\to 0^+} \left\{ \frac{\varepsilon}{a} \ln\left[\frac{e^{\left(\frac{x+a}{\varepsilon}\right)}+1}{e^{\frac{x}{\varepsilon}}+1} \right] \right\}, \tag{2.7}$$

where ε is any constant in the interval $(0,1]$.

Despite the new and interesting derivation approach, there are three main drawbacks. They are first implemented in one dimension, where the higher dimensions are not discussed at all or cause particularly high difficulties (see, for example, reference [55]).

The second derivation is an expansion as given in Eq. (2.2) which is a problem because the Heaviside function is certainly not analytic around zero. Another example is to use an expression such as Eq. (2.4) and expand it for small C, while the limiting procedure required to maintain equality requires $C \to \infty$ [43].

The last is that macroscopic quantities (e.g., the diffusion coefficient) cannot be inferred from microscopic rules with artificial parameters such as C and (ϵ), which cannot be removed later. In the paper [60], it was shown that the absence of formal derivation is not accidental, but rather reflects the significant differences between the continuum equation describing the BD model and the KPZ equation. This difference proves to be slight in one-dimension in the presence of noise but it is crucial when discussing deterministic dynamics. However, there is still an open question: first whether the BD model in d dimensions has a proper continuous description that does not depend on the discrete lattice on which it was defined, and how this equation can be derived. The second is whether the BD model belongs to the KPZ universality class in dimensions higher than one or not.

2.2. Eden model

For a long time the geometric scaling properties of structures that grown by ballistic deposition [57] and Eden growth [61] numerially simulated and studied. Interestingly, both structures can be described in the fractal geometry concept [62] and related geometric scaling relationships. The internal structure of both models is uniform on all short length scales (where D is the fractal dimensionality, d is the Euclidean distance). A surface or line growth variance (S) in strip geometry can be described by the scaling form

$$S(M) \sim L^{a} f(h/L^{\frac{\beta}{\alpha}}), \tag{2.8}$$

where $f(x)$ is a scaling function defined by

$$f(x) \sim \begin{cases} x^{\frac{1}{2}} & \text{for } x \ll 1, \\ \text{constant} & \text{for } x \gg 1, \end{cases}$$

initially presented by Family and Vicsek [63] for ballistic deposition and by Julien and Botet [64] for Eden model. The mean height value h is originally flat surface and the width of the strip (or column for $d = 3$) is L. Both ballistic deposition and Eden models were simulated with the same idea in large scale growth that the exponents α and β in Eq. (2.8) are equal [65]–[67]. The values of α and β are $\frac{1}{2}$ and $\frac{1}{3}$ for $d = 2$, respectively. These obtained values are predicted theoretically by the authors [1]. Therefore, the self-affine fractal surfaces of deposits can be described in term of equation (2.8) that generated by ballistic deposition models and Eden growth models, including universal exponents α and β.

Here, discussion concerns with a different aspect of Eden growth and ballistic deposition. The incoming particles sticks to only one particle in the growing deposit for ballistic deposition. The process presents growing trees that is shown in the [40]. Ballistic deposition may occupy more than one nearest neighbour site in lattice models. `

2.3. 1+1 dimension study of finite-size scaling of a ballistic deposition model

In general, the assumption shows that the ballistic deposition model belongs to the KPZ universality class, but it is slow for theoretical predicted values of the exponents $\alpha = \frac{1}{2}$, $\beta = \frac{1}{3}$, and $z = \frac{3}{2}$ [68] which require more larger lattices simulation. The study [64] used finite scaling

and large sampling in order to have rather large lattices with few samples in the simulations. The authors have been focused on the functional size of the various exponents. Finally, only two of the exponents are independent, which we have given above.

In the ballistic deposition model, the interface width is defined by

$$\langle W(t)\rangle = \sqrt{\langle h^2(t)\rangle - \langle h(t)\rangle^2}. \tag{2.9}$$

Thus, the width of the interface follows the scaling function proposed by Family and Vicsek [64], which is defined as:

$$W(t) = L^{\gamma} f\left(\frac{t}{L^z}\right), \tag{2.20}$$

where the scaling function $f(x)$ with $x = t/L^z$ is proportional to $f(x) = x^{\beta}$ for $x \ll 1$ and $f(x) \approx const$ for $x \gg 1$. Here, the exponent γ is the roughness exponent with respect to the saturation of the interface width. The exponent β is the growth exponent and the exponent z is the crossover or saturation exponent. Since the exponent z represents the transition time from the ballistic deposition regime to the saturation regime, it can characterize finite systems. This is more typical for time-dependent rather than equilibrium systems, where correlations are built up and are eventually reduced by the finite size of the system. The analogue equivalent of equilibrium systems occurs at the critical point of the second order phase transition. It can be defined during the growth process that is shown in the Fig. 2.3. The two-dimensional simulation carried in two models in the paper by Meakin [68]. They measured the maximum width (W) and maximum height (h). In the case of 3 dimensional models, the width of projection onto the x -plane was measured.

There were 86 simulations were carried in 2 dimensional model [41] with the 10^7 number of particles for the lengths size $L = 8192$. Simulation were conducted with periodic boundary condition in all simulation results.

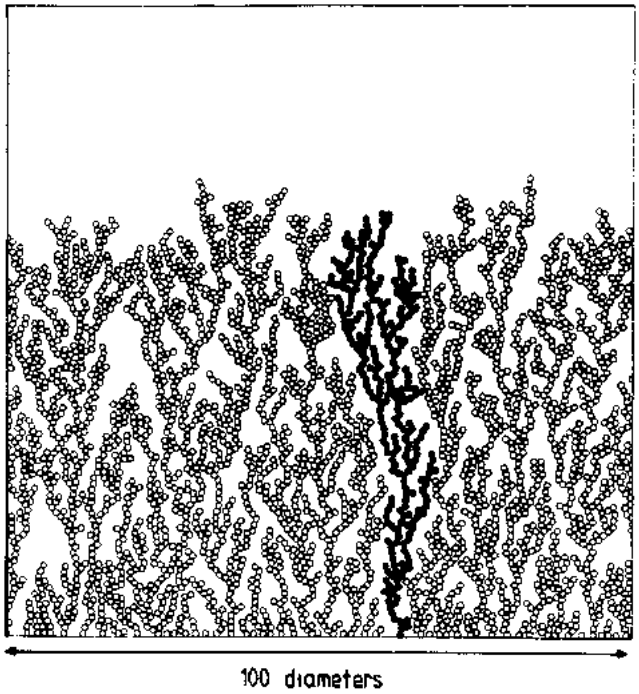

Figure 2.3. Two-dimensional simulation result of ballistic deposition. Emphasized part shows the tree that created by connected particles [68].

There were 86 simulations were carried in 2-dimensional model [68] with the 10^7 number of particles for the lengths size $L = 8192$. Simulation was conducted with periodic boundary condition in all simulation results. The results of the simulation for the width (W) and height (h) had a value of 0.4 and 0.6, respectively. These results are obtained in proved for KPZ equation in our dissertation chapter 6.

Initially, the growth of the interface is dependent on the lattice size and its scaling function that can be described by the proportional relation $t^{\beta}/L^{z\beta}$. This leads to a correlation between the exponents.

$$\alpha = \beta z. \tag{2.31}$$

In [64], the simulation of the ballistic deposition model was performed in the square lattice with different lattices of linear sizes L, which provided a detailed finite size dependence study. Periodic boundary conditions were applied in a direction perpendicular to the incoming flux of the particles. The ballistic deposition model started to saturate at the instant of time t_x, which means crossover time. Equation (2.10) showed that the crossover time is consistent with the relation

$$t_x \infty L^z, \tag{2.42}$$

where the symbol '∞' means 'proportional to'. Relation (2.12) initially increases linearly for $t \ll t_x$ then takes a constant value.

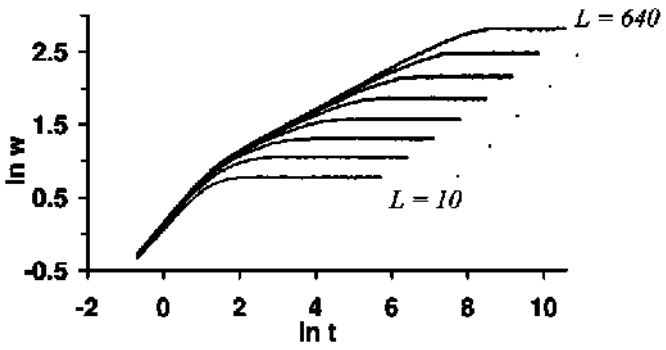

Figure 2.4. Plot of the width vs. time for systems of sizes L as 10, 20, 40, 80, 160, 320, 640, and L_{max} = 1280 lattice constants wide. Smaller sizes saturate at a smaller value of the width [36].

DOI: 10.14750/ME.2023.031

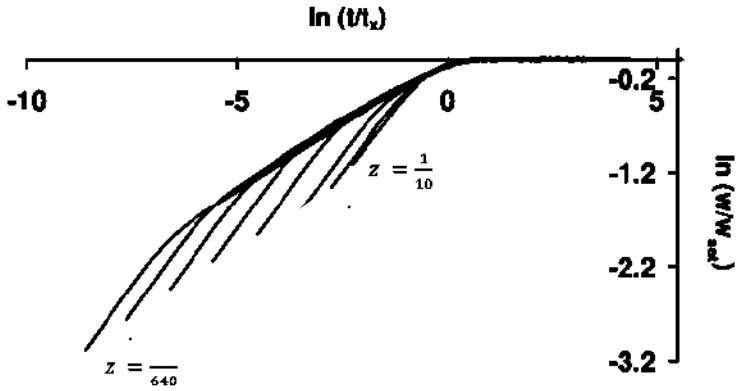

Figure 2.5. Plot of the collapsed scaling function. Tails represent the initial transient behaviour due to a clean substrate between $z_{min} = \frac{1}{640}$ *and* $z_{max} = \frac{1}{10}$ *[37].*

From Eq. (2.12), the characteristic dependence of the crossover time on the size of the system can be observed as well as the fact that the crossover time increases with the size of the system. The crossover time was defined as the time given by the intersection of the straight line describing the saturation regime and the straight line describing the growth regime. In the process of calculating the slope of the latter straight line, there is a transient regime in the initial stages of growth [65]. Figure 2.5 presents the results for exponent z for the same lattice sizes as in Figure 2.4.

The value of the exponent z increases monotonically depending on the size of the system. The absolute value of the local slope increases by $\frac{1}{L} \to 0$ but asymptotic limit of indication has not been reached yet. Since the exponent β characterizes the growth of the interface for finite system size in early times, we can understand from [63] that smaller lattice constants lead to a non-monotonic approach to the asymptotic value. Although the conservative value $\beta \geq 0.30$ can be obtained by extrapolation, it is not clear whether it can converge to the value 0.3 [66] predicted by the KPZ universality class. Later the system had time to grow lateral correlations much longer than its own linear size, but since the spatial correlations are limited by the size of the system, it showed that the system has a natural length scale, the saturation width of the interface. Because of Eq. (2.10) and Fig. 2.4, we expect the value of the saturated width of the interface to scale as L^{α}. As with previous quantities the roughness exponent α did not saturate. It is also instructive to observe the value of the exponent α given from Eq. (2.11). The value of α is taken from βz for a given size of the system. Again, the results do not converge to the asymptotic values. Finally, the values of the z and exponent α have also to satisfy the following scaling relation

$$z + \alpha = 2, \tag{2.53}$$

thus, this quantity is plotted for various system sizes. Again, we can observe that the sum of two values is far from being achieved through the trend in the right direction. (See Fig. 2.7).

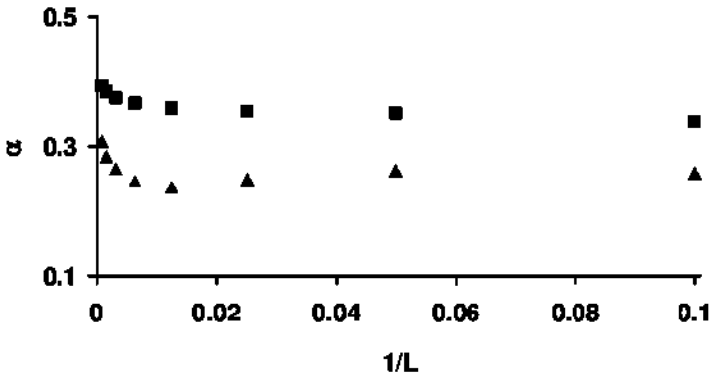

Figure 2.6. Plot of the roughness exponent, α, vs. $1/L$ for the same system sizes referred to in Figure 2.4. Filled triangles are calculated using Eq.(2.11), while filled rectangles are the values directly calculated [36].

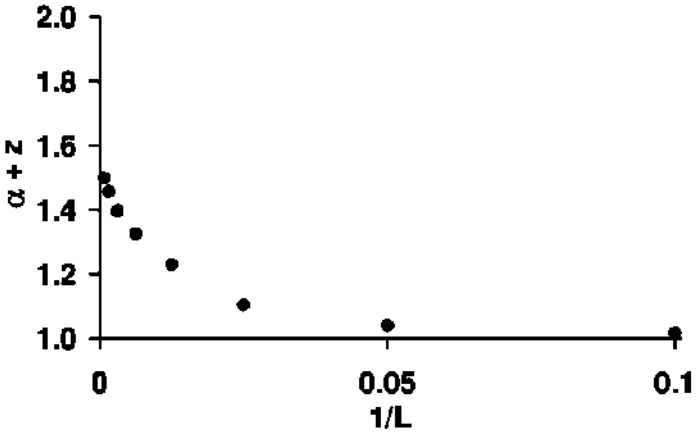

Figure 2.7. The plot shows the quantity $\alpha + z$ vs. $1/L$. Refer [36] for further details.

The ballistic deposition model shows strong corrections to scaling up to lattice sizes of 1280 lattice constants wide, leading to quite low convergence rates towards the asymptotic values of the exponents α, β, and z. Results presented in [63] indicate that correction scale higher than 1280 has not been investigated and it requires more processes of simulating larger lattices to obtain better estimates.

1+1 dimension study of finite-size scaling of the ballistic deposition model provides an example of how nanostructured materials may introduce more stringent demands on present day theories. In particular, the slow convergence of the exponents α, β, and z to their asymptotic limit may prevent some real systems from being in the asymptotic regime. However, it requires more study on the KPZ universality model and its connection with the ballistic deposition model.

2.4. Direct connection between the BD and the KPZ equation

Takashi Nagatani [55] described a direct and formal derivation of the KPZ equation from the ballistic deposition models. Figure 2.1 shows that the particle sticks to the first site along its trajectory and occupies nearest neighbour. It represents ballistic deposition as $i-1, i, i+1$. At time $t+1$, the

height $h(i,t+1)$ is given by

$$h(i,t+1) = max[h(i-1,t), h(i,t) + h(i+1,t)] \tag{2.64}$$

where max [] is the maximum of the function. In [41] a limiting procedure was applied to the difference of heights between nearest neighbours and the following Eq. (2.15) was obtained

$$h(i,t+1) - h(i-1,t+1) = \lim_{\varepsilon \to 0^+} \varepsilon \ln \frac{e^{\frac{h(i-1,t)}{\varepsilon}} + e^{\frac{[h(i,t)+1]}{\varepsilon}} + e^{\frac{h(i+1,t)}{\varepsilon}}}{e^{\frac{h(i-2,t)}{\varepsilon}} + e^{\frac{h(i-1,t)+1}{\varepsilon}} + e^{\frac{h(i,t)}{\varepsilon}}}. \tag{2.75}$$

When $e^{\frac{h(i,t)-h(i-1,t)}{\varepsilon}}$ is replaced by $c(i,t)$ a difference-difference equation was obtained

$$c(i,t+1) = [\delta c(i-1,t) + c(i-1,t)c(i,t) + \delta c(i-1,t)c(i,t)c(i+1,t)][\delta + c(i-1,t) + \delta c(i-1,t)c(i,t)]^{-1}, \tag{2.86}$$

where $\delta = e^{-\frac{1}{\varepsilon}}$. We consider that the hydrodynamic mode on in the rough surface in the coarse-grained scales. The perturbation method applied to Eq. (2.16) defined slow variables X and T for the space variables i and time variables t [69].

For $|\Delta x| \ll 1$, we get $X = (\Delta x)i$, $T = \delta(\Delta x)^2 t$. By setting $\ln c(i,t) = (\Delta x)\nu(\Delta x i, \delta(\Delta x)^2 t) = (\Delta x)\nu(X,T)$, and expanding $c(i,t)$ to order $(\Delta x)^3$, the following formula was obtained

$$c(i,t) = exp[(\Delta x)\nu(X,T)] = 1 + (\Delta x)\nu + \frac{(\Delta x)^2\nu^2}{2} + \frac{(\Delta x)^3\nu^3}{6} + \cdots, \tag{2.17}$$

where ν equals $\nu(X,T)$ in the second equality. Similarly, $c(i-1,t), c(i+1,t)$ and $c(i,t+1)$ were expanded in [41] and by substituting long-wavelength expansion into Eq. (2.18)

$$c(i,t+1) = \frac{[c(i-1,t) + c(i-1,t)c(i,t)]}{[1 + c(i-1,t)]}. \tag{2.98}$$

We obtained KPZ equation through Burgers equation

$$\partial_T h = \frac{[(\partial_X h)^2 + \partial_X^2 h]}{8}. \tag{2.19}$$

In addition, there was an attempt at modifying models for the ballistic deposition with next nearest neighbour sticking rule in the same sequence as Eqs (2.14)-(2.17). However, the application of the limiting procedure and the perturbation method to the (2+1)-dimensional ballistic deposition could not derive the KPZ equation.

2.5. Eden model and universality within the one-dimensional KPZ class

Previously, Derrida et al. [70] [71] have proposed that for all (1+1) dimensional models within the KPZ class, the large deviation function related to the interface height h exhibits universal scaling in the limit of large systems

$$R_T = \frac{[\langle h^3 \rangle]^2}{\langle h_t^2 \rangle \cdot \langle h_t^4 \rangle} \tag{2.20}$$

converges to a universal value of 0.415 to 17 as t approaches infinity. In this expression, h_t represents the space-averaged height, and refers to ensemble averages

Although the KPZ equation can describe a wide range of systems, including particles moving on a lattice or directed polymers in random media, we will focus solely on growth models to simplify the presentation. The extension to other applications should be relatively straightforward. In this context, we consider a discrete growth model on a one-dimensional lattice of N sites with periodic boundary conditions. At each time step, a growth event occurs in each site with a probability dt.

The space-averaged height after t time steps is the quantity h_t whose distribution we are interested in. It should be noted that the variable under consideration in [70] was $Y_t = Nh_t$. As a result, the phrasing of the findings may change differently here. Alternatively, we will utilize the averaged velocity $v_t = h_t/t$ as a variable.

The probability distribution $P(h_t)$ should become independent of the starting condition if t is high enough. The long deviation function f is defined in the long time limit as

$$f(v) = \lim_{t\to\infty} \frac{lnP(vt)}{t}. \tag{2.21}$$

We hypothesize that for large systems, the high deviation function takes the form when the departure of v from its average $\bar{v}$ is at most of order $1/N$

$$F(v) = KH\left(N\frac{v-\bar{v}}{\bar{v}}\right), \tag{2.22}$$

where asymptotic behavior of H is as follows:

$$\begin{aligned} H(V) &= -V^2 + O(V)^3 \text{ for } |V| < 1, \\ H(V) &\simeq -[2\sqrt{3}/(5\sqrt{\pi})]V^{\frac{5}{2}} \text{ for } V \to +\infty, \\ H(V) &\simeq -[4\sqrt{\pi}/3]|V|^{\frac{3}{2}} \text{ for } V \to -\infty. \end{aligned} \tag{2.23}$$

The coefficient K is defined as

$$K = \frac{1}{2N^2}\frac{\overline{v^2}}{\lim_{t\to\infty}(\langle h_t^2 \rangle_c / t)}, \tag{2.24}$$

where $\langle h_t^2 \rangle_c$ is the second order cumulant. The rescaling factor K varies depending on the model, but it is believed that the form of H is the same for all microscopic models within the KPZ class..

It is worth noting that the shape of H presented above may be influenced by the type of boundary conditions utilized. For open border circumstances, for example, we can get a different answer. However, it is believed that H is universal in that it would be consistent across all microscopic models, given the same geometrical restrictions, such as periodic boundary conditions in this case.

The central component of the big deviation function defines all the cumulants $\langle h_t^2 \rangle_c$. The universality of the limit of Eq. (2.21) follows directly from the universality of the form of Eq. (2.22).

In this part, we describe the analytical results derived for the huge deviation function on several models. Initially, the suggestion of the hypothesis was put forth after computing the large deviation function for a specific model in the KPZ class, the asymmetric exclusion process (ASEP).

In the ASEP, a system of particles p moves on a ring of N sites. If this site is unoccupied, each particle jumps to the next site to its right with probability Δt during each time interval Δt. The large deviation function [70] confirms the scaling equation (2.22) for the asymmetric exclusion process (ASEP) model. It is not applicable to other models.

$$K = \sqrt{\frac{\rho(1-\rho)}{\pi N^3}} \tag{2.25}$$

and

$$\bar{v} = \frac{N}{N-1}\rho(1-\rho). \tag{2.26}$$

Since then, Lee and Kim [72] have expanded the result to include the partially asymmetric exclusion process, where particles can move to the right or left with a probability. $(1+\varepsilon)\Delta t/2$ or $(1-\varepsilon)dt/2$. They did it by employing the theory of quantum spin chains and discovering the form Eq. (2.22) with

$$K = \varepsilon\sqrt{\frac{\rho(1-\rho)}{\pi N^3}} \tag{2.27}$$

and

$$\bar{v} = \varepsilon\frac{N}{N-1}\rho(1-\rho). \tag{2.28}$$

Brunet and Derrida [73] have been thinking about guided polymers that are anchored to impurities. If we consider the height of the interface as equivalent to the free energy for a polymer with length t, then this model falls within the KPZ class. According to earlier results, the scaling Eq. (2.23) for the big deviation function, and hence the universal asymptotic value appear to be proven.

Analytical findings are difficult to get for the majority of models. In the limit of a big system, it is easier to determine numerically whether the cumulant ratio converges to the hypothesized universal value 0.415 to 17.

It should be noted that because the computation of the fourth moment of a quantity that is an average over a large number of data points is quite time-consuming as it involves analyzing the statistics of the quantity.Furthermore, as t rises, we have less and fewer statistics to determine from a particular simulation. This is why significant t fluctuations are crucial.

As a result, our numerical computations are more indicative of the conjecture than true numerical proofs. However, we believe they are substantial. Some simulations for various deposition models had been done in [71].

Stauffer [74] then released some numerical findings derived for the Eden model, which appeared to contradict the hypothesis. We believe there is no contradiction. The difference stems

from how time is defined. If we define time as we propose below, our numerical results are plainly consistent with the hypothesis.

First, let us review the Eden model's definition. We consider an interface growing on a ring with N sites. At each time step, we choose one of the boundary sites, which is an empty site that borders an occupied site, as described in version A of [29]. If a boundary site is selected, it becomes occupied and its unoccupied neighbors become new boundary sites.

The number N_{B} of border sites fluctuates with the form of the interface throughout time. In the continuous limit, each boundary site should be picked with probability Δt at each time step dt. This indicates that the greater the N_{B}, the more likely at least one location will be picked.

To account for this impact in numerical simulations, time should not be increased by a consistent amount between two border site choices. $\frac{1}{N_B}$ should be used to weight the time increment.

The crucial distinction between our numerical simulations and Stauffer's lies in this aspect. Stauffer was employing the classic Eden model [48], in which time is not weighted. We observe that the simulation results in Figure 2.8 align with the hypothesis when using the weighted definition of time.

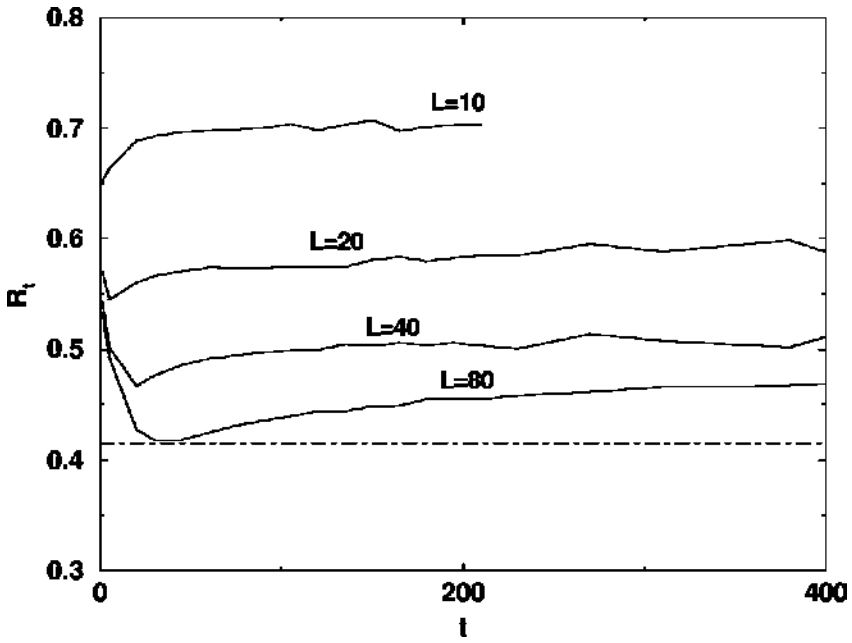

Figure 2.8. The graph shows the relationship between the cumulative ratio and time for different system sizes. The horizontal line with dots and dashes represents the expected value for an infinite system over an infinite amount of time. The data was gathered for various system sizes $L = 10, 20, 40,$ *and* 80*, time unit are* 10^{11}, $8.5 \cdot 10^{10}$, $2.3 \cdot 10^{10}$, *and* $8 \cdot 10^{9}$ *time units. Time is specified in such a way that each boundary site may be picked with probability dt at each time step dt [77].*

Stauffer's results indicate that the original Eden model would not be classified as KPZ. This is what the following basic argument would imply. As previously stated, using a weighted time implies that an event can occur in any location separately. If we take a nonweighted time, we

may infer that the chance of an event occurring in a certain site is dependent on the geometry of the interface in the entire system. As a result, the growth criteria are no longer local, therefore it is not unexpected that the model is not in the KPZ class [74].

DOI: 10.14750/ME.2023.031

3. KPZ EQUATION / STOCHASTIC BURGERS/SCALIG EXPONENT

3.1. KPZ equation

The Kardar-Parisi-Zhang (KPZ) equation is

$$\frac{\partial h}{\partial t} = -\lambda(\nabla h)^2 + \nu\nabla^2 h + \sqrt{Cr}\eta, \tag{3.1}$$

where stands for space-time white noise first, generally which is a Gaussian field with a distribution valued correlation function. It is an equation for a height function with a random evolution $h \in \mathbb{R}$ that depends on position $x \in \mathbb{R}$ and time $t \in \mathbb{R}_+$. The physical constants are λ, ν and Cr

$$\langle \eta(x,t), \eta(x',t') \rangle = \delta(x-x')\delta(t-t'), \tag{3.2}$$

where $x'$and $t'$are just variables used to specify the covariance function of the noise term, $\delta(x)$ and $\delta(t)$ are Dirac delta functions.

Kardar, Parisi, and Zhang initially proposed the Eq. (2.2) in 1986 [1], and it swiftly rose to prominence as physics' standard explanation for random interface growth. The mathematical complexity of the nonlinearity made it too difficult for the stochastic partial differential equations to be effective. Thus, the issue of well-posedness is really critical.

Formally, it is equivalent to the stochastic Burgers equation

$$\frac{\partial h}{\partial t} = -\lambda(\nabla h)^2 + \nabla^2 h + \sqrt{Cr}\partial_x \eta. \tag{3.3}$$

In higher dimensions, a similar equation can be written,

$$\frac{\partial h}{\partial t} = -\lambda|\nabla h|^2 + \nu\Delta h + \sqrt{Cr}\eta \tag{3.4}$$

with $x \in \mathbb{R}^d$. Additionally, one may try to generalize the non-linearity

$$\frac{\partial h}{\partial t} = f(\nabla h) + \nu\Delta h + \sqrt{D}\eta. \tag{3.1}$$

It seems that only Eq. (3.1) produces a nontrivial field when space-time white noise is forced. Here, we'll stick to just one space dimension with quadratic nonlinearity Eq. (3.1). We are still dealing with the extremely challenging problem of a field theory with broken time reversible invariance in this 1+1 dimensional scenario.

The stochastic Burgers Eq. (3.3) serves as a representation for turbulence as a mathematical model. Forster, Nelson, and Stephen [78] conducted a dynamical renormalization group analysis on it in 1977 [78] (see also [1], [12]), forecasting a dynamical scaling exponent

$$z = \frac{3}{2}. \tag{3.2}$$

This implies that one should anticipate nontrivial fluctuation behavior under the rescaling for the KPZ equation's solution h

$$h(x,t) = \varepsilon^{\frac{1}{2}} h(\varepsilon^{-z}t, \varepsilon^{-1}x), \tag{3.3}$$

where ε is rescaling constant.

This will be covered in much more detail later on in the notes. We now turn to the process' physical derivation and its physical predictions. Note that the goal of this introduction is merely to describe the physical background; it is not meant to be rigorous. Naturally, one is interested in demonstrating the equation's existence and uniqueness from a mathematical perspective. The solutions, however, can be expressed in terms of a classically well-posed stochastic partial differential equation, as we shall see. The main focus of these notes will be on the scaling exponents, the large scale fluctuation behavior, and the actual behavior of solutions, all of which are hypothesized to be universal within the so-called KPZ universality class.

3.2. Physical interpretation

Both diffusion and random deposition are processes that h grows. Three factors contribute to the passage of time: (3.1) Growth that is lateral or slope dependent, (3.2) relaxation, and (3.3) random forcing. The result is as follows:

$$\frac{\partial h}{\partial t} = -\lambda f(\nabla h)^2 + \nu \nabla^2 h + \sqrt{Cr}\eta. \tag{3.8}$$

the first term on the right hand side is the non-linear term $(\nabla h)^2$ and the second one $(\nabla^2 h)$ is the diffusive term of Eq. (3.8). It is assumed that the random force Eq. (3.3) is roughly independent at various times and locations. Gaussian space-time white noise, which has a mean zero and space-time correlations, is the most basic model.

$$\langle \eta(x,t), \eta(s,y) \rangle \coloneqq E[\eta(t,x)\eta(s,y)] = \delta(x-y)\delta(t-s). \tag{3.9}$$

The noise level is represented by the letter $\sqrt{Cr}$.Traditionally, it has a square root, making Cr the variance or mean square. The important term in Eq. (3.1), the deterministic portion of the growth, is considered to be a symmetric function that depends solely on the slope. An illustration of what we mean by "lateral growth" is shown below.

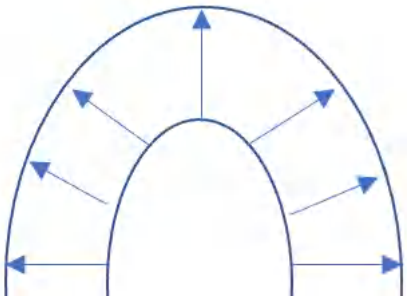

Figure 3.1. Lateral growth process.

The obvious alternative for f in the image might be $(1 + (\nabla h)^2)^{-\frac{1}{2}}$. However, this results in an equation seems impossible to solve. Amazingly, one discovers a non-trivial field through such a naive derivation (see introductions in [80], [2], and [29]).

DOI: 10.14750/ME.2023.031

3.3. Scaling concept

Here, we focus just on the specific choice $\lambda = \nu = \frac{1}{2}, Cr = 1$,

$$\frac{\partial h}{\partial t} = -\frac{1}{2}(\nabla h)^2 + \frac{1}{2}\nabla^2 h + \eta. \tag{3.10}$$

Subsituiting

$$h_\varepsilon(t,x) = \varepsilon^b h(h^{-z}t, \varepsilon^{-1}x) \tag{3.11}$$

we obtain $\frac{\partial h}{\partial t} = \varepsilon^{z-b}\nabla h_\varepsilon$, $\nabla h = \varepsilon^{1-b}\nabla h_\varepsilon$, and $\nabla^2 h = \varepsilon^{2-b}\nabla^2 h_\varepsilon$. The rescaling of the white noise is more intriguing

$$\xi(t,x) \overset{dist}{=} \varepsilon^{\frac{z+1}{2}}\xi(\varepsilon^1 x, \varepsilon^z t). \tag{3.12}$$

If the two random fields have the same distribution that demonstrates the equality then this leads to

$$\frac{\partial h}{\partial t} = -\frac{1}{2}\varepsilon^{2-z-b}(\partial_t h_\epsilon)^2 + \frac{1}{2}\varepsilon^{2-z}\partial_x^2 h_\epsilon + \varepsilon^{b-\frac{1}{2}z+\frac{1}{2}}\eta. \tag{3.13}$$

Apparently, we have a choice now $\lambda = \frac{1}{2}\varepsilon^{2-z-b}$, $\nu = \frac{1}{2}\varepsilon^{2-z}$, $\sqrt{Cr} = \varepsilon^{b-\frac{1}{2}z+\frac{1}{2}}$ to get (3.1) from (3.10). When comparing discrete models to KPZ, one must determine the proper v, and Cr (see [81]).

3.4. 1 + 1 dimensional noisy Burgers equation

The height differences is $h_t(x') - h_t(x)$ in 1 + 1 dimensions that become stationary as $t \to \infty$. If h_t is regulated by the KPZ equation, then h fulfills

$$\frac{\partial h}{\partial t} = \frac{\partial}{\partial x}\left[\frac{1}{2}\lambda h^2 + \frac{1}{2} + \nu\frac{\partial}{\partial x}h\right]. \tag{3.14}$$

Burger's equation contains $\lambda = -1$, which may be obtained by replacing h with $-\frac{1}{\lambda}\tilde{h}$. Burgers h is the velocity field of a one-dimensional fluid. Equation (3.14) is therefore the Navier-Stokes equation with random forcing.

Because h is locally preserved, we can still fix its average value, which is set to $\langle h \rangle = 0$ by our starting data. Noise and diffusion alone (i.e. Eq. (3.14) with $\lambda = 0$) generate a unique invariant distribution. It is Gaussian white noise with covariance.

$$\langle h(x)h(x')\rangle = (\gamma/2\nu)\delta(x - x'). \tag{3.15}$$

This measure also happens to be invariant under the flow created by the solutions of

$$\frac{\partial h}{\partial t} = \frac{\left(\frac{\lambda}{2}\right)\nabla^2 h}{\Delta x} \tag{3.16}$$

[78], [82]. To demonstrate this, imagine a length L interval with periodic boundary conditions. Formally, the right side of Eq. (3.16) is devoid of divergence

$$\int_0^L \frac{\partial}{\partial x} h(x)dx = 0 \tag{3.17}$$

because of periodic boundary conditions. As a result, we just need to confirm the density's temporal invariance

$$exp\left[-\frac{\nu}{\gamma}\int_0^L (x)^2 dxht\right]. \tag{3.18}$$

Differentiating in time yields

$$-\left(\frac{\lambda\nu}{2\gamma}\right)\left[\int_0^L h(x)\frac{\partial}{\partial x}h(x)^2 dx\right] exp\left[-\frac{\nu}{\gamma}\int_0^L h(x)^2 dx\right]. \tag{3.19}$$

The prefactor is eliminated by partial integration. In higher dimensions, the prefactor is $\int h(x)(h(x)\cdot\nabla h(x)d^d x$ which, in general, does not vanish.

The stationarity of white noise comes as a surprise since a smooth profile h_t first converges as $t \to \infty$ to a constant profile. White noise profiles are often harsh and may not settle as $t \to \infty$. These arguments raise the question of how mathematically defined Eq. (3.t14) is. Of course, a small distance limit should be implemented physically. If one discretizes Eq. (3.14) as

$$\begin{gathered}\frac{d}{dt}h(j) = \left(\frac{\lambda}{6}\right)\big(h(j) + h(j+1)\big) + h(j+1)) - h(j-1)(h(j-1) + h(j))) + \\ \nu(h(j+1) - h(j-1)) + \xi(j),\end{gathered} \tag{3.20}$$

the $h(j)$'s are distributed as separate Gaussian distributions with variance $\gamma/2\nu$ in the steady state [83]. Furthermore, as will be detailed in Chapter 6, the stationary distribution for numerous lattice growth models may be determined explicitly. At a large separation, the slopes are independent. These findings increase our faith in Eq. (3.15).

In the case of stationary growth, we infer that

$$\langle (h_t(x) - h_t(x'))^2\rangle = \left(\frac{\gamma}{2\nu}\right)|x - x'|. \tag{3.21}$$

Our reasoning provides no insight into the scaling function. Jansen and Schmittmann [84] demonstrated that there is a universal function, g, such that is average in the stationary measure with small k and large t in the Eq. (3.22).

$$\int e^{ikx}\langle h(x)h(0)\rangle dx = \frac{\gamma}{2\nu} g\left(\left(\frac{\lambda^2\gamma}{2\nu}\right)^{\frac{1}{3}} k|t|^{\frac{2}{3}}\right). \tag{3.22}$$

The scaling function $g(x)$ is not explicitly known. Because of symmetry, $g(x) = g(-x)$ and $g'(0) = 0$. Authors [84] calculated $g(x)$ for a small x and discovered $g"(0) \cong -4.5$. For large x approximations show that g decays as $exp\left(-c|a|^{\frac{3}{2}}\right)$, where c is a constant and a is the amplitude value [79], [85], [86]. The key point in (3.22) is that only macroscopic growth

DOI: 10.14750/ME.2023.031

model parameters appear: λ represents the growth velocity, and $\gamma/2\nu$ is the intensity of the static fluctuations. The scaling form (3.22), which determines the large scale behavior of any two-dimensional growth process (assuming the growth rules are sufficiently local and $\lambda \neq 0$; dictates the large scale behavior of any two-dimensional growth process).

Since we have predicted the stationary measure, we may compute the effective growth velocity $v_{eff}(\nabla h)$ (see explanation below Eq. (3.23)). The Gaussian (3.18), in fact, is the steady state for any bare growth velocity $v(\nabla h)$. The effective growth velocity is thus provided by (3.14) with $\left(\frac{\lambda}{2}\right) h^2$ substituted by $v(h)$

$$v_{eff}(\nabla h) = \int \left(\frac{\nu}{\pi\gamma}\right)^2 e^{-\frac{\nu u^2}{\gamma}} v(\nabla h + h)\, dh. \tag{3.23}$$

4. IMPACT OF THE INITIAL SURFACE MORPHOLOGY

Non-linear PDEs has no general mathematical theory, which could help us to derive physically relevant solutions. There are different methods available, beyond the celebrated Lie algebra formalism [87], the most commonly used method is the reduction technique. This means that the original variables of the PDEs like the time t and the spatial coordinate x are used to define a new variable (for example f). Via a variable transformation the original PDE can be reduced to an ordinary differential equation (ODE). The choice of the form of $f(x,t)$ is basically quite large. Usually, the continuity of first and second derivatives of f in respect of x and t is required. Beyond these continuous models based on partial differential equations (PDEs), there are numerous purely numerical methods available to study diverse surface growth phenomena. Without completeness, we mention the kinetic Monte Carlo [88], Lattice-Boltzmann simulations [89], and the etching model [90]–[96].

4.1. Results without noise term

Simulations have been carried out by MATLAB R2019a. Numerical solution for height profiles are calculated with the following data: $x \in [-200, 200]$, $t \in [0, 10000], N = 100, \Delta t = 1/100$, where N denotes the number of division points on the x-axis and Δt is the time step.

In the resulted figures below the complete solutions of the KPZ Eq.

$$\frac{\partial h}{\partial t}(x,t) = \nu \nabla^2 h(x,t) + \frac{\lambda}{2}(\nabla h)^2 + \eta(x,t), \tag{4.1}$$

that have been presented for different initial condition and various amplitudes. However for simplicity, the parameters are chosen as $\nu = \lambda = 0.1$ and the initial conditions are

$$h(x,0) = \left(1 \cdot \cos\left(\frac{x}{8}\right)\right)\left(1 + \sin\left(\frac{x}{8}\right)\right) \tag{4.2}$$

and

$$h(x,0) = \left(0.1 \cdot \cos\left(\frac{x}{8}\right)\right)\left(0.1 + \sin\left(\frac{x}{8}\right)\right). \tag{4.3}$$

Figure 4.1 presents the solutions in the time range $[1, 600]$ for the different amplitudes applied in the initial conditions Eqs. (4.2) and (43). It seems that the results are vibrating depending on the parameter value in the initial condition. In Fig. 4.1(a) it can be seen that $h(x,t)$ is between ± 1.3 and in Fig. 4.1(b) that it is between ± 0.6 which begin to smooth out in the both cases. This examination suggests that the initial condition amplitudes affect only the early phases of the surface evolution, while later the surface tends to approach a flat state regardless of the initial amplitudes.

DOI: 10.14750/ME.2023.031

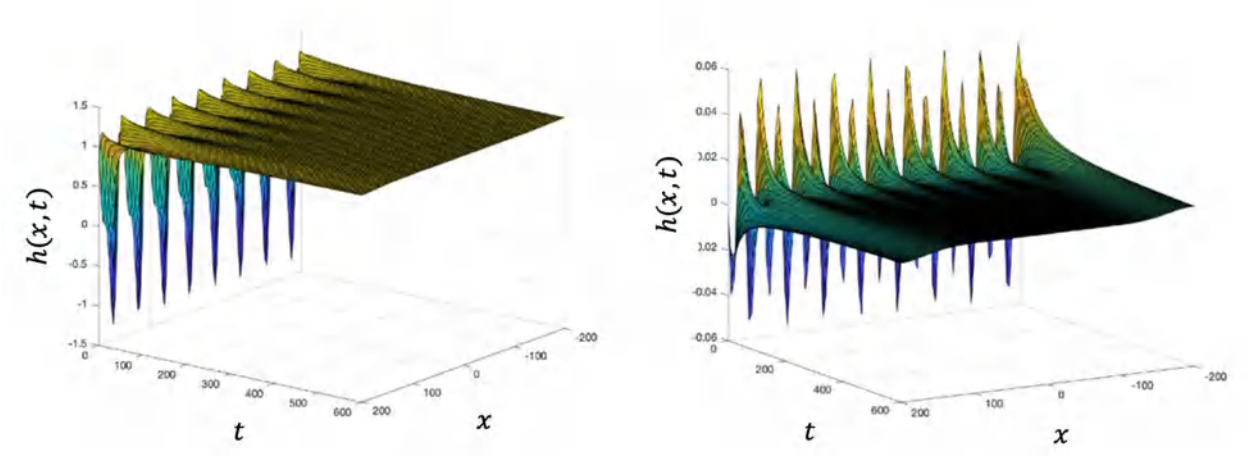

a b

Figure 4.1. The solutions of the KPZ equation (4.1) without noise term with initial conditions (4.2) and (4.3).

Figure 4.2 presents the results in the same parameters for $\nu = \lambda = 0.1$ applying different initial condition.

The following initial conditions are considered

$$h(x,0) = \left(1 \cdot \sin\left(\frac{x}{16}\right)\right) + \left(1 \cdot \cos\left(\frac{x}{16}\right)\right) \tag{4.4}$$

and

$$h(x,0) = \left(0.1 \cdot \sin\left(\frac{x}{16}\right)\right) + \left(0.1 \cdot \cos\left(\frac{x}{16}\right)\right). \tag{4.5}$$

Figures presented in Fig. 4.2(a) and Fig. 4.2(b) are different from each other by difference in their amplitudes. Based on these results, we can conclude that for initial condition amplitudes greater than 1, the surface evolution shown in Fig. 4.2(a) starts from a negative height with some waves, but increasing the amplitude leads to a decrease in the wave amplitude and the surface eventually approaches a flat state in the end. However, small amplitude values increase waviness in $h(x,t)$ line proportionally.

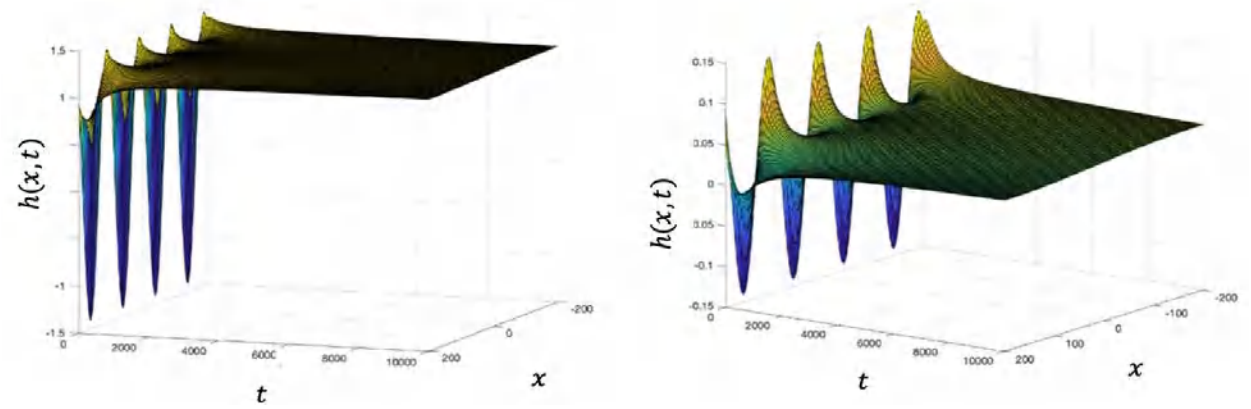

a b

Figure 4.2. The solutions of the KPZ Eq. (4.1) without noise term with initial conditions (4.4) and (4.5).

To illustrate the impact of the amplitude of the initial surface Fig. 4.3(a) and Fig. 4.3(b) exhibit the solution to Eq. (4.1) with initial conditions

$$h(x,0) = 1 \cdot sin\left(\frac{x}{16}\right) \tag{4.6}$$

and

$$h(x,0) = 0.1 \cdot sin\left(\frac{x}{16}\right), \tag{4.7}$$

and also gives the same results as discussed above.

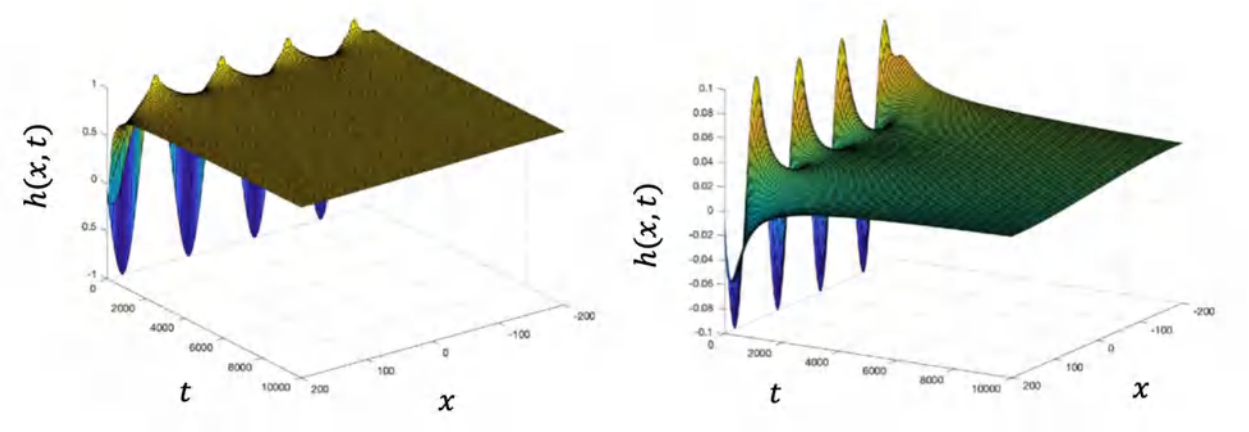

a b

Figure 4.3. The solutions of the KPZ Eq. (4.1) without noise term with initial conditions (4.6) and (4.7).

The functions demonstrate a comparable structure, as shown by Fig. 4.1 and Fig. 4.3, which depict the relationship between amplitude values over the same time period. Figure 4.1 demonstrates that the waviness can be altered based on the amplitude inputs. We may say that different numerical values of initial condition do not drastically change the whole surface as it is.

4.2. Results with Gaussian noise

As the main universality classes relevant for kinetic roughening, we focus on the case in which the surface or interface is subject to time dependent noise. In typical applications, these fluctuations arise in those of a driving flux (of, say, aggregating units, atoms or molecules) acting on the system. This is a convenient way to represent the nature of the noise, but it does not by any means imply that its amplitude is directly the square root of the average external flux. For instance, in studies of grows molecular beam epitaxy (MBE) for electrochemical [97] or chemical vapor deposition (ECD, CVD, respectively) [98] the noise term appearing in the Langevin equation for the interface [51], [99] is seen to be rather more involved than that. However, and this can never be overemphasized, the universal behavior applies to asymptotic properties, well beyond all existing transients (induced by, e.g. physical instabilities acting on the system) and crossovers (due

to competition among various physical mechanisms, each of which is dominant for a different range in time and space). For the type of systems, we are considering, the asymptotic properties are adequately described by equations featuring additive noise, which is Gaussian and uncorrelated in time and space [100].

Applying similarity transformation $h(x,t) = f(\zeta)$ and $\zeta = \frac{x}{\sqrt{t}}$ with Gaussian noise gives us the ODE of

$$vf''(\zeta) + 0.5f'(\zeta)[\zeta + \lambda f'(\zeta)] + ae^{\frac{-\zeta^2}{n}} = 0, \quad t > 0, \tag{4.8}$$

where a is in connection with the standard deviation of the Gaussian distribution and n determines the type of the noise term [96]. There is no general formula available for arbitrary parameters λ, μ, a. Fortunately, if two parameters are fixed e.g. $v = \lambda = 0.1$ and $n = 1$, then there is a closed expression (analytical solution) available for the solution

$$f(\zeta) = -\frac{1}{2\lambda}\ln\left[1 + \tan\left\{\sqrt{\lambda a\pi}\cdot \operatorname{erf}\left(\sqrt{\frac{\zeta}{2}}\right) + c_1\right\}^2\right] + c_2, \tag{4.9}$$

where erf means the error function and c_1 and c_2 are integration constants, see [95], [96].

Figure 4.4 presents the numerical results for the given parameters and $a = 1$ and for applying different initial condition amplitudes to Eq. (4.1) as follows

$$h(x,0) = \left(1\cdot\cos\left(\frac{x}{8}\right)\right)\cdot\left(1+\sin\left(\frac{x}{8}\right)\right) \tag{4.10}$$

and

$$h(x,0) = \left(0.1\cdot\cos\left(\frac{x}{8}\right)\right)\cdot\left(0.1+\sin\left(\frac{x}{8}\right)\right). \tag{4.11}$$

Figures 4.4(a) and 4.4(b) show almost the same structure. The only change is that if the amplitude is 1, the ripple appears, which can also be characterized by the maximum value of the amplitude.

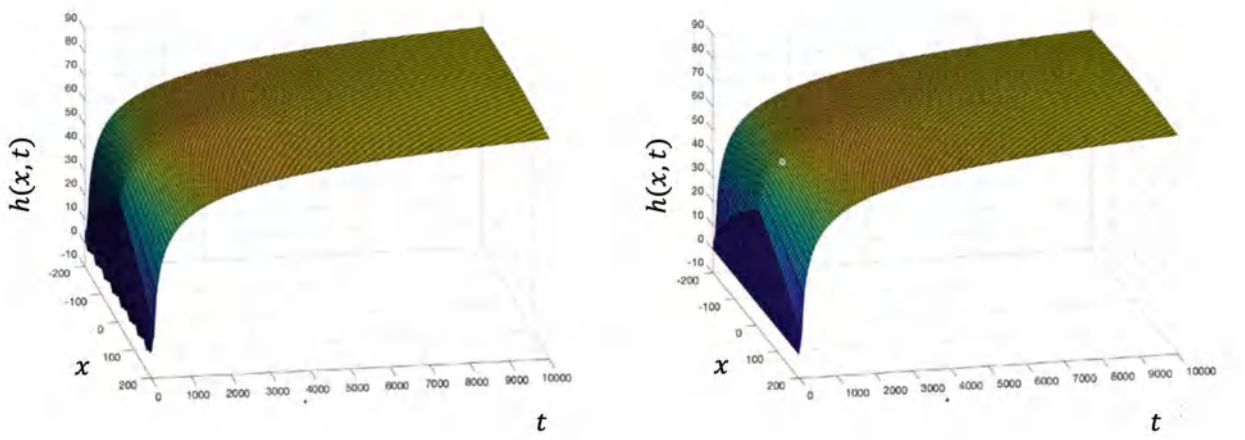

a b

Figure 4.4. The solutions of the KPZ Eq. (4.1) with Gaussian noise term with initial conditions (4.10) and (4.11).

DOI: 10.14750/ME.2023.031

Figure 4.5 shows the solutions of Eq. (4.1) with the same parameters. The figure shows the change in amplitude and the different representations of the graphs. We examine the effect of the strength of the Gaussian noise, denoted by a in Eq. (4.8) providing $a = 0.1$ and $a = 0.01$ in the Gaussian noise term $\eta(x,t)$ together with the initial state

$$h(x,0) = \left(1 \cdot \cos\left(\frac{x}{8}\right)\right) \cdot \left(1 + \sin\left(\frac{x}{8}\right)\right). \tag{4.12}$$

It results the big wavy shape in the surface escaping while keeping increase amplitude of noise term.

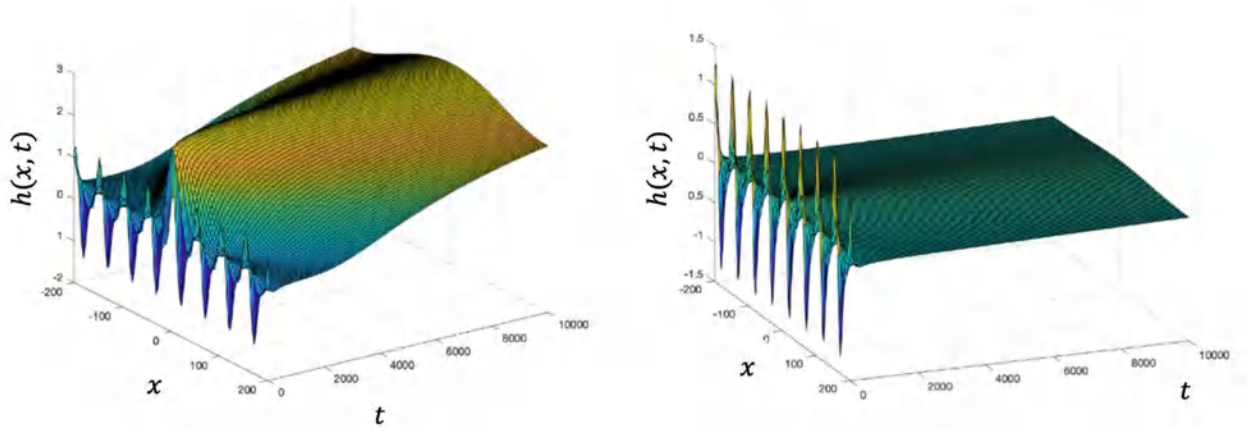

a b

Figure 4.5. The solutions of the KPZ Eq. (4.1) with Gaussian noise term with initial condition (4.12) and a=0.1 or a=0.01.

Figure 4.6 presents the results in the same output figures as presented in Fig. 4.4 in spite of changing initial condition and its amplitudes

$$h(x,0) = 1 \cdot sin\left(\frac{x}{16}\right) + 1 \cdot cos\left(\frac{x}{16}\right) \tag{4.13}$$

and

$$h(x,0) = 0.1 \cdot sin\left(\frac{x}{16}\right) + 0.1 \cdot cos\left(\frac{x}{16}\right). \tag{4.14}$$

DOI: 10.14750/ME.2023.031

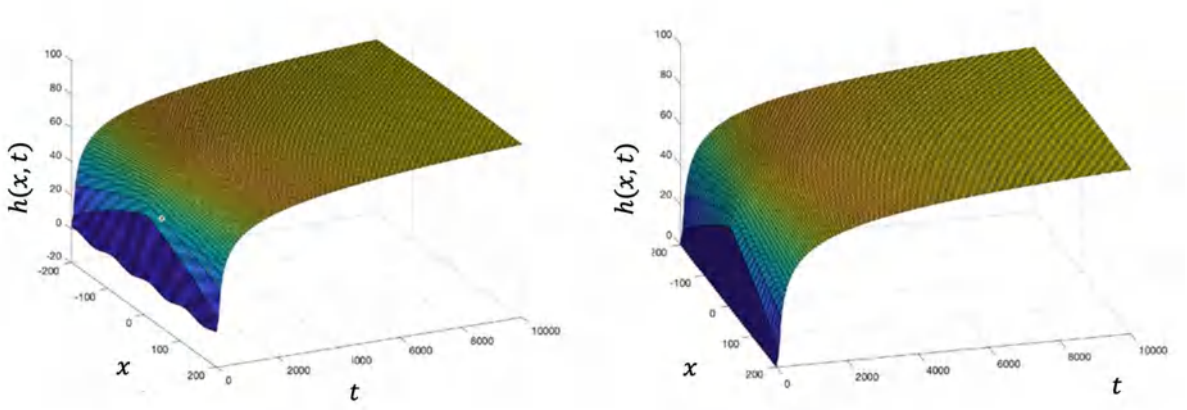

a b

Figure 4.6. The solutions of the KPZ Eq. (4.1)with Gaussian noise term with initial condition (4.14) and (4.4) for a=1.

Figure 4.7 presents the results of the numerical simulations for Eq. (4.1) applying different initial conditions with $a = 0.1$ or $a = 0.01$ in the Gaussian noise term η of Eq. (4.1).

In this figure different amplitude changes can be seen and how the graphs are variously presented while initial condition is kept

$$h(x,0) = 1 \cdot sin(x/16) + 1 \cdot cos\left(\frac{x}{16}\right) \tag{4.15}$$

Difference between Fig. 4.5 and Fig. 4.7 is their wavy steps in the same range $x \in [-200\ 200]$.

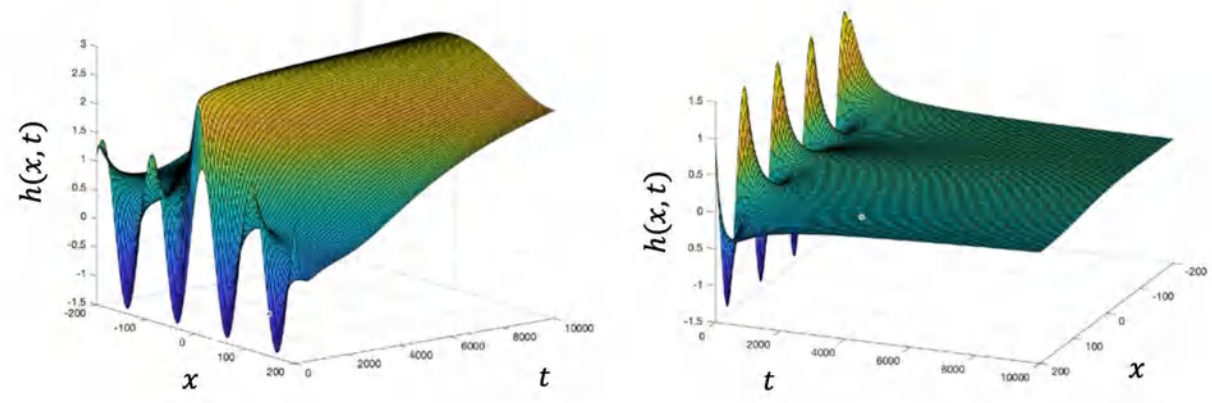

a b

Figure 4.7. The solutions of the KPZ Eq. (4.1) with Gaussian noise term with initial condition (4.15) and a=0.1 or a=0.01.

Figure 4.8 introduces the same output figures as presented in Fig. 4.4 and Fig. 4.6 in spite of changing the amplitudes in the initial condition

$$h(x,0) = 1 \cdot sin\left(\frac{x}{16}\right) \tag{4.16}$$

and

DOI: 10.14750/ME.2023.031

$$h(x,0) = 0.1 \cdot sin\left(\frac{x}{16}\right) \tag{4.17}$$

However, as it is shown that difference between all these figures are their wavy starting points which is increasing waviness in the same range $x \in [-200\ 200]$.

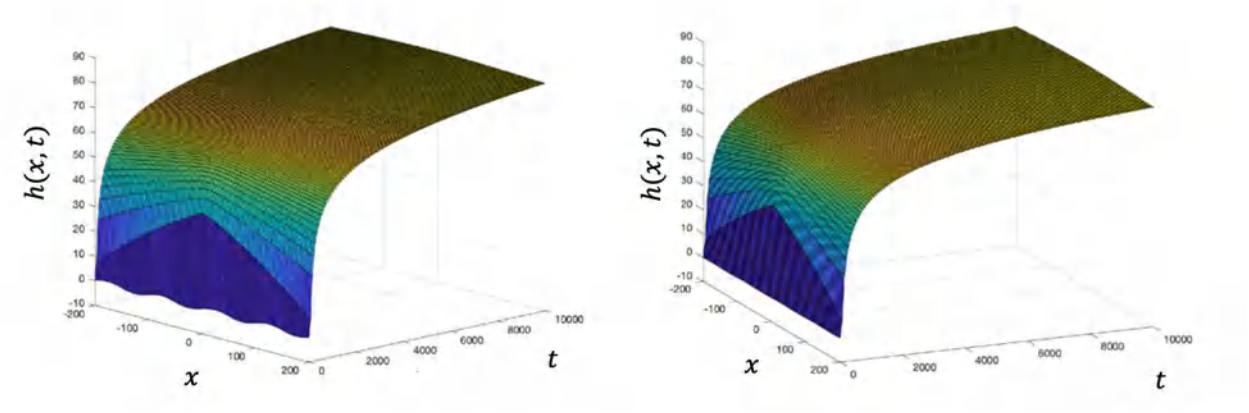

a b

Figure 4.8. The solutions of the KPZ Eq. (4.1) with Gaussian noise term with initial conditions (4.16) and (4.17).

Figure 4.9 presents the results of changed amplitudes with $a = 0.1$ or $a = 0.01$ in the Gaussian noise term η while initial condition is kept

$$h(x,0) = 1 \cdot sin\left(\frac{x}{16}\right). \tag{4.18}$$

As above results here are represents the impact of the initial condition and noise amplitudes and show wavy increase in the graphs.

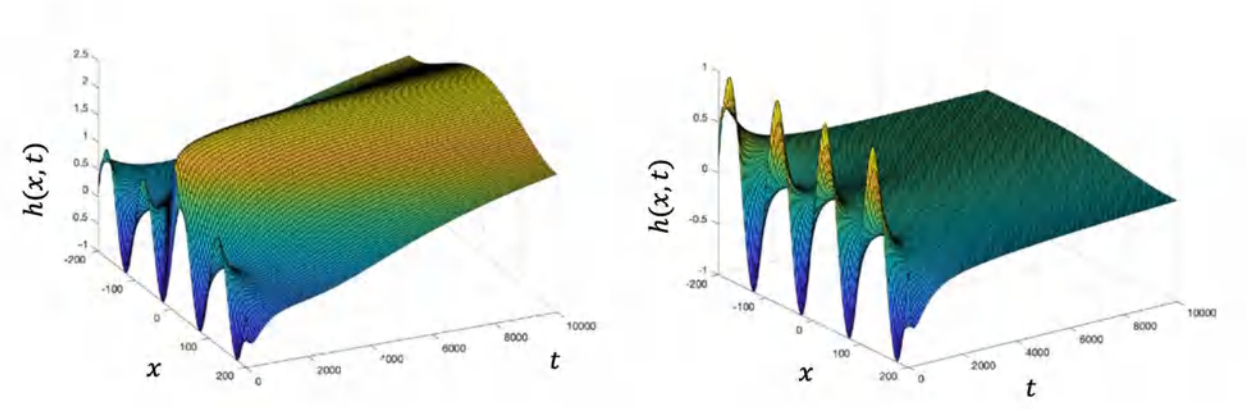

a b

Figure 4.9. The solutions of the KPZ Eq. (4.1) with Gaussian noise term with initial condition (4.18) and a=0.1 or a=0.01.

We consider the solutions of the KPZ equation (4.1) with a Gaussian noise term for initial condition (4.18) and values of a equal to 0.1 or 0.01.

To conclude, we can say that with an appropriate change of amplitudes in the initial condition and/or strength of noise in the noise term; or examining the problem without noise term, numerical solutions for the KPZ equation can be obtained for one spatial dimension. Numerous shaped figures show that every initial condition effects on wavy starting point of surfaces from smaller range to higher on both Gaussian noise and without noise case in the same way. One of the difference between these two cases that if we do not apply the noise term then after some time the solution surface is flat, but applying the Gaussian noise the surface has a wavy structure even after t =10000. Reducing the amplitude in the initial condition provides smoother shape in the surface structure.

4.3. Various initial condition amplitudes with noise terms

In this section we investigate the numerical solution to KPZ Eq. (4.1) with Gaussian noise, white noise and without noise terms. The importance is to point out the morphology of the initial surface of the substrate and the results obtained show different surface formations. In our investigations, the parameter values are chosen as $\nu = 1$ and $\lambda = \frac{1}{2}$ when we refer to the KPZ equation.

In some of previous studies [95], [96], [101]–[106], the role of the additional noise term makes the KPZ solutions interesting. However, when we conducted experiments without noise term in literature [107], [108], it introduced the phenomenal effect of different initial conditions to the surface. Now, our aim is to look for the solutions of Eq. (4.1) with initial condition $A \sin\left(\frac{x}{16}\right)$ applying various amplitudes. Furthermore, we will see numerical results with Gaussian noise and white noise terms with all physical parameters (ν, λ, A). Here, A is the initial condition parameter.

In the simulations, the solutions to Eq. (4.1) with various noise terms have been presented. Also, the case without noise term effect is studied. Furthermore, three different amplitudes are applied for the initial condition of the form

$$h(x,0) = \mathrm{A} \sin\left(\frac{x}{16}\right). \tag{4.19}$$

with amplitude *A.* The numerical analyses have been conducted on the MATLAB R2019b with parameters given below (4.20). In the calculations, the initial time t has been chosen as 0.01 until 100. The following values are fixed throughout the study

$$x \in [-100, 100], \qquad t \in [0.01, 100], \qquad N = 100, \ \Delta t = 0.01/100. \tag{4.20}$$

In the process of the simulation obtaining the solution of the KPZ Eq. (4.1), the initial conditions which mimic the initial surface structure are chosen as in Eqs. (4.21)-(4.23). The amplitude parameters are taken in a maximally simple form to determine relational changes of the initial conditions and the noise term differences. To get a better understanding first, we determine the solution Eq. (4.1) without noise term with different amplitude values

$$h(x,0) = 10 \sin\left(\frac{x}{16}\right), \tag{4.21}$$

and

$$h(x,0) = \sin\left(\frac{x}{16}\right) \tag{4.22}$$

and

$$h(x,0) = 0.1 \sin\left(\frac{x}{16}\right). \tag{4.23}$$

4.3.1. The case: without noise term

The research result using the traveling wave Ansatz with closed forms to obtain analytic solutions to KPZ Eq. (4.1) without noise term was presented in paper [95]. The self-similar Ansatz [95] has the form $h(x,t) = t^{-\alpha} f\left(\frac{x}{t^{\beta}}\right) := t^{-\alpha} f(\omega)$, These methods belong to the reduction mechanism, where applying a suitable variable transformation reduces the original partial differential equations (PDEs) or systems of PDEs to an ordinary differential equation (ODE) or systems of ODEs. Applying the traveling wave Ansatz to the KPZ partial differential Eq. (4.1) with $\eta(x,t) = 0$ leads to the ordinary differential equation (ODE) of

$$-\nu f''(\omega) + f'(\omega)\left[c - \frac{\lambda}{2} f'(\omega)\right] = 0. \tag{4.24}$$

The solution to equation (4.24) can be given as

$$f(\omega) = \frac{2}{\lambda} \ln\left(\frac{\lambda\left[c_1 \nu e^{\frac{c\eta}{\nu}} - c_2 c\right]}{2\nu c}\right)\nu, \tag{4.25}$$

where c_1 and c_2 are the constants of the integration. It should be noted that this is a linear function equation $f(\omega) = a\omega + b$ which is presented in a complicated form. The parameters for c_1 is set, and it equals 0, which gives a constant solution. Physically it means that there is a continuous surface growing till infinity which is quite unphysical. Therefore, some additional noise is needed to have physically realistic surface growing phenomena. However, in our situation, when there is no noise term ($\eta(x,t) = 0$), the surface is flat without any wavy effect.

DOI: 10.14750/ME.2023.031

When there is an initial condition effect, and its amplitude difference is investigated, then the wavy surface of the graph appears as Fig. 4.10 without any curve or wedge surface effect.

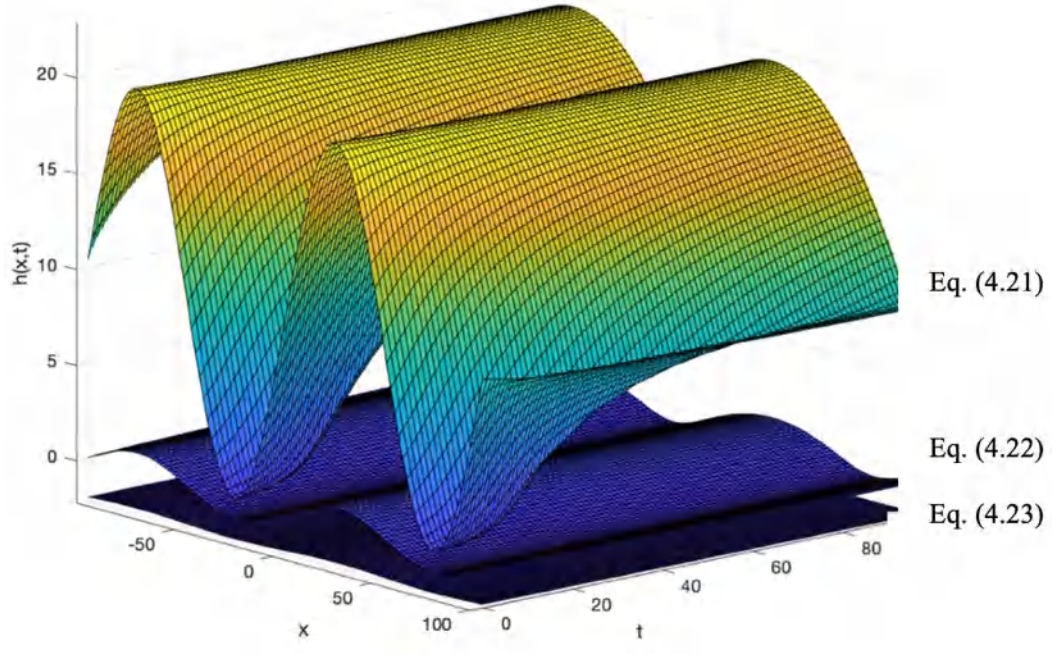

Figure 4.10. The solution graph to (4.1) without noise term and with given values (4.19) and various initial conditions (4.21)-(4.23).

As it is presented in Fig. 4.10, the amplitude of the initial condition is an important parameter for the formation of the surface even without noise term. When the amplitude parameter of the initial condition equals 10, the starting part of the wavy surface fluctuates between given values. After a certain time, this surface becomes flat; see details on the results and numerical data in paper [109].

4.3.2. The case with Gaussian noise term

Kinetic roughening is an important part of universality classes. For this reason, we pay attention to the time-dependent noise affecting the surface growth. Generally, these surface fluctuations occur by driving flux or atoms acting on the system. However, this does not mean that its amplitude is directly the square root of the average external flux. For example, research on beam molecular epitaxy growth for electrochemical or chemical vapor deposition showed that the noise term from the Langevin equation for the interface is more affected. However, it cannot be overemphasized. Universal behavior refers to asymptotic properties, far exceeding all existing transients (induced by, e.g., physical instability acting on the system) and crossovers (due to competition among various physical mechanisms, each of which is dominant for a different range in time and space). Considering the type of system and the asymptotic properties, the equations containing the additive noise term adequately describe the phenomenon. The Gaussian-type noise is uncorrelated in time and space [69]. Applying similarity transformation $h(x,t) = f(w)$ and $w = \frac{x}{\sqrt{t}}$ to (1) with Gaussian noise, one gets the ODE of

$$\nu f''(w) + 0.5 f'(w)[w + \lambda f'(w)] + a e^{\frac{-w^2}{n}} = 0\,, \tag{4.26}$$

where value a is chosen as 1. There is no general formula available for the solution to (4.26) for arbitrary parameters λ, a. If we fixed all parameters such as: $\nu = 1$, $\lambda = \frac{1}{2}$ and $a = 1$, then there is a closed expression (an analytical solution) available

$$f(w) = -\frac{1}{2\lambda} \ln \left[1 + \tan \left\{ \sqrt{\lambda a \pi} \cdot \operatorname{erf}\left(\sqrt{\frac{w}{2}} \right) + c_1 \right\}^2 \right] + c_2, \tag{4.27}$$

where erf means the error function and c_1 and c_2 are integration constants, see [100], [110].

We will consider the case of sharp wedge initial condition for positive, small ε as

$$h_\varepsilon(x, 0) = -\frac{|x|}{\varepsilon} \quad \text{with} \quad \varepsilon > 0, \;\; \varepsilon \to 0. \tag{4.28}$$

The solution to Eq. (4.1) with (4.8) is presented as follows

$$h(x, t) = -\frac{t}{24} - \frac{x^2}{2t} + \left(\frac{t}{2}\right)^{\frac{1}{3}} \eta(x, t). \tag{4.29}$$

The flattening parabola should be viewed as the top part of the droplet in the experiment of [101], [102] and $\eta(x, t)$ represents the superimposed fluctuations. Eventually, the KPZ equation holds in greater generality. In particular, it is also applied for interface motion and growth models in higher dimensions. For surveys on the earlier developments, we refer to [2], [29], [111], [112]. Recently, the KPZ equation has been used as a challenging test ground for non-equilibrium renormalization group techniques [113].

The subtraction $\frac{x^2}{2t}$ from Eq. (4.29) is uniquely fixed by the requirement that $\eta(x, t)$ is independent of x for any given $t > 0$. In fact, by the scaling invariance of the KPZ equation, for fixed t, higher-order correlations also depend only on the relative distance in x. Noise term $\eta(x, t)$ depends on t. However, to find out its value is less obvious. Because a diverging uniform shift in h-direction is the construction of the solution. This is most easily explained for the initial condition $h_\varepsilon(x, 0)$. The construction of the solution requires

$$\lim_{\varepsilon \to 0} e^{h_\varepsilon(x,0)} = \delta(x), \tag{4.30}$$

which presents that $h_\varepsilon(x, 0) = -\varepsilon^{-1}|x| - \log(2\varepsilon)$ with $\log(2\varepsilon)$ diverging as $\varepsilon \to 0$ (see [114]).

DOI: 10.14750/ME.2023.031

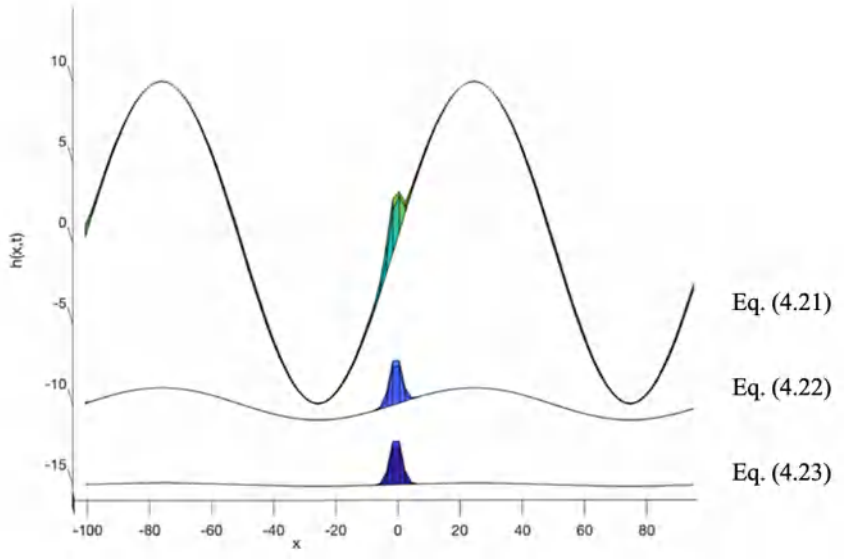

Figure 4.11. Solutions to Eq. (4.1) with Gaussian noise term with values (4.20) and initial conditions (4.21)-(4.23) for t=100.

Figure 4.11 represents the so-called bell curve Gaussian surface. On the one hand, in the graph for the amplitude of the initial condition between 0.1 and 1 (in Eqs. (4.21) and (4.23)) the same curves are obtained in spite of initial surface differences. Alternatively, while initial condition amplitude equals 10, the wavy surface affects the Gaussian noise term curve edge resulting in a decrease in the noise term appearance.

4.3.3. The case with white noise term

The white noise term for $\eta(x,t)$ is not a regular function. The solution $h(x,t)$ partially inherits this roughness of the surface due to the noise and therefore, the function $(\partial h/\partial x)^2$ is not studied till now. Nevertheless, more reliable solutions can be formulated by suitable approximation schemes, which are explained in detail in . The most direct one can be easily stated. One smoothens η to η_κ as

$$\eta_\kappa(x,t) = \int \kappa\varphi\big(\kappa(x-x')\big)\eta(x',t)\,dx' = \varphi_\kappa \cdot \eta(x,t),\ \kappa \to \infty \qquad (4.31)$$

with some smooth function φ, a localized and normalized smearing function. Then $\eta_\kappa \to \eta$ as $\kappa \to \infty$ and Eq. (4.1) has well-defined solutions $h_\kappa(x,t)$ with noise terms η_κ. They move with a uniform background velocity v_κ along the h-direction. Then $v_\kappa \to \infty$ as $\kappa \to \infty$, but $h_\kappa(x,t) - v_\kappa t$ has a limit. Since v_κ sets merely the choice of a reference frame, the claim is that under this limit procedure, the fluctuation properties remain intact [111].

While understandable solutions are thus ensured, little is known about their properties. To make $\frac{\partial h(x,t)}{\partial x}$ stationary, one has to start the solution to the KPZ equation with two-sided Brownian motion. With this input, one argues that the height fluctuations will grow as $t^{\frac{1}{3}}$, while the transverse

correlation length increases as $t^{\frac{2}{3}}$. Very recently, it has been proved that the variance of the stationary two-point function increases as $t^{\frac{4}{3}}$ by providing suitable upper and lower bounds [116]. If we choose as initial function the narrow wedge

$$h(x,0) = -\frac{|x|}{\delta} \tag{4.32}$$

with $\delta \ll 1$, it leads to following representation

$$h(x,t) = \begin{cases} -\dfrac{x^2}{2\lambda t} & \text{for } |x| \leq \dfrac{2\lambda t}{\delta}, \\ -\dfrac{|x|}{\delta} & \text{for } |x| > \dfrac{2\lambda t}{\delta}. \end{cases} \tag{4.33}$$

The initial condition may look artificial. In spite of short times, the nonlinearity dominates, and ignoring the other terms in the Eq. (4.33), h spreads very fast into the parabolic profile. It can be seen as the top part of a growing surface. Physically one thereby covers the case of macroscopically curved height profiles [116]–[120].

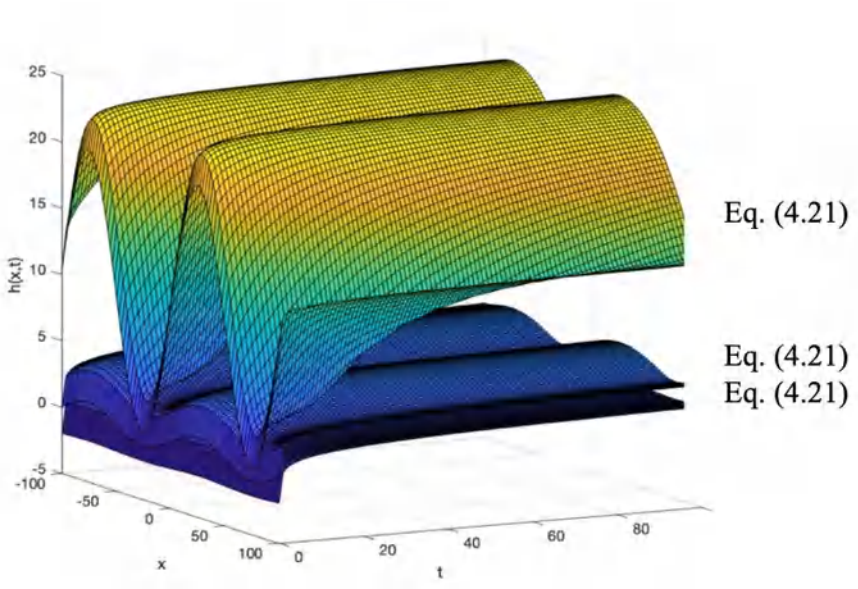

Figure 4.12. Solutions to (4.1) with white noise term with values (4.20) and initial conditions (4.21)-(4.23).

The solution (4.33) for the distribution of $h(x,t)$ for all $t > 0$ is exact in the properly normalized limit $\delta \to 0$. A further explanation has been presented in the paper [116]–[120].

At the beginning of time *t*, there is an angled surface as an effect of the noise term. Despite the difference in amplitude of the initial condition, the primary form of the graph is the same. Figure 4.12 represents the initial condition amplitude effect only to the surface but not the noise itself.

DOI: 10.14750/ME.2023.031

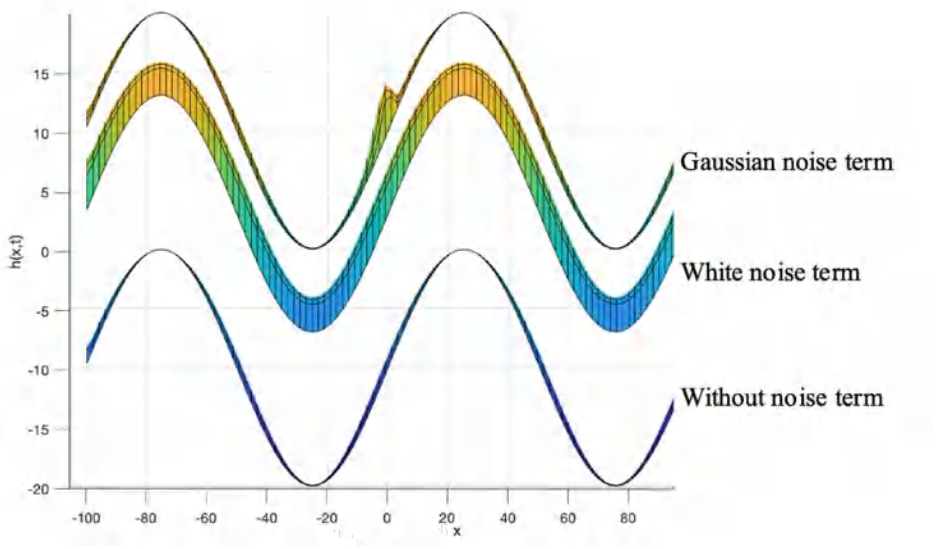

Figure 4.13. Cross-section of h(x,t) and x with the effect of initial condition (4.21) to all three cases for t=100.

To introduce visible differences between the noise terms and amplitude, the impact of them is presented in Fig. 13. It is obvious that the initial condition effect is the same in all the simulations. However, at the beginning of the time t, the parts of each graph are differently formed due to the effect of the noise terms. Without noise term, the graph started with the straight wave surface and smoothed after a certain time. The second simulation result presented for the white noise term graph started with an edge surface at the beginning and took effect of the initial condition to itself. Also, in the third graph with Gaussian noise term, the surface has the same wavy surface formation. However, it can be seen in the middle of the graph that a bell curve shape appeared due to the Gaussian noise term.

The height distribution function of the (1+1) dimensional KPZ equation with different initial condition amplitudes and different noise terms is numerically analysed. It can be concluded that for fixed parameters of KPZ Eq. (4.1), the noise terms represented similar shapes on the surface with the same initial condition. However, the noise term effect remained at the same level in every simulation despite different amplitudes. Moreover, when the initial condition was high enough, then the presence of Gaussian noise cannot be observed on the surface (see Fig. 4.11).

DOI: 10.14750/ME.2023.031

5. IMPACT OF NOISE TERMS

Without having general mathematical theory, non-linear partial deferential equation (PDE) stands in a crucial point in order to derive physically relevant solutions. There are various available techniques [9] and generally the most applied method is the reduction technique. This technic defines a new variable or function (for example f) from the original variables of the PDEs like the time t and the spatial coordinate x. Transforming of original PDE, variables can form an ordinary differential equation (ODE). Choosing $f(x,t)$ form is mostly quite large. That's why usually, the continuity of first and second derivatives of f in respect of x and t is required. Via a variable transformation the original PDE can be reduced to an ODE. The choice of the form of $f(x,t)$ is basically quite large. Usually, the continuity of first and second derivatives of f in respect of x and t is required. Beyond these continuous models based on PDEs, there are numerous purely numerical methods available to study diverse surface growth phenomena. Without completeness, we mention the kinetic Monte Carlo [10], Lattice-Boltzmann simulations [11] and the etching model [12].

5.1. Results without noise term

In our work, the KPZ Eq. (5.1) has been simulated and analyzed using MATLAB R2019a.

$$\frac{\partial h}{\partial t}(x,t) = \nu\nabla^2 h(x,t) + \frac{\lambda}{2}(\nabla h)^2 + \eta(x,t) \tag{5.1}$$

Simulation data during the experiment are the following:

$$x \in [-100, 100],\ t \in [0, 1000],\ N = 100,\ \Delta t = 1/100, \tag{5.2}$$

where N denotes the number of division points on the x-axis and Δt is the time step.

In the resulted figures below the complete solutions of the original PDE (5.1) have been presented showing in different initial condition and various amplitudes. However, for simplicity, the parameters are chosen as $\nu = 0.1\ and\ 2,\ \lambda = 1$ and the initial condition is

$$h(x,0) = \cos\left(\frac{x}{4}\right). \tag{5.3}$$

DOI: 10.14750/ME.2023.031

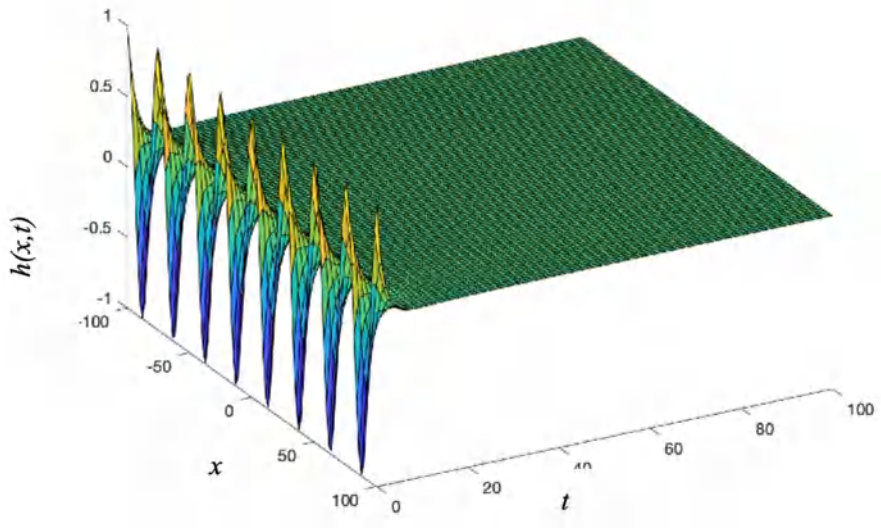

Figure 5.1. Solution to (5.3) KPZ equation without noise term for the parameter set $\nu = 0.1, \lambda = 1$.

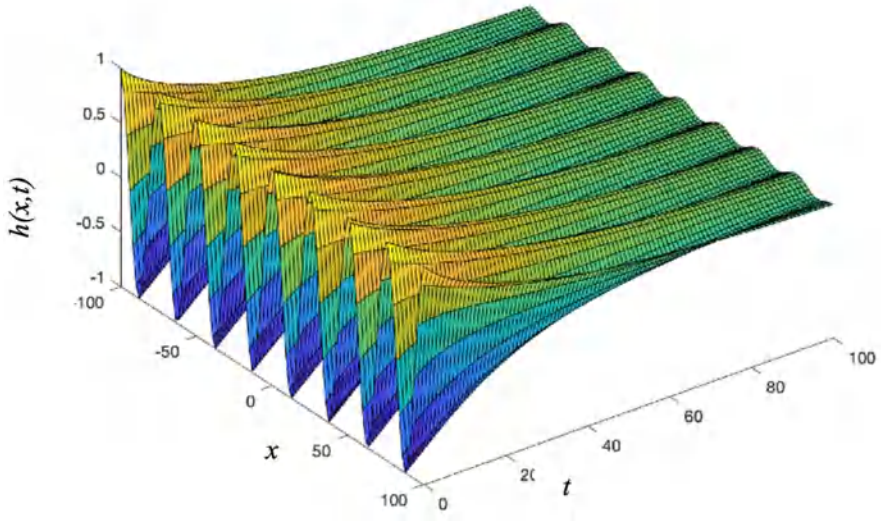

Figure 5.2. Solution to (5.3) KPZ equation without noise term for the parameter set $\nu = 2, \lambda = 1$.

Figures 5.1 and Figure 5.2 present the solutions in the time range $[1, 100]$ with initial condition (5.3). In the simulation result, on Fig. 5.1 the smoothing value is $\nu = 0.1$ and it can be seen that there is only initial condition effect at the beginning of the figure. This wavy surface continues till *t = 10*, then it becomes totally flat surface. Figur 5.2 represents the smoothing value which in our case equals to $\nu = 2$ and the surface waviness decreases slowly. However, this process creates a wavy surface for a long time, resulting in a significantly visible effect of the value ν.

DOI: 10.14750/ME.2023.031

5.2. Results with Gaussian noise

Properly described asymptotic properties include the additive noise equation, which is Gaussian and uncorrelated in time and space [100]. Applying similarity transformation $w(x,t) = f(\zeta)$ and $\zeta = \frac{x}{\sqrt{t}}$ with Gaussian noise gives us the ODE of

$$\nu f''(\zeta) + 0.5 f'(\zeta)[\zeta + \lambda f'(\zeta)] + a e^{\frac{-\zeta^2}{n}} = 0, \quad t > 0, \tag{5.4}$$

where a is in connection with the standard deviation of the Gaussian distribution. There is no general formula available for arbitrary parameters λ, μ, a. That's why there are two parameters fixed e.g. $\lambda = n = 1$ and $\nu = 0.1 \ldots 2$. Then, there is a closed expression (analytical solution) available for the solution

$$f(\zeta) = -\frac{1}{2\lambda} \ln \left[1 + \tan \left\{ \sqrt{\lambda a \pi} \cdot \operatorname{erf}\left(\sqrt{\frac{\zeta}{2}} \right) + c_1 \right\}^2 \right] + c_2, \tag{5.5}$$

where erf means the error function and c_1 and c_2 are integration constants, see [95], [96].

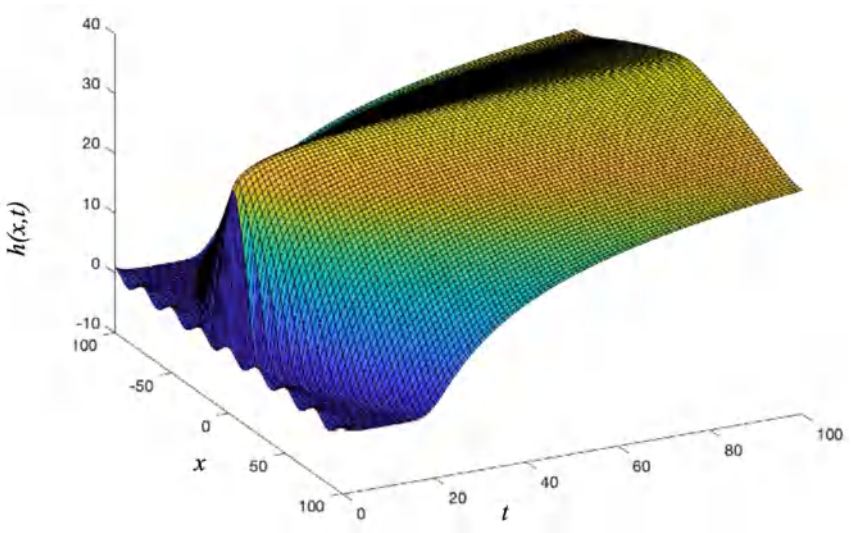

Figure 5.3. Solution to (5.3) KPZ equation without noise term for the parameter set $\nu = 2, \lambda = 1$.

DOI: 10.14750/ME.2023.031

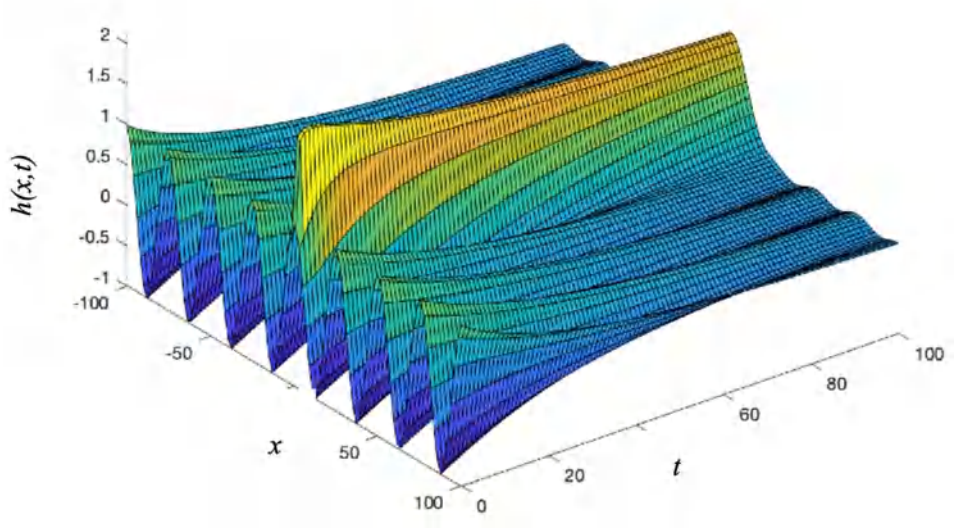

Figure 5.4. Solution to (5.3) The KPZ equation without a noise term was studied for the specified parameters v=2, λ=1.

Figures 5.3 and Figure 5.4 present the solutions in the time range [1, 100] with initial condition (5.3). In the result of simulation Fig. 5.3, the smoothing value is $v = 0.1$ and it can be seen that there is a small initial condition effect at the beginning of the figure then the Gaussian noise effect takes place. The Gaussian noise effect almost has not been affected by the initial condition. However, Figure 5.4 represents the smoothing value when it equals to $v = 2$ showing that surface waviness decreases slowly and effects to the Gaussian noise making it sharper curved. At the same time this process creates wavy surface for long time which gives significantly visible effect of value *v*.

Here, we examined the numerical solutions of (5.1) with MATLAB simulations. The simulation data explain the phenomena observed by the experiments and validate the mathematical model [121]. Thus, the higher coefficient of the second half of Eq. (5.1) ensures the smooth effect of the ripple of the initial condition. In summary, by changing the parameter v appropriately, the effect of the initial condition can be seen for a longer period of time.

5.3. Result with pink noise

Our first case is pink noise term $\eta(x,t) = \frac{a}{w}$.

The Figures 5.5 and 5.6 display the form of the shape function with varying physical parameters. At first, the solutions in both figures look the same. However, there is a significant increase on the Fig. 5.6 in a small time t. In other word the solution has an initial increase when the parameters v and λ are lower. As time goes the surface formation tend to reach flat surface with a small curve in the centre, which shows the pink noise effect along the surface.

DOI: 10.14750/ME.2023.031

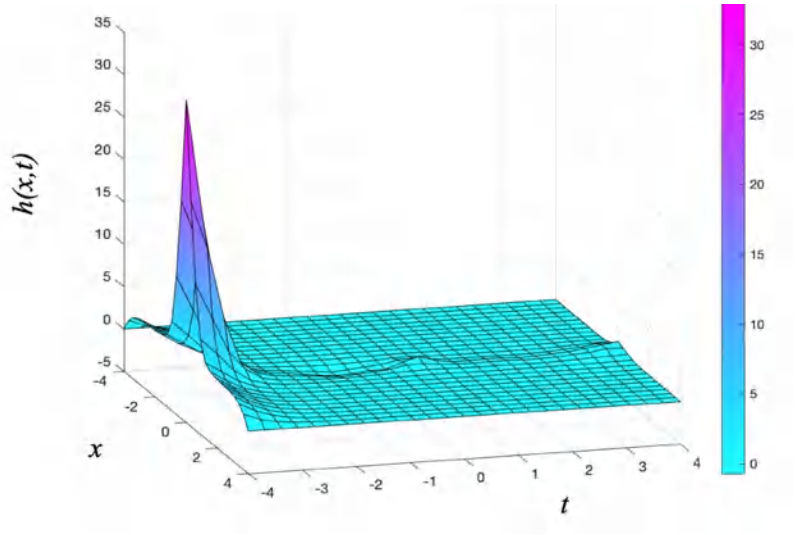

Figure 5.5 The solution of the KPZ equation that includes a pink noise term, for a specific set of parameters v=a=1 and λ=2. Here, initial condition is $h(x,0) = 0$.

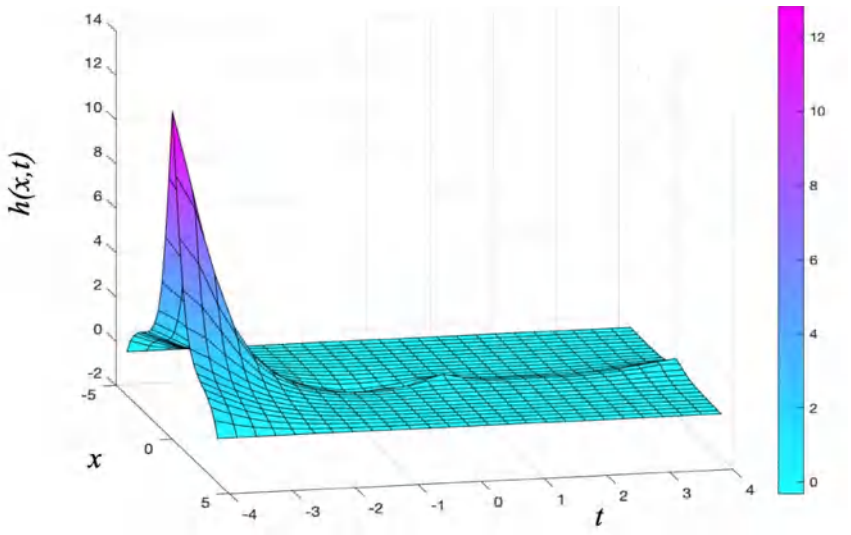

Figure 5.6. The solution of the KPZ equation with pink noise is depicted in figure 5.5, with the specified parameters v=3,a=1 and λ=4. Here, initial condition is $h(x,0) = 0$.

5.4. Result with white noise

Our second case leads to the white noise term $\eta(x,t) = a\, w^0$. Figures 5.7 and 5.8 show the shape for the white noise. The different feature of this noise term from the pink noise is twice higher time of execution. However, when the parameters ν and λ are higher, the behaviour of the initial shape of the function is lower. While this effect reaches an arc shape after in small time t and it continuous on the surface till the end of the time.

DOI: 10.14750/ME.2023.031

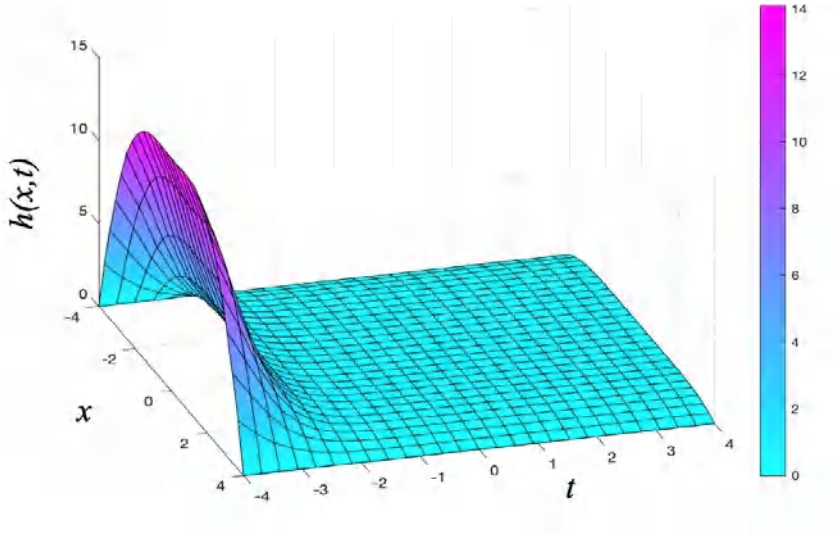

Figure 5.7. The KPZ equation solution with white noise, using the specified set of parameters v=a=1 and λ=2. Here, initial condition is $h(x,0) = 0$.

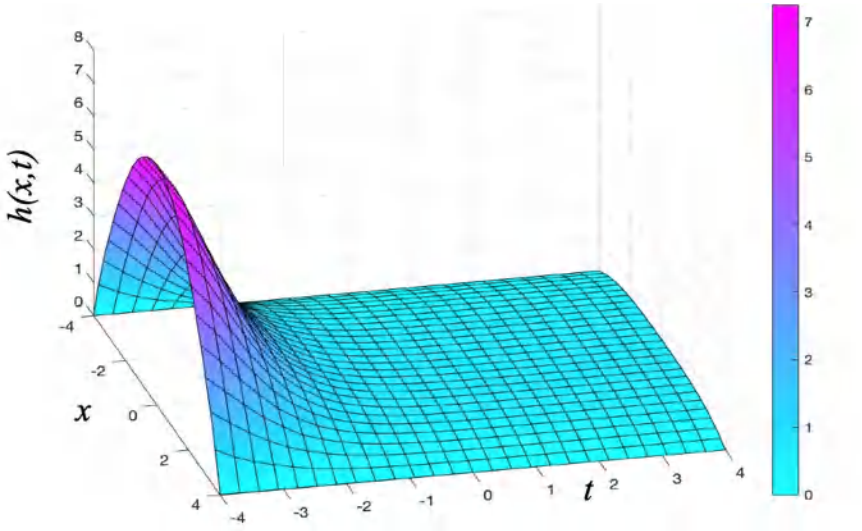

Figure 5.8. The KPZ equation solution with white noise, using the specified set of parameters v=3, a=1 and λ=4. Here, initial condition is $h(x,0) = 0$.

5.5. Result with blue noise

Our next noise term case is $\eta(x,t) = aw$. Figure 5.9 and Figure 5.10 show the solution function $h(x,t)$ of the wavy surface. In the beginning in both figures the initial part of surface is increasing in small time t, however it is various depending on parameters of v and λ as previous simulation results. Here, the effect of blue noise term remains as a wavy surface.

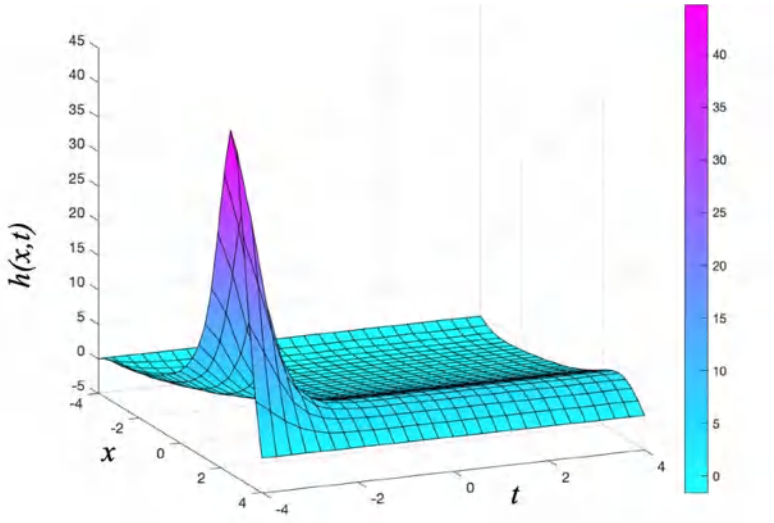

Figure 5.9. The KPZ equation solution with blue noise, using the specified set of parameters v=a=1 and λ=2. Here, initial condition is $h(x,0) = 0$.

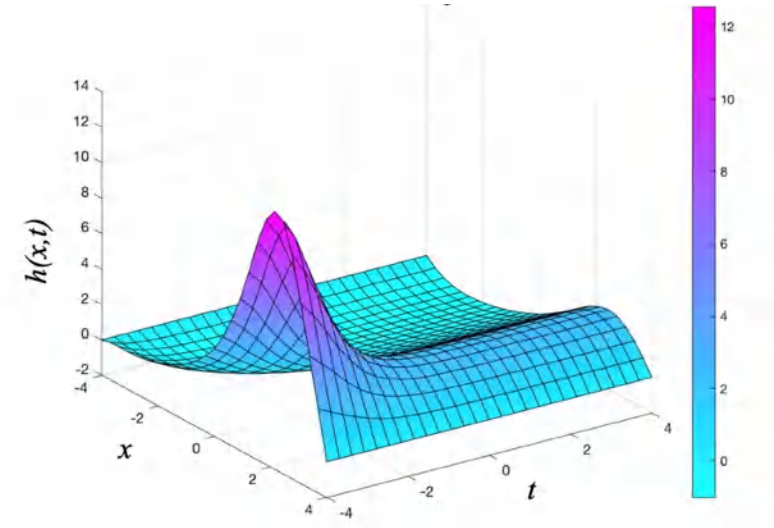

Figure 5.10. The KPZ equation solution with blue noise, using the specified set of parameters v=3, a=1 and λ=4. Here, initial condition is $h(x,0) = 0$.

5.6. Result with Gaussian noise

Our numerical simulation includes Gaussian noise $\eta(x,t) = ae^{-\frac{w^2}{2}}$. Figures 5.11 and 5.12 present the solutions which the features are very similar to formerly investigated research results [122], [123]. Initially, both figures are decreasing from the bell curve to smaller curved surface as time goes on. As it has already been stated that noise terms the parameters of v and λ are playing the same role as previous cases.

DOI: 10.14750/ME.2023.031

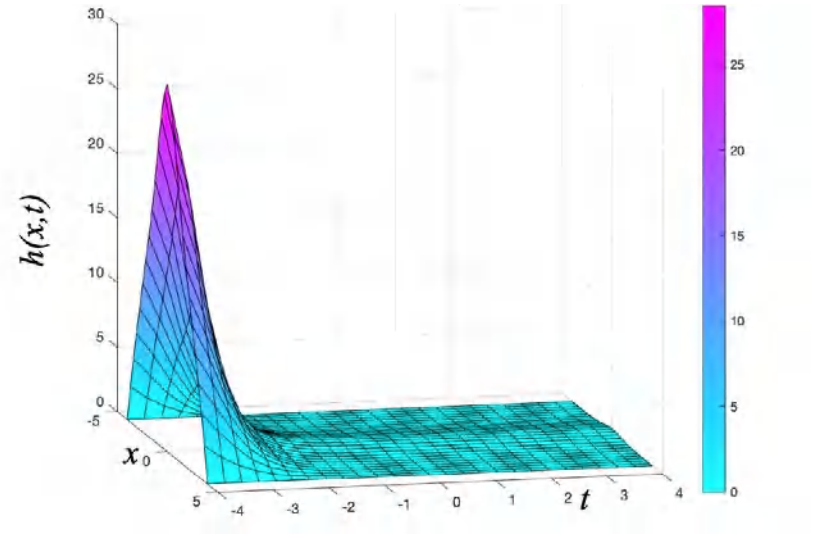

Figure 5.11. The KPZ equation solution with Gaussian noise, using the specified set of v=a=1 and λ=2. Here, initial condition is $h(x,0) = 0$.

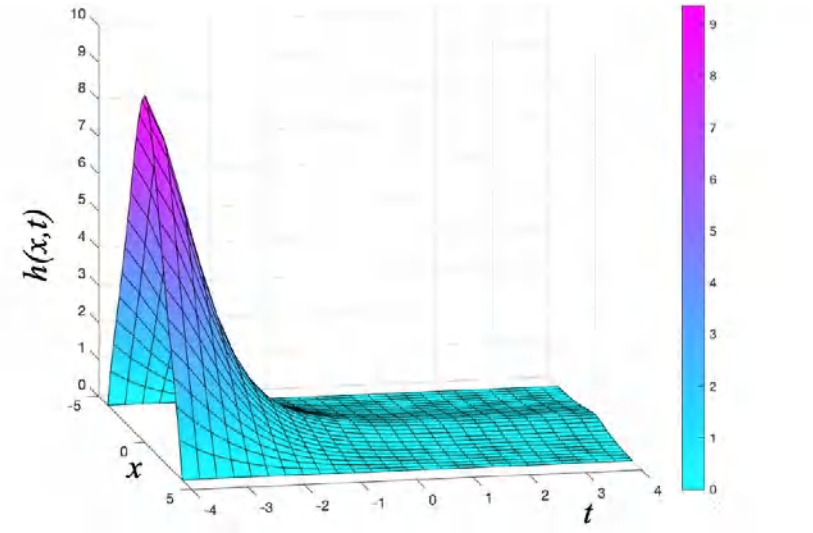

Figure 5.12. The KPZ equation solution with Gaussian noise, using the specified set of v=3, a=1 and λ=4. Here, initial condition is $h(x,0) = 0$.

5.7. Result with Lorentzian noise

As a last system we investigate the Lorentzian noise $\eta(x,t) = \frac{1}{1+w^2}$. In comparison to other noise terms, the Lorentzian noise executed in very small time t and the surface is wavy with high vibrant shape. Despite previous noise term simulation results, this noise term initial formation has not been changed by the parameters of v and λ. Here, only starting point of surface affected and shaped more curved.

DOI: 10.14750/ME.2023.031

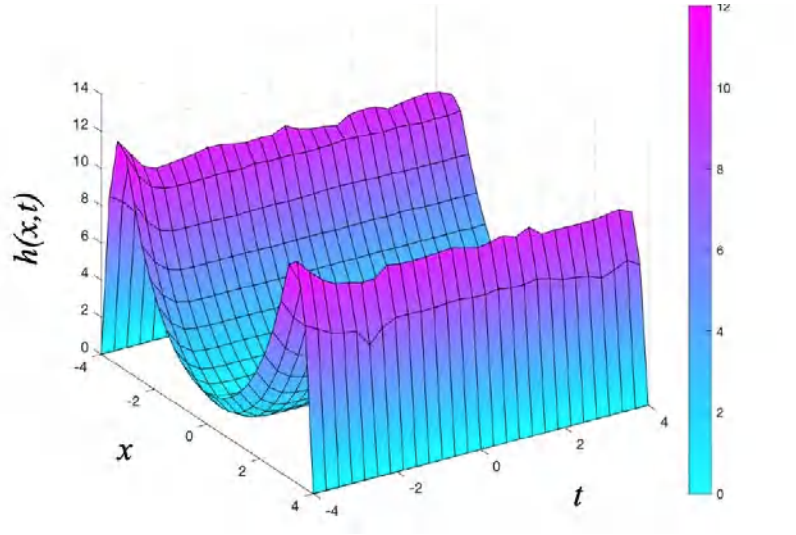

Figure 5.13. The KPZ equation solution with Lorentzian noise, using the specified set of v=a=1 and λ=2. Here, initial condition is $h(x,0) = 0$.

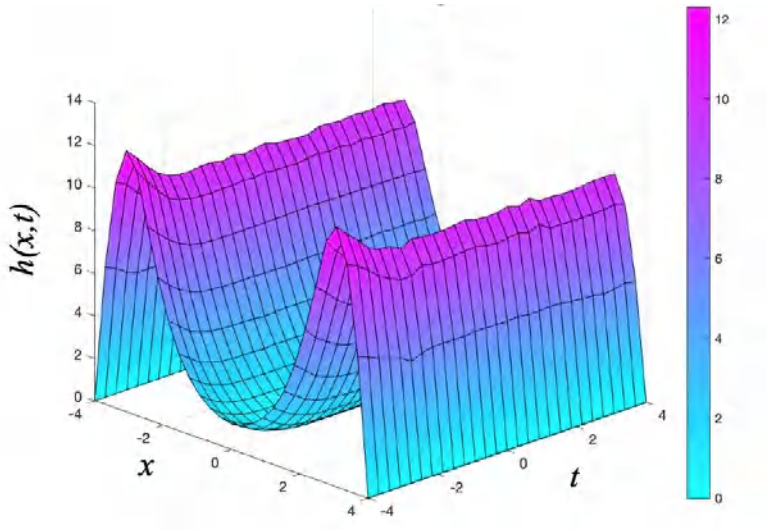

Figure 5.14. The KPZ equation solution with Lorentzian noise, using the specified set of v=3, a=1 and λ=4. Here, initial condition is $h(x,0) = 0$.

In summary, we can say that with an appropriate change of parameter on PDE Toolbox and applying new variables on it, we can numerically simulate the KPZ equation with different noise terms. We analysed three power-law-type noises w^n with exponents of -1, 0, 1, called pink, white and blue noise respectively. Each of them describes completely different dynamics. In addition, we investigated the properties of Gaussian and Lorentzian noises. The parameters of some values are investigated and discussed.

DOI: 10.14750/ME.2023.031

6. SOLUTION METHODS APPLYING DIFFERENTIAL FINITE ELEMENT METHODS

The Kardar–Parisi-Zhang (KPZ) equation (6.1)

$$\frac{\partial h}{\partial t}(x,t) = \nu\nabla^2 h(x,t) + \frac{\lambda}{2}(\nabla h)^2 + \eta(x,t) \tag{6.1}$$

is examined using the recently published leapfrog–hopscotch (LH) method as well as the most standard forward time centered space (FTCS) scheme and the Heun method. The methods are verified by reproducing an analytical solution. The performance of each method is then compared by calculating the average and the maximum differences among the results and displaying the runtimes. Numerical tests show that due to the special symmetry in the time–space discretisation, the new LH method clearly outperforms the other two methods. In addition, we discuss the effect of different parameters on the solutions [124].

6.1. Forward Time Centered Space Scheme

In the paper [6], Moser et al. introduced spatial derivatives of the right-hand side of the KPZ Eq. (2.2). It was discretised using standard forward–backward differences on a cubic (6.2) grid with lattice constant Δx, which is also known as a forward time centred space (FTCS).

$$h_i^{n+1} = h_i^n + r(h_{i+1}^n + h_{i-1}^n - 2h_i^n) + \mu(h_{i+1}^n - h_{i-1}^n)^2 + \Delta t\, k(x,t) \tag{6.2}$$

where Δt is the step size and $t_{i+1} = t_i + \Delta t$, $r = \frac{\upsilon\Delta t}{\Delta x^2}$ and $\mu = \frac{\lambda\Delta t}{8\Delta x^2}$ are the appropriate mesh ratios. We use a for loop going through the nodes to calculate the right-hand side of Eq. (6.1) and omit the old values. We use only one array for the variable *h*, which has as many elements as the number of nodes. However, when we calculate h_i^{n+1}, the value of h_{i-1}^n is still necessary, thus we have to introduce an auxiliary temporary array variable to store the calculated values, and only after the completion of the loop can we load the new values h_i^{n+1} to the array. Therefore, with its speed, the seemingly simplest algorithm can still be surpassed, as we will show later.

6.2. Heun's method

The Heun method is an improved or a modified Euler's method applied in computational science and mathematics. It represents the explicit trapezoidal rule [125], [126], which is a two-stage Runge–Kutta method. This method was originally proposed to solve ordinary differential equations (ODEs) with given initial conditions:

$$y'(t) = f(y(t),t), t(t_0) = y_0. \tag{6.3}$$

The procedure in this case is the following. At the first stage, Heun's method calculates the intermediate value y^{pred} and then the final approximation y^{n+1} at the next integration point:

$$y^{pred} = y^n + hf(t^n, y^n), \tag{6.4}$$

$$y^{n+1} = y^n + \frac{h}{2}[f(t^n, y^n) + f(t^{n+1}, y^{pred})].$$

Although the rate of convergence of Heun's method is two, thus it is usually more accurate than the simple explicit (Euler) method, its Courant–Friedrichs–Lewy (CFL) stability limit is unfortunately the same [127], [128].

The predictor–corrector type that Heun's method applied to the KPZ equation reads as:

$$\begin{aligned} h_j^{pred} &= h_j^n + r\left(h_{j-1}^n + h_{j+1}^n - 2h_j^n\right) + \mu\left(h_{j+1}^n - h_{j-1}^n\right)^2 + k(x, t^n + \Delta t/2)\Delta t \\ h_i^{n+1} &= h_i^n + \frac{r}{2}\left(h_{i-1}^n + h_{i+1}^n - 2h_i^n + h_{j-1}^{pred} + h_{j+1}^{pred} - 2h_j^{pred}\right) \\ &\quad + \mu\left((h_{i+1}^n - h_{i-1}^n)^2 + \left(h_{j+1}^{pred} - h_{j-1}^{pred}\right)^2\right) + k\left(x, t^n + \frac{\Delta t}{2}\right)\Delta, \end{aligned} \tag{6.5}$$

where $\mu = \frac{\lambda \Delta t}{8\Delta x^2}$ and $k(x,t)$ is noise term. When Heun's method is implemented by two for loops, we need not only one extra array to store h_j^{pred}, but a temporary array as in the FTCs method. This makes a time step of Heun's algorithm slower and memory-consuming, although, to a much lesser extent than in the case of implicit methods.

6.3. Leapfrog–Hopscotch method

The leapfrog–hopscotch (LH) structure was first proposed and explained in our recent paper [125]. Similar to the original odd–even hopscotch (OEH) algorithm introduced five decades ago by Gordon [129] and Gourlay [130], one must divide the grid into two subgrids of odd and even nodes (light and dark blue dots in Fig. 6.1, respectively) such that the nearest neighbours of odd nodes are always even and vice versa. The calculation starts with a half-sized time step for the odd nodes using the initial h_i^0 values, symbolised by the green arrows in Fig. 6.1. Then, full time steps are made to calculate alternately the even and the odd nodes (light and dark blue arrows, respectively) until one reaches the final time, where the time step size must also be halved for odd nodes (orange arrows). One can see that in each step, the latest available *u* values of the neighbours (denoted by $h_{i\pm1}^{recent}$) are used, thus the method is explicit. We mention that this LH structure was thoroughly examined for the diffusion equation [125]. According to a large number of numerical experiments, the UPFD formula is optimal for use in the zeroth time step and the symmetric $\theta = {}^1/_2$ formula in all other steps, thus we will apply only these formulas and we will call this concrete method (the LH time–space structure and the formulas) "the LH method". Due to the special symmetry of the time–space discretisation and the $\theta = {}^1/_2$, this method has excellent properties, as we will see in the following.

DOI: 10.14750/ME.2023.031

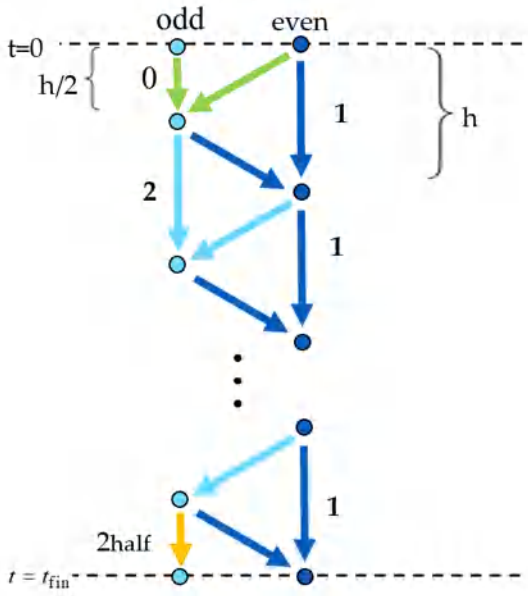

Figure 6.3. The new leapfrog–hopscotch structure.

We express the new value of the *h* variable in the following form in the case of the one space-dimensional KPZ equation [131], [132] at the zeroth step:

$$h_i^{n+1} = \frac{2h_i^n + r(h_{i-1}^{recent} + h_{i+1}^{recent}) + \mu\,(h_{i-1}^{recent} - h_{i+1}^{recent})^2 + k(x, t^n + \Delta t/2)\Delta t}{2(1+r)} \tag{6.6}$$

and at all other steps (denoted by 6.1and 6.2 in Fig. 6.1.):

$$h_i^{n+1} = \frac{(1-r)h_i^n + r(h_{i-1}^{recent} + h_{i+1}^{recent}) + \mu\,(h_{i-1}^{recent} - h_{i+1}^{recent})^2 + k(x, t^n + \Delta t/2)\Delta t}{1+r} \tag{6.7}$$

except the last, which is a half time step thus the substitution $\Delta t \to {}^{\Delta t}/_{2}, r \to {}^{r}/_{2}, \mu \to {}^{\mu}/_{2}$ must be performed in Eq. (6.7). We note that if $\mu = 0$ and $k = 0$ then one obtains back the original LH method's form developed for the diffusion equation. One can see that due to the time–space structure, the LH method does not use any extra arrays for the temporary values of *h*, and that is why it has less memory requirement, and it can be slightly faster than the simplest FTCS method.

6.4. Stability considerations

Since the conventional explicit methods have severe stability problems, usually implicit methods are used to solve the linear diffusion equation and most of its nonlinear modifications. For example, the explicit Euler (FTCS) is stable for the linear diffusion equation with coefficient ν only if the time step size is small enough, i.e., $\frac{\nu \Delta t}{\Delta x^2} \leq \frac{1}{2}$ (this is also called the CFL limit). However, implicit methods not only require more computational effort (especially in the nonlinear case), but they are very slow and memory consuming in the case of a large number of nodes/cells and if the matrix is not tridiagonal, which is always true in 2 or more space dimensions.

In [125], we analytically proved and numerically demonstrated that the new LH method is unconditionally stable for the linear diffusion equation, and it has roughly the same accuracy as Heun's method. The LH method is almost as accurate for stiff systems as the implicit Crank–Nicolson scheme, but it is much faster. This encouraged us to adapt the LH method to the KPZ equation.

However, the KPZ equation contains a nonlinear term with coupling coefficient λ and a noise term, besides the linear diffusion term. Dasgupta et al. showed [16] that in the discretised model, isolated pillars or grooves are prone to increase indefinitely if their height exceeds a critical value, which depends on a single parameter proportional to $\lambda\sqrt{A/\nu^3}$, where A is the amplitude of the noise term. They argued that this instability is inherent in the numerical treatment due to the space discretisation of the continuous equation. Our observations reinforce these findings in the case of the LH method as well, but the systematic examination of the probability of the appearance of these instabilities is out of the scope of this paper.

What we stress here is that we are talking about two qualitatively different kinds of instabilities. In the original continuous equation, the nonlinear term yields the growth of pillars and grooves, while the diffusion tries to smooth them out. However, in the case of the conventional explicit schemes, the diffusion itself also causes instability. The LH method is close to being ideal from this point of view as well: stronger diffusion means faster smoothing and thus increased stability.

6.5. Verification using an analitical solution

If we introduce the variable $\omega = x + ct$, then Eq. (6.1) with the Brownian noise term can be written as follows:

$$\frac{\partial h(x,t)}{\partial t} = \upsilon\nabla^2 h + \frac{\lambda}{2}(\nabla h)^2 + \frac{a}{\omega^2}. \tag{6.8}$$

For verification, we reproduce the following recently published analytical solution to Eq. (6.7) [96]:

$$h^{\text{exact}}(\omega) = \frac{1}{\lambda}\left\{c\omega + \nu\, ln\left(\frac{\lambda^2 I_d(\varphi)^2}{c^2\omega\left[K_d(\varphi)I_{d-1}(\varphi)+I_d(\varphi)K_{d+\frac{1}{2}}(\varphi)\right]^2}\right)\right\}, \tag{6.9}$$

where a, c=const., $\varphi = \frac{c\omega}{2\nu}$, while $I_d(\varphi)$ and $K_d(\varphi)$ are the modified Bessel functions of the first and the second kind with the subscript of $d = \frac{\sqrt{\nu^2-2a\lambda}}{2\nu}$.

The following parameters are used in the numerical calculation:

$$\nu = 1,\ \lambda = 6,\ a = 0.05,\ c = 1, x \in [0,6],\ t \in [1,2]. \tag{6.10}$$

The number of space nodes is 300, thus the space step size is $\Delta x = 0.02$.

For the initial and the boundary conditions, the analytical solution is used at t = 1 as the initial condition and the Dirichlet boundary conditions are taken at the edges of the spatial interval. We

DOI: 10.14750/ME.2023.031

note that the evaluation of the modified Bessel functions to obtain the initial and the boundary conditions was by far the most time consuming part of the code.

The (global) numerical error function is the absolute difference of the numerical solutions u_j^{num} produced by the examined method and the analytical solution $h_j^{\text{exact}} = h^{\text{exact}}(x = x_j)$ at the final time. We use these errors of the nodes to calculate the maximum error:

$$\text{Error}(L_\infty) = \max_{1 \le j \le N} \left| u_j^{\text{exact}}(t = 2) - u_j^{\text{num}}(t = 2) \right|. \tag{6.11}$$

The L_∞ errors as a function of the time step size h can be seen in Fig. 6.2.

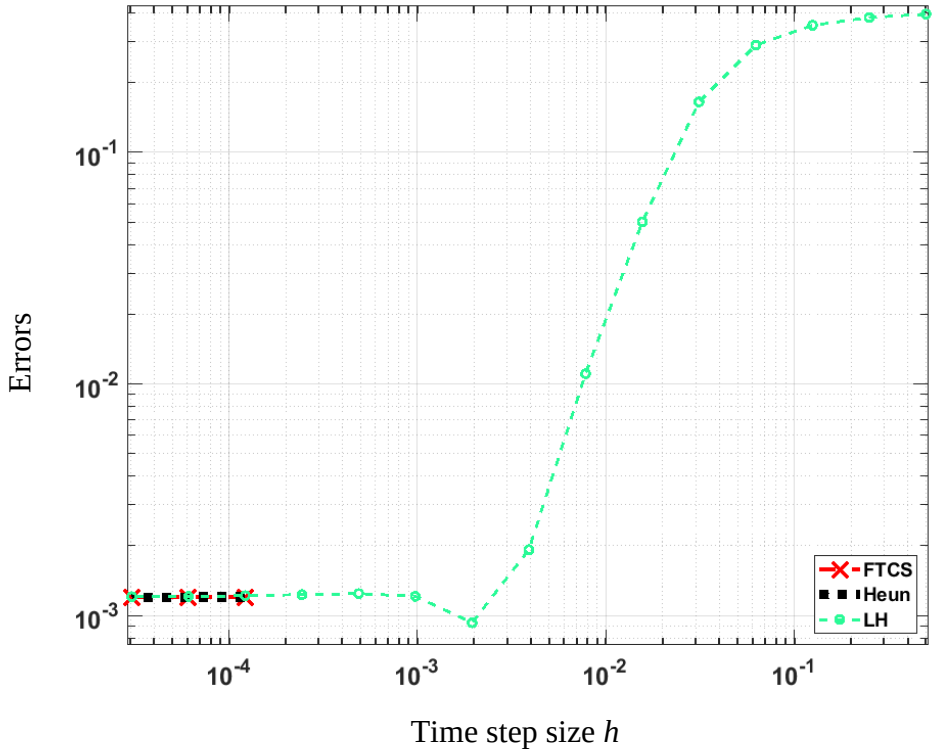

Figure 6.2. The L_∞ errors as a function of time step size Δt for the numerical solutions of Eq. (6.1) in case of the standard FTCS scheme, the Heun method and the Leapfrog–hopscotch method.

One can see that the LH method reaches the minimum error (determined by space discretisation) at about 2×10^{-3}, while the FTCS and the Heun methods are unstable above 2×10^{-4}. It means that the LH method can be safely used with an order of magnitude larger time step sizes than the examined conventional methods.

6.6. Comparison of different methods

We continue the investigation in those cases where the analytical solution is not known. The spatial length of the simulated system is $L = 32$, so $x \in [0, 32]$, while the space step size is $\Delta x = 0.01$, thus the number of nodes is $Nx = 3201$. In order to minimise the effect of the

boundaries, we wanted to use periodic boundary conditions. However, the noise terms are not periodic functions of space, therefore we constructed a special modification of the periodic boundary conditions, when the previous (left) and the following (right) copy of the system is not only shifted but mirrored as well. It is implemented by taking $h_1 = h_3$ and $h_{N_x} = h_{N_x-2}$ in the case of each method.

The initial time of the simulation is $t_{in} = 0.01$ (note that the term $x + ct$ is present in the denominator of the Brownian noise term, thus *x* and *t* cannot be zero at the same time), and the final time is $t_{fin} = 0.1, 1$ or 10. The time step size is chosen as 10^{-5} for the FTCS and the Heun methods, but it is 10^{-5} and 10^{-4} for the LH method. In this section we fix the parameters as follows:

$$\nu = 1,\ \lambda = 6,\ a = 1,\ c = 1 \tag{6.12}$$

In our previous research works [36,37], we used different initial conditions with different amplitudes for Eq. (6.1). Here, all numerical simulations for each scheme were performed with the same initial condition $h(x, 0)$.

$$h(x, t = 0) = \sin\left(\pi \cdot \frac{x}{4}\right) + \cos\left(\pi \cdot \frac{x}{4}\right) \tag{6.13}$$

For the simulations to measure the running times, we used a laptop computer (ASUS, Taiwan) with a 2.6 GHz Intel I CITM i7-10750H CPU, 8.0 GB RAM with the MATLAB R2020b software(The MathWorks, Inc. USA) in which there was a built in tic-toc function to measure the total running time of the tested algorithms.

For all three methods, with the parameters given in Eq. (6.1), the simulations were performed and the results are presented in Fig. 6.3.

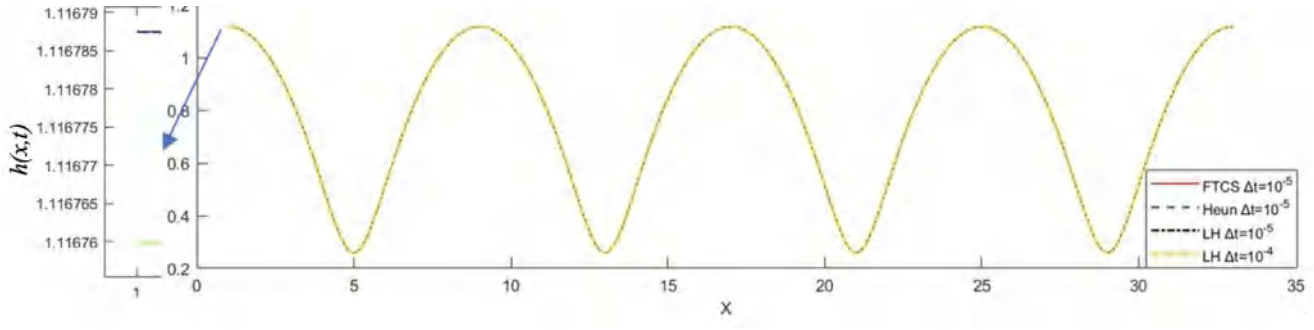

Figure 6.3. Comparison of three different methods with various parameters in Eq. (6.12). The final time is $t_{fin} = 1$.

One can see in Fig. 6.3 that the curves are indistinguishable, which means that each method is accurate. The (global) numerical difference is the absolute difference of the numerical solutions h_i^{num} produced by the examined methods at final time t_{fin} for the KPZ equation: the FTCS scheme, the Heun method and the LH method for 10^{-5} and 10^{-4} time step size. For brevity, we denote this latter case, the LH method with 10^{-4} time step size as LH*.

In order to find an individual difference in the nodes or cells, we calculate the maximum and the average differences in the following ways:

DOI: 10.14750/ME.2023.031

$$D_i^{\mathrm{FTCS,Heun}} = \left| h_i^{\mathrm{FTCS}} - h_i^{\mathrm{Heun}} \right|, \quad D_i^{\mathrm{FTCS,LH}} = \left| h_i^{\mathrm{FTCS}} - h_i^{\mathrm{LH}} \right|, \quad D_i^{\mathrm{Heun,LH}} = \left| h_i^{\mathrm{Heun}} - h_i^{\mathrm{LH}} \right|, \tag{6.14}$$

Average differences (L_1 errors)

$$L_1^{FTCS,Heun} = \sum_i \frac{D_i^{FTCS,Heun}}{Nx}, \quad L_1^{LH,LH*} = \sum_i \frac{D_i^{LH,LH*}}{Nx}, \text{ etc.} \tag{6.15}$$

Maximum differences (L_∞ errors)

$$L_\infty^{FTCS,Heun} = \max_i \{D_i^{FTCS,Heun}\}, \; L_\infty^{LH,LH*} = \max_i \{D_i^{LH,LH*}\}, \text{ etc.} \tag{6.16}$$

In Tables 6.1 and 6.2, we show the average and the maximum differences of the methods, namely the FTCS, the Heun and the LH with two different time step sizes Δt. It is clear that due to enhanced stability, the LH method can be used with larger time step sizes for further investigation of the KPZ equation.

Table 6.1. Average difference without noise term.

t_{fin}	$L_1^{FTCS,Heun}$	$L_1^{FTCS,LH}$	$L_1^{Heun,LH}$	$L_1^{FTCS,LH*}$	$L_1^{Heun,LH*}$	$L_1^{LH,LH*}$
0.1	$3.48 \cdot 10^{-7}$	$3.47 \cdot 10^{-7}$	$2.70 \cdot 10^{-9}$	$3.86 \cdot 10^{-4}$	$3.88 \cdot 10^{-4}$	$3.88 \cdot 10^{-4}$
1	$5.45 \cdot 10^{-7}$	$5.42 \cdot 10^{-7}$	$2.45 \cdot 10^{-9}$	$4.30 \cdot 10^{-5}$	$4.34 \cdot 10^{-5}$	$4.34 \cdot 10^{-5}$
10	$3.20 \cdot 10^{-7}$	$3.19 \cdot 10^{-7}$	$1.10 \cdot 10^{-9}$	$3.20 \cdot 10^{-7}$	$8.38 \cdot 10^{-8}$	$8.38 \cdot 10^{-8}$

Table 6.2. Maximum difference without noise term.

t_{fin}	$\max_i\{D_i^{FTCS,Heun}\}$	$\max_i\{D_i^{FTCS,LH}\}$	$\max_i\{D_i^{Heun,LH}\}$	$\max_i\{D_i^{FTCS,LH*}\}$	$\max_i\{D_i^{Heun,LH*}\}$	$\max_i\{D_i^{LH,LH*}\}$
0.1	$6.91 \cdot 10^{-7}$	$6.93 \cdot 10^{-7}$	$8.56 \cdot 10^{-9}$	$6.66 \cdot 10^{-4}$	$6.66 \cdot 10^{-4}$	$6.66 \cdot 10^{-4}$
1	$1.32 \cdot 10^{-6}$	$1.31 \cdot 10^{-6}$	$6.57 \cdot 10^{-9}$	$1.47 \cdot 10^{-4}$	$1.48 \cdot 10^{-4}$	$1.48 \cdot 10^{-4}$
10	$3.24 \cdot 10^{-7}$	$3.23 \cdot 10^{-7}$	$1.12 \cdot 10^{-9}$	$4.66 \cdot 10^{-7}$	$1.52 \cdot 10^{-7}$	$1.51 \cdot 10^{-7}$

In addition, the total running time of the tested algorithms is presented in Table 6.3. It is shown that in various time t, the method's running time is different and the fastest is the leapfrog–hopscotch method for any time length. It is slightly faster than the FTCs method with the same time step size, as we mentioned before.

Table 6.3. Running time differences between the methods.

Methods	Running Time (s)		
	$t_{fin} = 0.1$	$t_{fin} = 1.0$	$t_{fin} = 10.0$
FTCS method, $\Delta t = 10^{-5}$	0.3232	2.9663	28.6288
Heun's method, $\Delta t = 10^{-5}$	0.6573	6.2133	73.8652

DOI: 10.14750/ME.2023.031

LH method, $\Delta t = 10^{-5}$	0.3135	2.5480	24.4324
LH method, $\Delta t = 10^{-4}$	0.0825	0.3105	2.4560

Note that when the time step size Δt is larger than 10^{-5}, the methods are unstable except for the LH method. This proves that our new method is not only the fastest, but also more stable even in larger time steps Δt. This numerical experiment demonstrated again that this new explicit method is very effective for the KPZ equation. We think that it will be very promising, especially in two or three space-dimensional numerical experiments since they include a large amount of the nodes or cells.

6.7. Impact of different parameter values (without noise term)

In this section, we investigate the effect of different parameters, such as the coefficient ν, λ, a and t_{fin}. When one of the parameters are changed, all other parameters are fixed: $\nu = 1,\ \lambda = 6,\ a = 1$ and different final times t_{fin} are used. For the sake of verification, we still use not only the LH, but the FTCS and Heun's methods as well.

Figure 6.4 illustrates the solutions obtained with different methods for the linear diffusion parameter ν. It is clear that increasing the strength of the diffusion decreases the waviness of the surface. We note that when $\nu = 6.0$, the traditional methods (FTCS and Heun) are unstable, and they cannot be used even with this small time step size.

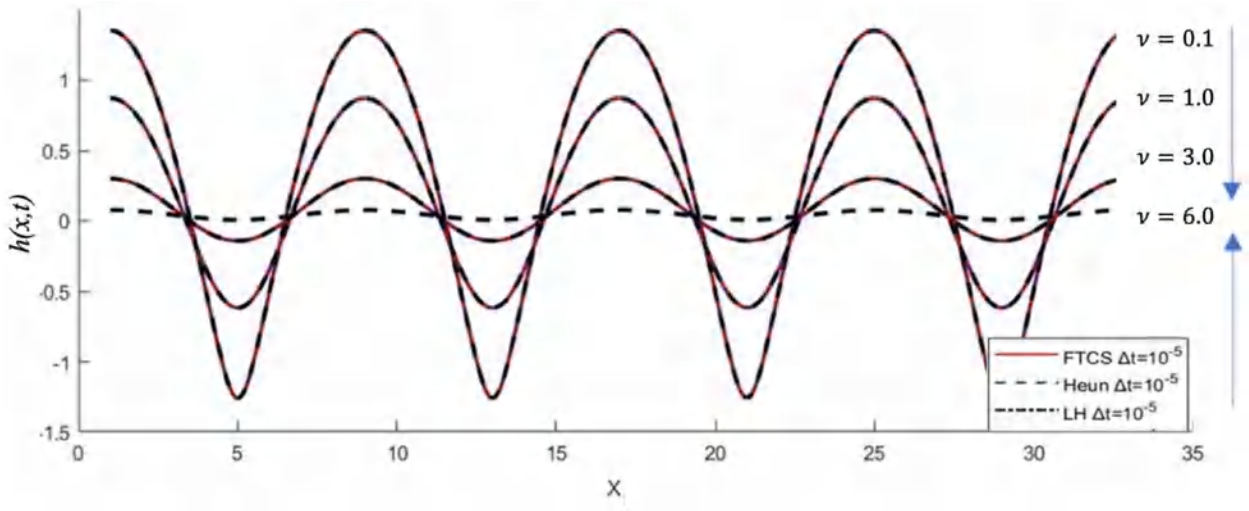

Figure 6.4. Numerical simulation of h for different diffusion coefficients υ with three methods.

In Fig. 6.5, we illustrate the behaviour as a function of the nonlinear term parameter λ for final time $t_{fin} = 1$. One can see that the function is shifting to higher levels when the coefficient of the nonlinear term λ is increasing and the waviness of the function decreases.

DOI: 10.14750/ME.2023.031

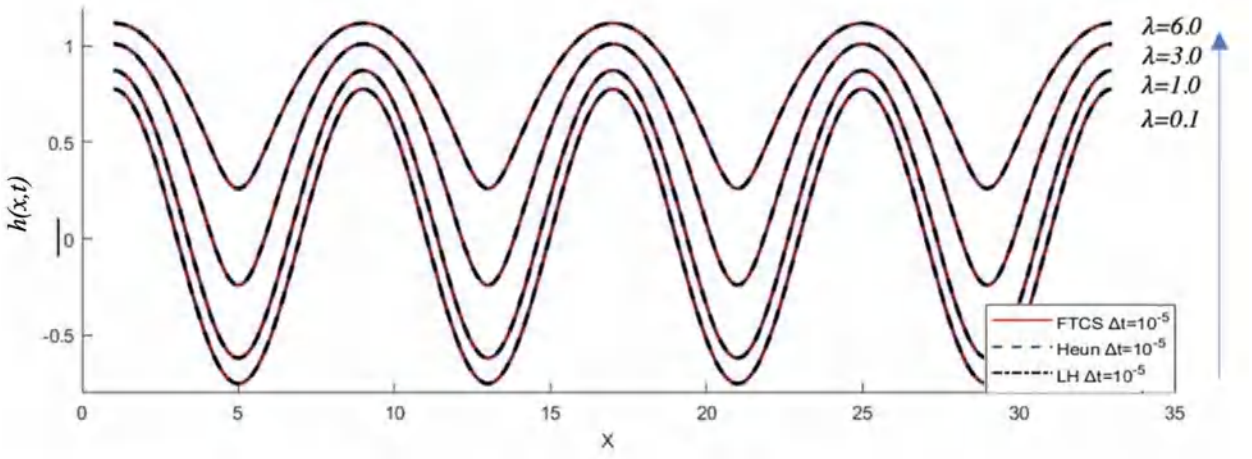

Figure 6.5. Numerical simulation of h for different nonlinear term coefficients λ with three methods.

Here, we are interested in the effect of the time on the used methods. In Fig. 6.6, we present the numerical solution of the discretised KPZ equation for different final times. Therefore, we perform the simulation for three different final times $t_{fin} = 0.1, 1.0$ and 10 with the parameters given in Eq. (6.12). One can conclude that the waviness of the surface is decreasing as time elapses.

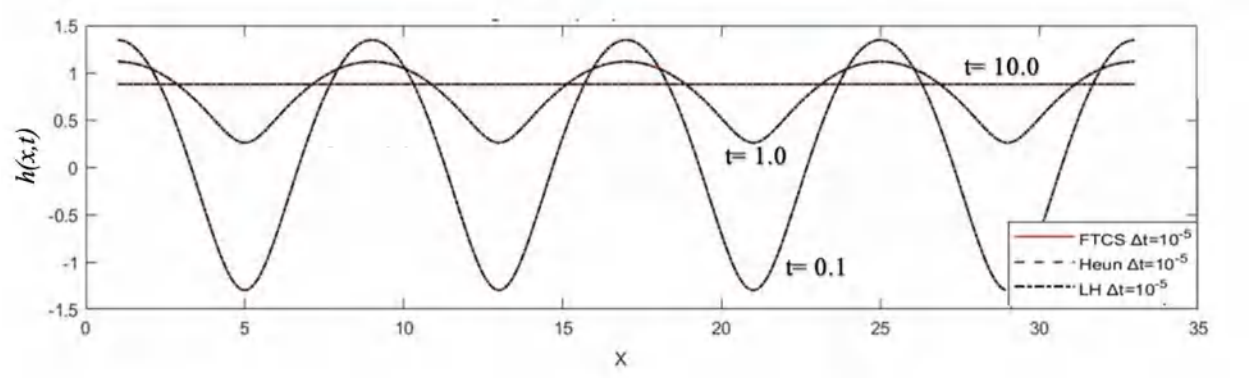

Figure 6.6. Numerical simulation of the system different time t with various methods

After examining each method with various parameters, we have more information on how the surface formation occurs. In the simulations, each increased parameter decreases the waviness of the function. However, as we mentioned above, if the linear term parameter has a higher value ($\nu \geq 6$), then only the LH method is stable, while the FTCS and Heun's methods are not stable.

6.8. Comparison of various noise term effects

Once we verified and proved the most stable method, we used the leapfrog–hopscotch method to numerically solve the KPZ equation with different noise terms and various parameters. In our previous works, we analysed the solutions with the noise term $k(\omega) = a\omega^2$ [95], [96]. In our current numerical simulation, we examine Gaussian noise term $ae^{-\omega^2}$ and Brownian noise term a/ω^2 when all the physical parameters are set as in Eq. (6.17). However, some parameters

DOI: 10.14750/ME.2023.031

are investigated separately to show their effect on the solution and to show their effect on the system. If not explicitly stated otherwise, the values of the parameters will be the following:

$$\nu = 1,\ \lambda = 1,\ a = 1,\ c = 1, \Delta t = 10^{-5} \tag{6.17}$$

Figure 6.7 shows that the Brownian noise term's effect is higher than the Gaussian noise term. In this simulation, the amplitude of the noise terms is $a = 1$ in both cases. The Brownian noise function k has quite a high value that is close to the origin due to the small values of x and t in the denominator, thus it remarkably raises the function h at the left side of the figure, but this effect vanishes for larger values of x. On the other hand, the h function in the case of the Gaussian noise is only slightly different than h without a noise term, even for $x = 0$.

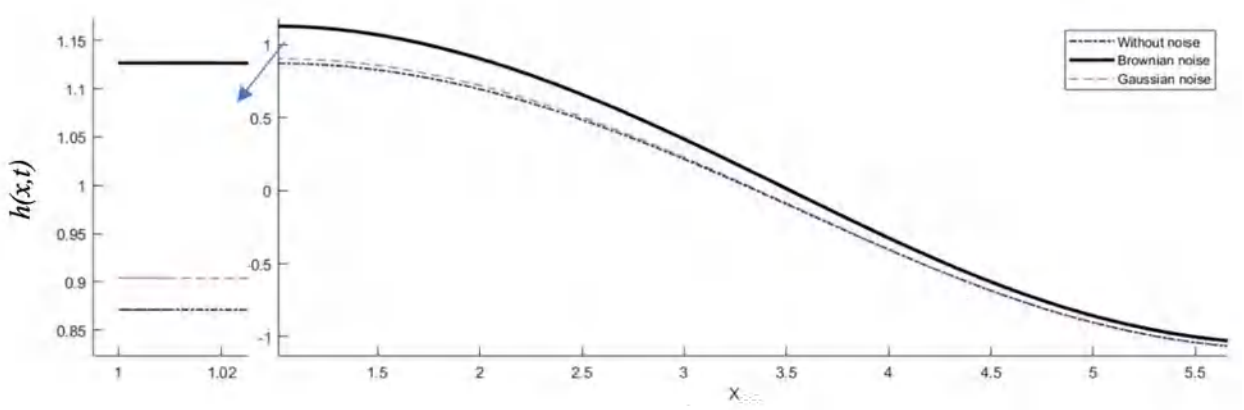

Figure 6.7. Numerical simulation results of leapfrog–hopscotch discretised methods with various noise term effects in time $t_{fin} = 1$. The time step size is $\Delta t = 10^{-5}$.

We increased the time t_{fin} of the simulation from 1 to 10. In this case, we see from Fig. 6.8 that the effect of the Brownian noise term is again much stronger than the Gaussian noise term and the elevation on the left side requires a longer length of x to reach the non-elevated surface (right side of the figure) without a noise term. Similarly to the previous result in Fig. 6.7, the function h in case of Gaussian noise is slightly smoother and the effect of the noise is small.

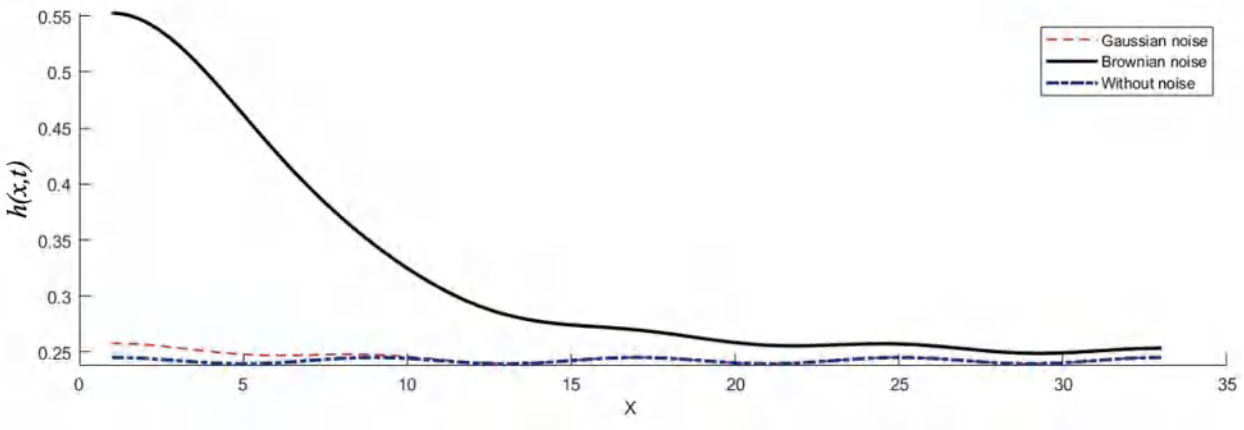

Figure 6.8. Numerical simulation results of the leapfrog–hopscotch method with various noise term effect in time $t_{fin} = 10$. The time step size is $\Delta t = 10^{-5}$.

As stated above, the noise term has significant effects on the system. Therefore, we performed our method with a higher amplitude than $a = 1$. We fixed the amplitude as $a = 10.0$ and it was simulated with all the noises. Figure 6.9 for $t_{fin} = 1$ and Fig. 6.10 for $t_{fin} = 10$ show that when the noise term amplitude is high, the results are different. However, the effect of Brownian noise is again much stronger than Gaussian noise. This proves that noise term amplitude plays a crucial role in the simulation result.

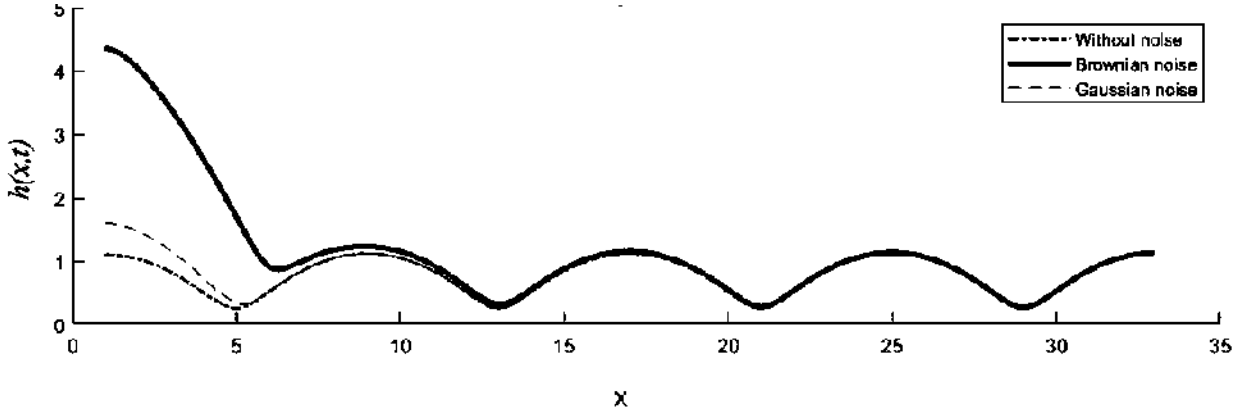

Figure 6.9. Numerical simulation results of the leapfrog–hopscotch method in case of various noise term effects with amplitude a=10.0. The time step size is $\Delta t = 10^{-5}$ *and the final time is* $t_{fin} = 1$.

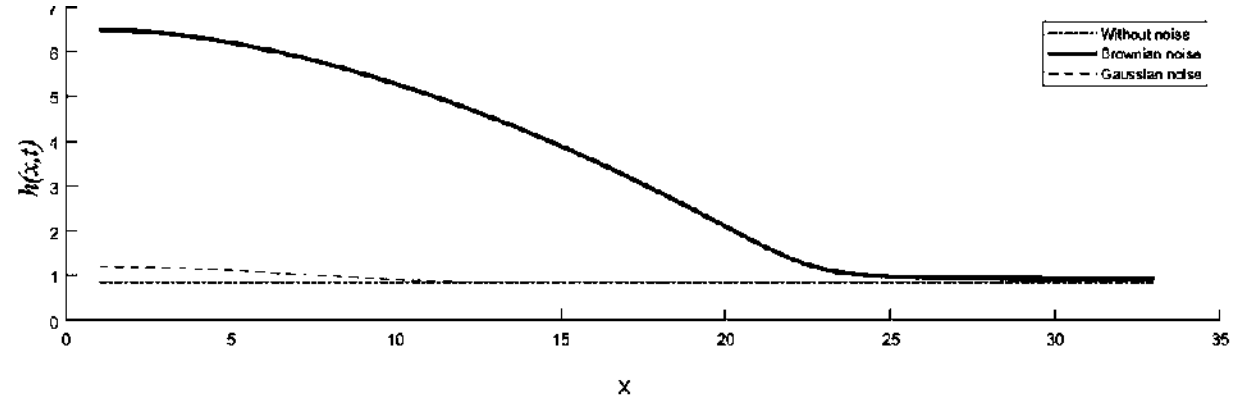

Figure 6.10. Numerical simulation results of various noise term effects with the amplitude a=10.0 and $t_{fin} = 10$ *obtained by the leapfrog–hopscotch method. The time step size is* $\Delta t = 10^{-4}$.

We have already discussed the average/maximum differences without noise terms and we presented all of the obtained results in Tables 6.1-3. We have seen that the LH* method (LH method with increased time step size) is very accurate for a large final time. Therefore, we now simulate surface growth by the LH* method with different noise terms in longer time $t_{fin} = 10$ to see the effect of the amplitude to the smaller time stem size. As a result, the effect of the Brownian noise is significantly stronger than that of the Gaussian, which has only a slight effect, approximately $x = 0$ compared to the case without the noise term. Compared to Fig. 6.9, we see

DOI: 10.14750/ME.2023.031

that due to the longer final time - and without the noise member functions - its height is low for Gaussian. However, the function *k* in the case of the Brownian noise term is even higher due to the longer simulation time $t_{fin} = 10$.

We demonstrated in Fig. 6.9 that the effect of the increased (linear) diffusion term parameter ν is decreased surface waviness. Now, we present the effect of the parameters ν and λ on the method when the value of the diffusion term is large, $\nu = 3.0$ and the value of the nonlinear term is small, $\lambda = 0.1$. In Fig. 6.10, one can see that the shape of the surface is very close to a sine wave and the increased linear term parameter υ changes Brownian noise but not the Gaussian noise term.

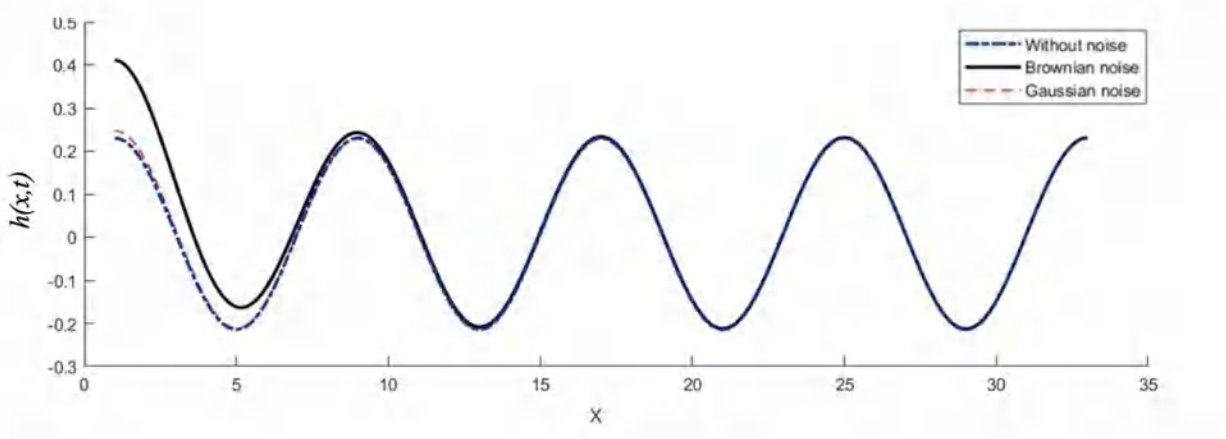

Figure 6.11. Numerical simulation results of leapfrog–hopscotch methods in case of various noise terms with increased diffusion: ν=3.0 and λ=0.1. The time step size is $\Delta t = 10^{-5}$ *and the final time ist*$_{fin} = 1$.

In Fig. 6.11, we fixed all other parameters as in Eq. (6.8) but only linear and nonlinear terms are changed to a very small value of υ and to a large value of λ. The effect is slightly similar to that in Fig. 6.5. However, due to the small value of ν and the large value of λ, the bottoms of the wavy surface became very narrow valleys.

DOI: 10.14750/ME.2023.031

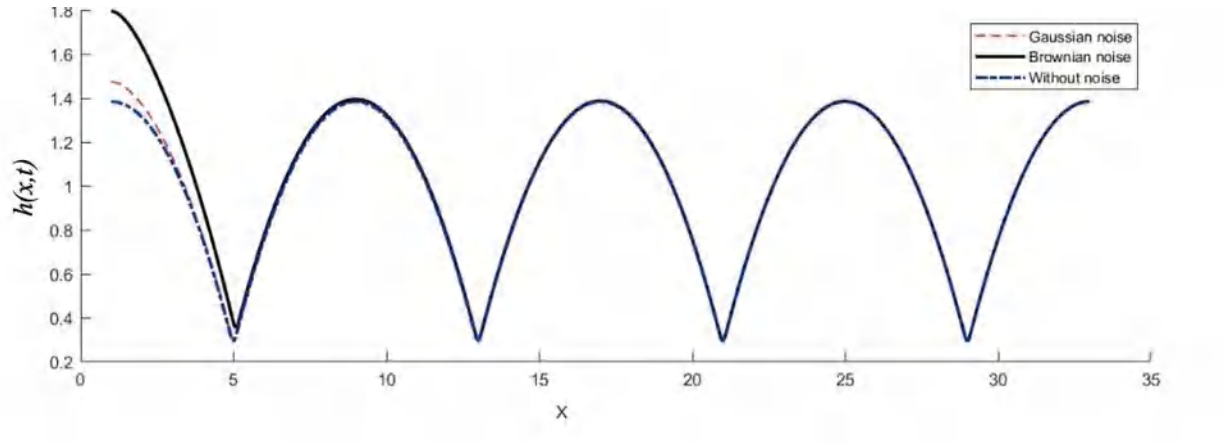

Figure 6.12. Numerical simulation results of leapfrog–hopscotch methods in case of various noise term effect with decreased diffusion υ=0.1 and increased nonlinear parameter λ=6.0. The time step size is $\Delta t = 10^{-5}$ *and the final time is* $t_{fin} = 1$.

The most standard FTCS scheme, the well-known Heun method and the recently invented leapfrog–hopscotch method are used to solve the KPZ equation in one spatial dimension. We have validated all methods using an analytical solution, and we compared the performance of these methods in cases of different parameters. We found that FTCS and the Heun's methods are usually unstable above $\Delta t = 2 \times 10^{-5}$ (the concrete threshold for stability depends on the parameters), while the LH method was stable in all of the presented numerical experiments. It can be unstable only if the nonlinear coupling term λ are much higher than the linear coefficient υ and/or there are spike-like pillars or grooves. Therefore, even if the LH method is not unconditionally stable for the KPZ equation, it is obvious that it has much better stability properties than the conventional explicit methods.

The effect of the parameters on the solution for the KPZ equation, and most importantly the coefficients in the equation, have been examined. The newly proposed LH method has been used without noise and with Gaussian and Brownian noise terms to show the effect of the noise terms for fixed parameters. In addition, we have simulated two different noise terms with different parameters such as ν linear, λ nonlinear and a noise term amplitude parameters. The effect of each applied parameter has been presented and discussed.

DOI: 10.14750/ME.2023.031

7. EXAMINATION OF THE WIDTH FUNCTION

7.1. Width function

The main attention of our work is the examination of the solutions to the KPZ equation in 1+1 dimension and the mean surface width or interface roughness of the height profile defined by

$$W(L,t) = \sqrt{\frac{1}{L}\int_0^L [h(x,t) - \langle h(L,t)\rangle]^2 dx}, \tag{7.1}$$

where $\langle h(L,t)\rangle = \int_0^L h(x,t)dx/L$ denotes the mean height at time t. For finite L,

this quantity shows the scaling behaviour of many growth processes introduced by Family and Vicsek [82] [83]

$$W(L,t) = L^{\alpha} W\left(\frac{t}{L^z}\right) \tag{7.2}$$

with the dynamical exponent z and the roughness exponent α. The scaling function has the limits $\mathrm{W}(y) \to 1$ for $y \to \infty$ and $\mathrm{W}(y) \sim y^{\beta}$ for $y \ll 1$ as $y = \frac{t}{L^z}$ The exponent β called growth exponent is given by $\beta = \alpha/z$. The saturation scales are as L^z, and the saturation width is proportional to L^{α} [10]. In 1+1 dimension, the KPZ equation holds $\alpha = 1/2$ and $z = 3/2$, thus, verifying the general Galilean invariance scaling relation $\alpha + z = 2$ [25]. The ratio of these values yields $\beta = 1/3$.

Our aim is to use the discretized KPZ equation as in [49] to explore different surface formations and roughnesses. We wish to study the role of linear term parameter ν and the non-linear parameter λ on the growth formations. In addition, we investigate the surface roughness during different linear system sizes L . In the past, most of the research on stochastic control has been concerned with theoretical models that suppress the non-linearity either entirely or partially [84] [85] [86] [87] [88]. Avoiding or minimizing the effect of the non-linearity is necessary during the numerical simulation process to avoid or minimize the effect on both the dynamic and steady-state properties. In previous works [88] [89] [90], a method to control the non-linear term using exponential decreasing function technique has been proposed. In contrast, here we numerically simulate the proposed method using fixed parameters and present a random number taken from a uniform distribution for the noise term. Based on previous results, it is validated to control the system and achieve the desired saturation width. This type of control approach has been previously implemented and used for the stochastic Kuramoto-Sivashinsky equation [86].

Initiall, the authors [49] introduced spatial derivatives for the right-hand side of the KPZ equation (2.2). A discretized method was used that includes standard forward-backward differences for a cubic grid with a lattice constant Δx

$$h_i^{n+1} = h_i^n + \frac{\Delta t}{\Delta x^2}\left[\nu(h_{i+1}^n + h_{i-1}^n - 2h_i^n) + \frac{\lambda}{8}(h_{i+1}^n - h_{i-1}^n)^2\right] + \sqrt{\frac{2D}{\Delta x^d}}\sqrt{12\Delta t}\,\eta_i^n. \tag{7.3}$$

The most accurate result were obtained for Eq. (7.3) using Euler's method when $d = 1$ or $d = 2$. The results were similar and comparable to simulated results of other author [51] [95]. However, for $d = 3$, the simulation showed the limitation of this method. Based on the previous simulation results, we apply for $d = 1$ in the present numerical experiments.

7.2. The numerical method applied for the KPZ equation in 1+1 dimension

The topic of discussion is the KPZ growth in (1+1) dimensions with temporal correlation, followed by an examination of the scaling results. We review existing numerical results and compare them with our simulation results. Furthermore, we perform several numerical simulations for different diffusion coefficients ν, as well as for the nonlinear coefficient λ and for systems of larger size *L* while fixing the other parameters. All numerical results are compared with the results of previous works [49] [69] [88] [89] [90] [95] [96]. For the simulations to analyze the effect of different coefficient, we used A computer was used to analyze the effect of different coefficients, a MacBook Air 1,6 GHz Dual-Core Intel Core i5, 8 GB 2133 MHz LPDDR3 and the MATLAB R2019b software (The MathWorks, Inc., Portola Valley, CA, USA).

The simulation shows that the discretized version of the temporal correlated KPZ equation in (1+1) dimension displays numerical divergence in the effective λ regime [89], making it impossible to observe the system's evolution past a certain time limit due to singular growth. In order to prevent numerical instability, the nonlinear term is replaced by an exponentially decreasing function, as proposed by Dasgupta et al. [16]

$$f(x) \equiv \frac{1 - e^{-cx}}{c}, \tag{7.4}$$

where *c* is an adjustable parameter. Since it is fixed as 1, the different solutions for the coefficient λ of the nonlinear term can be compared. Therefore, the temporal correlated KPZ equation in (1+1) dimension is modified and takes the following form

$$h_i^{n+1} = h_i^n + \nu\frac{\Delta t}{(\Delta x)^2}[h_{i+1}^n - 2h_i^n + h_{i-1}^n] + \Delta t\frac{\lambda}{2c}\left[1 - e^{-c\left[\frac{h_{i+1}^n - h_{i-1}^n}{2\Delta x}\right]^2}\right] + \eta_i^n,$$
$$\eta_i^n = \sqrt{\frac{2D}{\Delta x^d}}\sqrt{12\Delta t}\cdot R(t). \tag{7.5}$$

In Eq. (7.6), $R(t)$ is a random number from a uniform distribution in the interval $[-1.0, +1.0]$. In our further investigations, $c = 0.1$, $d = 1$ [130] and the spatial and temporal steps are $\Delta x = 1$ and $\Delta t = 10^{-3}$, respectively. Our initial work started from flat interface at $t = 0$ with periodic boundary conditions that were used in our previous paper [97], [98] for different discretized methods.

We use random numbers in our simulations that vary between $a = -1.0$ and $b = 1.0$, and

$$R(t) = a + (b - a) \cdot rand(\Delta t, \Delta x), \tag{4.6}$$

where $rand(t1, x1)$ returns a t1 by x1 array of random numbers where $t1, \ldots, x1$ indicate the size of each dimension [98].

7.3. The impact of *a* and *b* on the surface growth

First, we investigate the morphology of the solutions to (7.5) when different lower and upper limits are applied in $R(t)$ in the noise term. The noise term values are random with different integers a and b.

$$\Delta x = 1,\ \Delta t = 10^{-3},\ \lambda = 1,\ \nu = 0.01,\ L = 1128,\ c = 0.1,\ D = 1,\ t = 100. \tag{7.7}$$

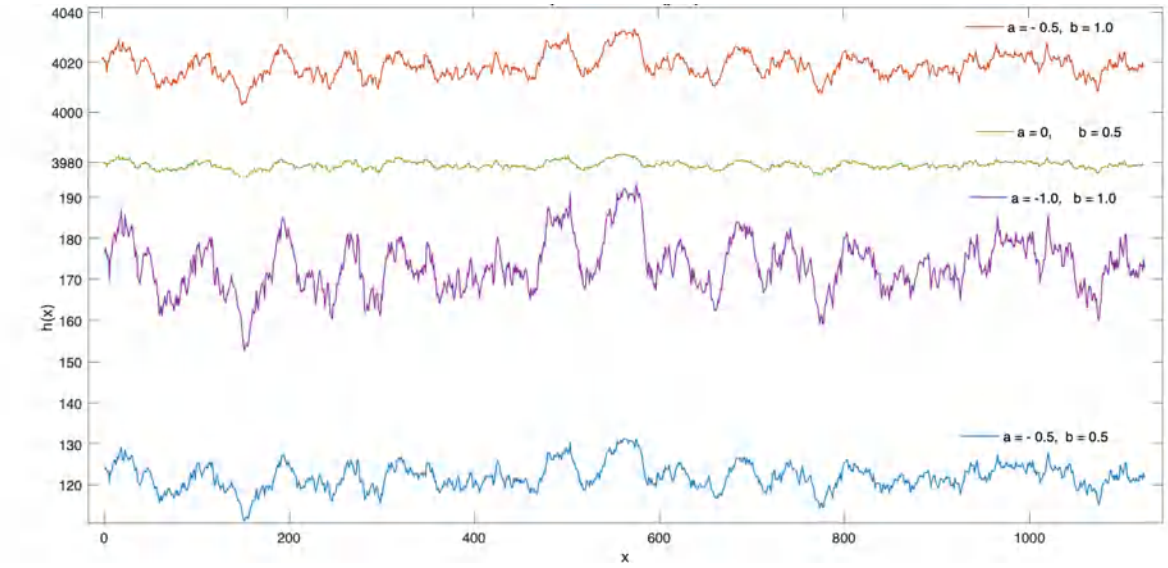

Figure 7.1. The plots of the solutions to the KPZ equation in (1+1) dimension at a growth time $t = 100$ *with parameters fixed in (7.7),* $\lambda = 1$*, and random numbers in the noise term that oscillate between* $a \in [-1.0, 0]$, $b \in [0.5, 1]$.

For different a and b, Fig. 7.1 shows the implementations for random numbers in the noise term for Eq. (7.5) with parameters fixed in (7.7). When the values of a are -0.5 or -1 and for b is 0.5 or 1, it can be seen that the height of the surface $h(x, t)$ formation is very high, reaching 4020. However, it is obvious from Fig. 7.1 that increasing the values of a and b also increases the surface roughness. For a =0 and b=0.5, we obtained the smallest roughness and for a =-1, b =1, the

roughest surface structure. We note that the application of different parameters of a and b has an effect on the surface height and it can cause sudden increase of $h(x,t)$. Fortunately, the use of the equal a and b values show relatively similar surface formation height $h(x,t)$ as in other former research papers [78] [89] [100].

In the Fig. 7.2, the surface width $W(t)$ is plotted using the Eq. (7.7) and different pairs of a and b in the noise term. It shows that an increase of $for\ |a|$ and $|b|$, increases the surface width function as does the surface roughness.

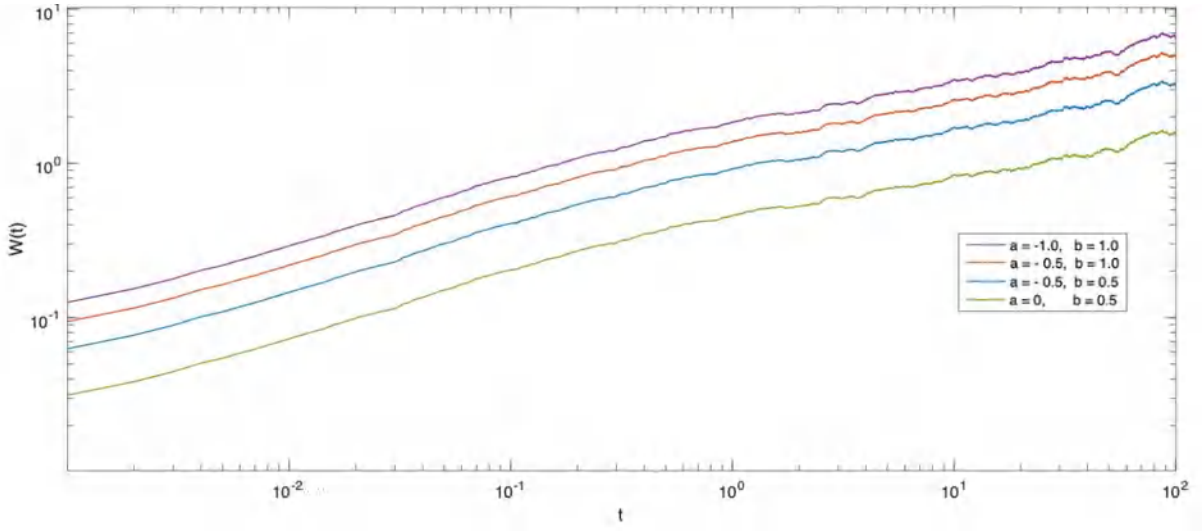

Figure 7.2. Log-log plot of the surface width $W(t)$ for parameters fixed in (7.7), $t = 100$ and the random numbers in the noise term that oscillate between $a \in [-1.0, 0]$, $b \in [0.5, 1]$.

7.4. The impact of ν and λ

The Kardar-Parisi-Zhang equation is a mathematical model that describes the behavior of randomly growing surfaces. The equation involves several parameters, including the roughness exponent (ν) and the growth exponent (λ).

In an experiment, the numerical values of ν and λ depend on the specific system being studied. There have been numerous studies on the KPZ equation in different physical systems [134-140], and the values of these parameters can vary widely depending on the experimental conditions [137].

The previous investigations of one-component growth mechanisms are based on the Kardar-Parisi-Zhang universality class [41]. The scaling exponents of metals in previous studies were found to be between 0.22 and 0.56. Studies using thermal evaporation sources gave consistent scaling exponents of about 0.25 for iron [138] and 0.42 for molybdenum [139]. The present study found a scaling exponent of 0.3, which is in agreement with the scaling exponents for sputter-deposited gold and molybdenum films. However, these values are larger than 0.25, which were predicted by the KPZ equation for the 2+1 system [134] [135].

Other studies have found different values of ν and λ in different systems. For instance, in a study of bacterial colonies, the roughness exponent was found to be around 0.5, while the growth exponent was around 1.25 [136]. In a study of electrodeposition, the roughness exponent was found to be around 0.8, while the growth exponent was around 1.5 [137].

Overall, the values of ν and λ in real experiments depend on the specific physical system being studied and the experimental conditions. The KPZ equation has been found to be a useful tool for describing the behavior of growing surfaces in a wide range of systems, and further studies are needed to better understand the relationship between the KPZ parameters and the behavior of different physical systems.

In this section, various smoothing ν and nonlinear λ parameters are investigated to show how they affect on the surface morphology. The simulation results are shown for the Eq. (7.5) with following fixed parameters

$$\Delta x = 1, \;\; \Delta t = 10^{-3}, \;\; L = 1128, \;\; c = 0.1, \;\; t = 100. \qquad (7.8)$$

First, the interface profiles are plotted for the KPZ equation with different smoothening parameters ν. Figure 7.3 shows the various interface profiles for $\lambda = 1$ and $\nu = 0.01, 0.1, 0.5, 1, 2, 5, 10$. Figure 7.3 shows that the height of the interface profile decreases as the value of ν decreases. If the smoothening parameter ν is equal to 0.01, the height of surface roughness vibrating between $h(x,t) = 5500 \ldots 5700$ indicated in red in the figure. The least influenced height of the surface profile is shown in light blue ($\nu = 10$), which is below $h(x,t) = 5100$ and the smoothest compared to all other smaller parameters.

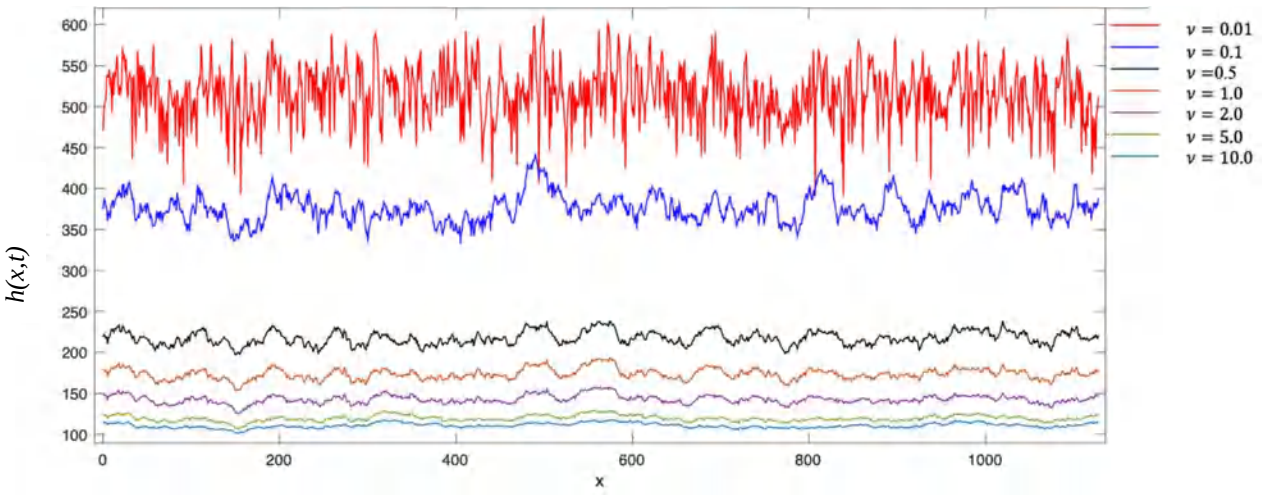

Figure 7.3. The shape of the KPZ equation in (1+1) dimension at the time of growth is studied $t = 100, \lambda = 1$ *and fixed parameters (7.8) for various parameters of* ν $(0.01, 0.1, 0.5, 1, 2, 5, 10)$.

The surface width function is presented on a log-log graph in Fig 7.4. Here, we fixed all the parameters as in (7.8) and keep changing the value of smoothening term ν from 0.01 to 10. Initially, each simulated result starts from the same point but during the time t they behave

DOI: 10.14750/ME.2023.031

differently according to variety of the parameter ν. In the Fig. 7.4, the red line shows the highest width $W(t)$ in $\nu = 0.01$ that presents slightly curved line in the end. At the same time, it can be seen that increase of parameter ν decreases the width $W(t)$. However, the roughness of the lines is different that it is smoothy $\nu = 0.01$ and rough $\nu = 10$, respectively. Figure 4 also indicates that the slope of the function $W(t)$ agrees well with $t^{\frac{1}{3}}$ in the literature.

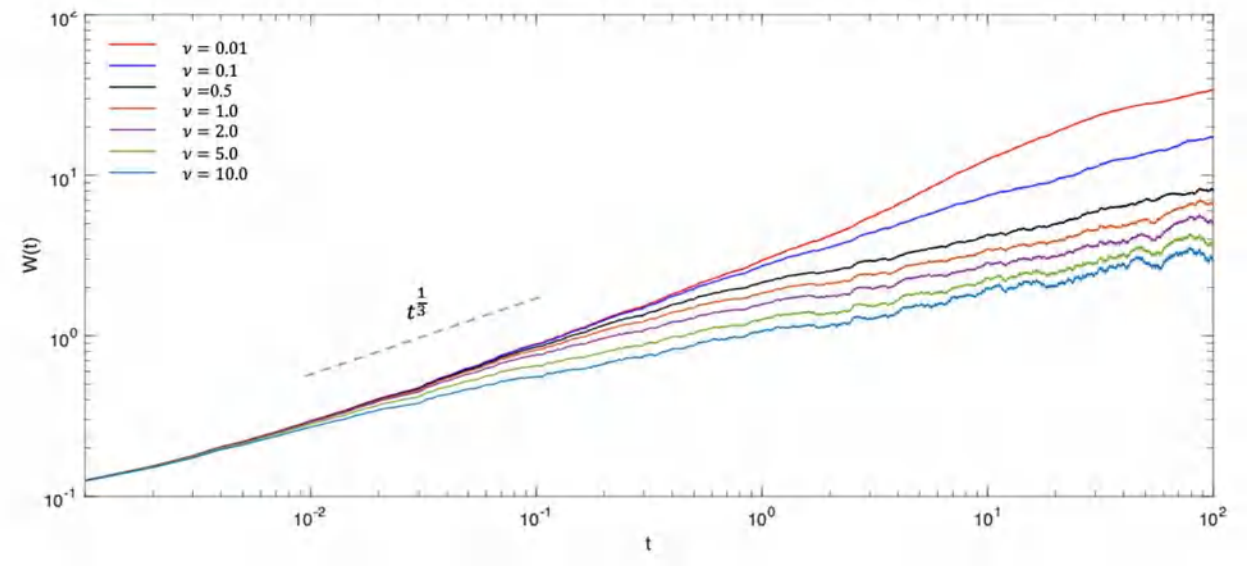

Figure 7.4. Log-log plot of the surface width $W(t)$ for fixed parameters (7.8), $\lambda = 1$ and $t = 100$. The parameter ν is between 0.01 and 10.0.

Figure 7.5 exhibits the plots of height $h(x)$ for various parameters λ of the nonlinear term ranging from 0.01 to 10. All the results obtained are obtained with a fixed smoothing parameter ν=0.01. Note that when ν is larger than 0.01, anomalous surface formation appears for different values of λ. However, the other fixed parameters were given in (7.8). When λ and ν are chosen to be equal, i.e., 0.01, the height of the interface profile h(x) is the lowest, as shown in Fig. 7.5 . The height of the interface profile $h(x)$ is uniformly oscillating. However, as the value of the nonlinear term λ increases, the surface roughness also increases and reaches the maximum value $h(x) = 1.2 \cdot 10^4$ for λ=10.

DOI: 10.14750/ME.2023.031

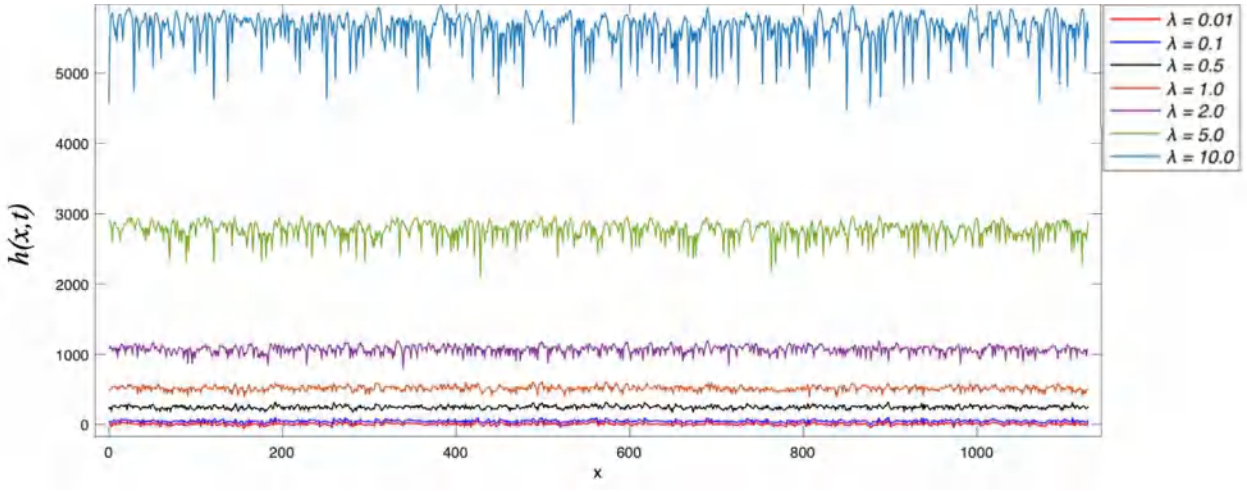

Figure 7.5. The shape of the KPZ equation in (1+1) dimension at the time of growth is studied $t = 100$, *ν=0.01 and parameters in (7.8) for parameters of* $\lambda = 0.01, 0.1, 0.5, 1, 2, 5, 10$.

Fig. 7.6 presents log-log plot of the surface width $W(t)$ for fixed values of Eq. (7.8) and ν=0.01. It is similar to the Fig. 7.4 that initial point of all simulated results is started from the same points and increase till the certain time t. When the values of λ and ν are close/the same to each other, the interface width $W(t)$ is resemble too. However, increasing the value of nonlinear term λ, increase the interface width $W(t)$. It is obvious from the Fig. 7.6 that the highest curved and light blue (malibu) colored line represents the highest value of λ that equals to 10. Figure 7.6 also indicates that the slope of the function $W(t)$ agrees well with $t^{\frac{1}{3}}$ in the literature.

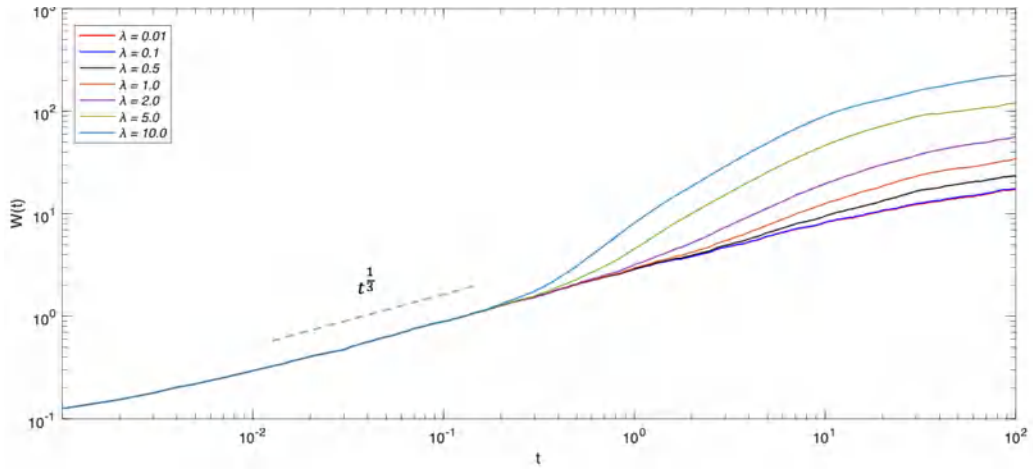

Figure 7.6. Log-log plot of the surface width $W(t)$ *for parameters (7.8), time* $t = 100$ *and ν=0.01. The parameter of* λ *is between 0.01 and 10.0.*

7.5. The impact of t on the slope of $W(t)$

To examine and compare the slope of the function $W(t)$, three different time periods $t = 10$, 100 and 500 are chosen. All the parameters in (7.8) are fixed except for the time and the value of the smoothing term ν. The Fig. 7.7 shows the slope results relation to the different values of the

smoothing term ν, that is from 0.01, 0.05, 0.1, 0.5 … to 10. As it is presented in Fig. 7.7, the highest slope value that above 0.6 is obtained when the time was $t = 10$ for $\nu = 0.01$. It is shown by the blue line with circle. However, the values of slope significantly decreased till $\nu = 2$ then it continued decreasing smoothly. Consequently, the second highest slope is obtained when the time was $t = 100$ with the slope value between 0.55 and 0.6 and it is represented by the red starred line in the figure. Similarly, the above-mentioned behavior happened here too but it should be noted that slope values are higher for $t = 100$ than $t = 10$. Interestingly, the longest time that was $t = 500$ showed fluctuated result between 0.35 and 0.5 for along the ν values. It is illustrated by black line and "×"

Our examination of the slope of $W(t)$ shows that as t increases, the numerical results come closer and closer to the theoretical value of 1/3. For small t the slope is less than 1/3.

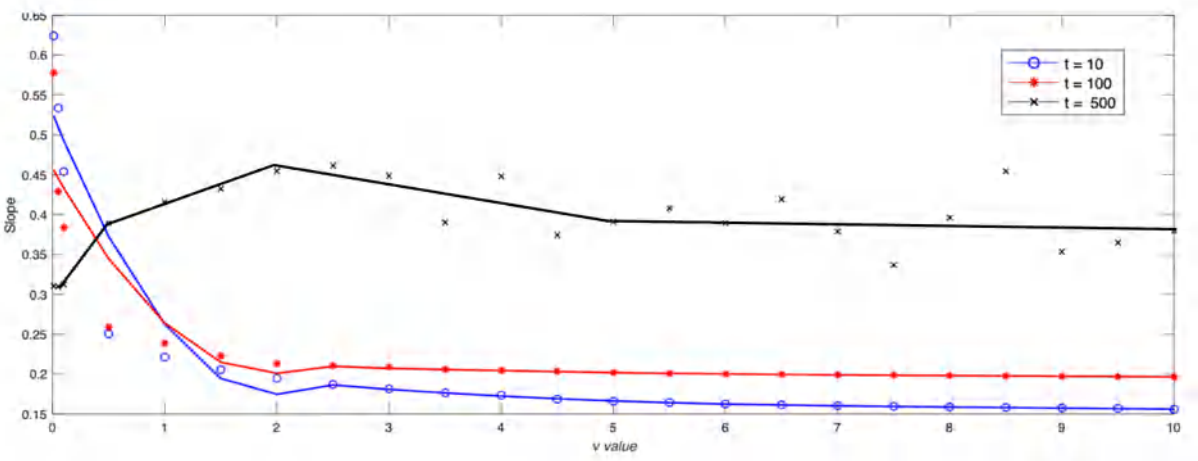

Figure 7.7. The width function's slope for the values of $\nu = (0.01, 0.05, 0.1, 0.5 \ldots 10)$ $t = 10, 100, 500$ *for the fixed* $\lambda = 1$. *All other parameters are given in (7.8).*

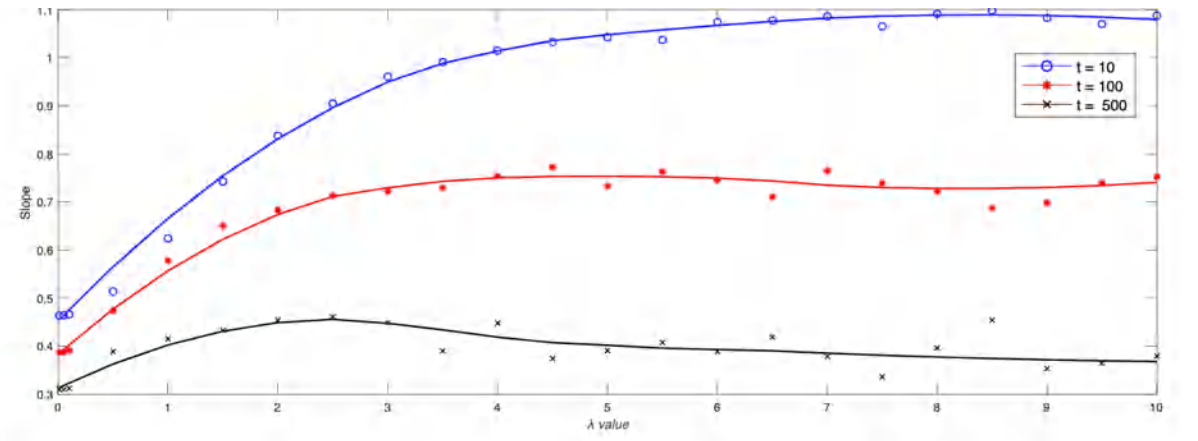

Figure 7.8. The width function's slope for different values of λ $(0.01, 0.05, 0.1, 0.5 \ldots 10)$ *in various time length* $t = 10, 100, 500$ *for the fixed* $\nu = 0.01$. *All other used parameters are given in the Eq. (7.8).*

DOI: 10.14750/ME.2023.031

In Fig. 7.8, the slope of $W(t)$ is plotted for different nonlinear term values λ $(0.01, 0.05, 0.1, 0.5$ ... $10)$ and time lengths $t = 10, 100$ and 500. It is shown that the highest slope belong to the smallest time $t = 10$. It starts at 0.45 and increases significantly to 1.2 then levels off. Figure 7.8 shows that the near-constant slope decreases with increasing time t.

7.6. The impact of L

Figure 7.9 shows the data obtained for different sizes of L lengths between 128 and 1024. These were obtained with a simulation run time of $t = 10^4, \lambda = 1, \nu = 1$. In all cases we started with a flat surface at t = 0. The data obtained for the (1+1)-dimensional KPZ equation confirm the Vicsek and Family scaling (7.2) for systems of different L sizes.

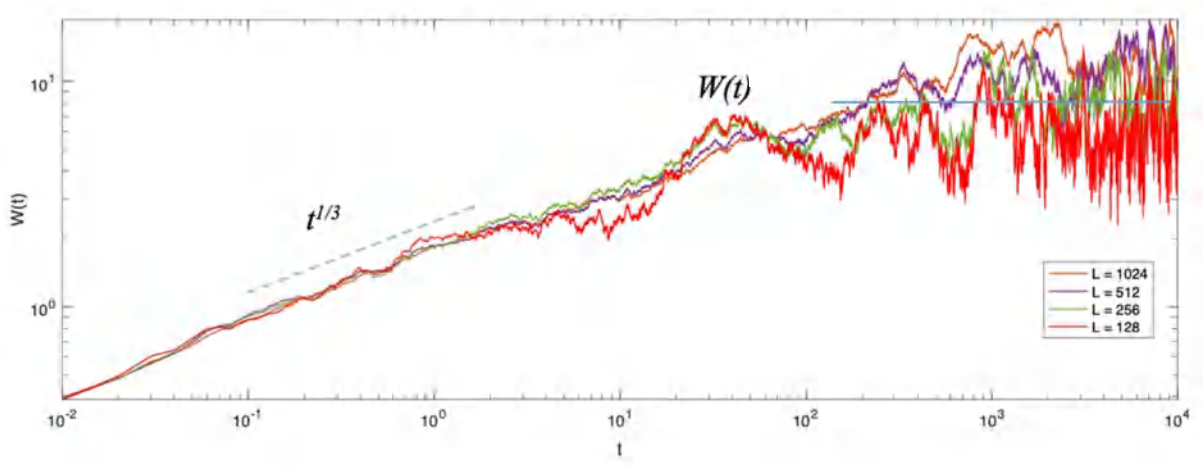

Figure 7.9. The log-log plot of width function in different linear system sizes L between 128 and 1024. Here, fixed parameters are: $\Delta x = 1, \Delta t = 10^{-2}, \lambda = 1, \nu = 1,\ c = 0.1, t = 10^4$. *The dashed line shows a power-low with exponent 1/3.*

Figure 7.9 shows four independent numerical simulation for various length L and this different linear system size L affects the slope of the width function. shows that the different linear system size L affects the slope of the width function. We started our numerical simulation with a system size of L = 1024, which is indicated in brown. The initial point of the line increases steadily, but after a certain time t oscillation started. When we reduce the system size L to 128, denoted by red, the oscillation starts early and the magnitude of the oscillation is at its maximum.

The impact of the random values in the noise term, the two parameters, a and b, on the surface growth of the 1+1 dimensional KPZ equation described by Eq. (7.6) in the presence of noise with different lower and upper limits in $R(t)$ is investigated. The results, shown in Figs. 7.1 and 7.2, demonstrate that increasing the values of a and b increases the surface roughness, and that the use of equal values of a and b results in relatively similar surface formation heights as compared to results of other researchers.

Moreover, the slope of the width function $W(t)$ is analyzed using simulations at different values of time ($t = 10$, 100, and 500), smoothing term (ν), and nonlinear term (λ). The results

indicate that as t increases, the numerical results of the slope of $W(t)$ approximates well the theoretical value $1/3$ which confirms the Vicsek and Family scaling. Figures 7.7 and 7.8 show the relationship between different time lengths and smoothing/nonlinear term values and their effect on the slope of $W(t)$. The effect of different linear system sizes (L) on the slope of the width function is given. The simulation shows that as L decreases, the oscillation starts earlier and is more pronounced.

7.7. Investigations in (1+1) dimension

The impact of long-range temporal correlations on the surface morphology is studied by examining Equation (7.1). The spatial step is $\Delta x = 1$ [55]. Here, the lattice size L used in the numerical integration has the values $L = 1128$ [59]. In Eq. (7.6), R is a random number taken from a uniform distribution from the interval $[0.5, +0.5]$.

Figures 7.10 and 7.11 illustrate the instable growth in different time t when Eq. (7.2) is simulated with $v = 1/2$, $\lambda = 1$, and $c = 0.1$, in one dimensional interface with $L = 1128$. Here, time increases from $t = 1.0, 2.0, 5.0\ to\ 10.0$ (with $\Delta t = 0.05$).

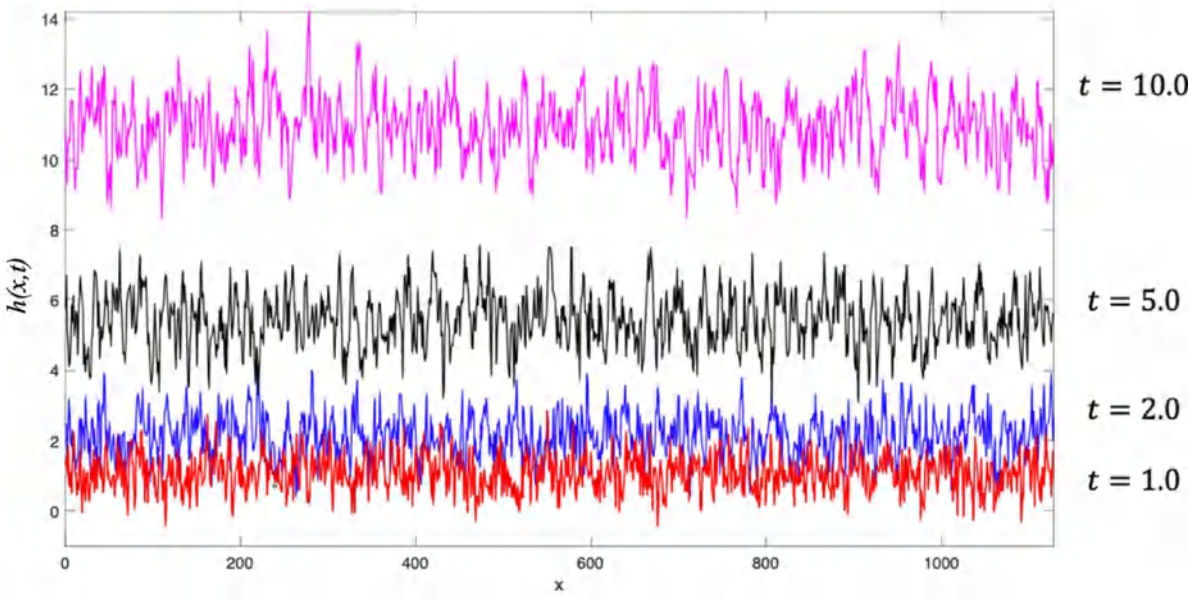

Figure 7.10. Numerical simulation results of Eq. (7.1) in different time from t = 1.0 to t = 10.0.

Figure 7.10 shows the result of the numerical simulation for different time t. When the time increases, the surface height also increases. However, we would like to point out that the amplitude of the surface formation also increases and shows a rougher surface.

DOI: 10.14750/ME.2023.031

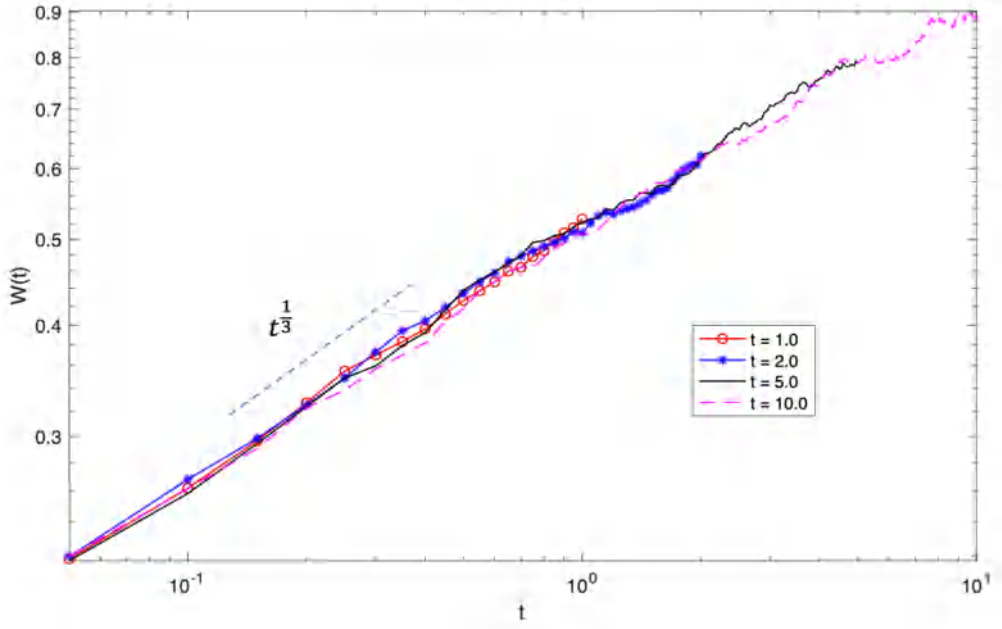

Figure 7.11. The log-log plots of thee surface roughness $W(t) = \sqrt{\langle [h(x,t) - \langle h \rangle] \rangle}$ *for different time values. Red circle lines present the result for t = 1.0, blue asterisk lines indicate the time t = 2.0. Black line and dashed magenta lines indicate the time t = 5.0.*

Figure 7.11 shows the increase in surface roughness with time. The total width $W(t)$ is plotted for different time t, and as time increases, the height of the interface also increases. Note that the amplitude of the KPZ equation increases with increasing time.

We numerically simulated KPZ equation in 1+1 dimension with a random noise term from a uniform distribution in the interval $[0.5, +0.5]$. It is confirmed that the appearance of instability exists, and the surface formation varies with the length of time. The simulation results show that when t final is increased from $t = 1.0$ to $t = 10.0$ the height of results shifted to upper position. We can conclude that the instability of the discretized KPZ equation is affected by different time effects.

DOI: 10.14750/ME.2023.031

NEW SCIENTIFIC RESULTS OF THE THESES

The main contributions from the research can be summarised as follows:

I. I analyzed the numerical solutions to the one-dimensional KPZ equation using MATLAB with various initial condition amplitudes a and noise terms. The results showed that noise terms produced similar surface shapes regardless of the initial condition amplitude, and the presence of Gaussian noise is not observable at high initial conditions amplitude.
I investigated three power-law-type noises w^n with exponents of $-1, 0, 1$, called pink, white and blue noise, respectively, and including Gaussian and Lorentzian noises. In order to observe and better understand certain physical phenomena, I used the data obtained from these experiments and validated a mathematical model [121]. Decreasing initial condition amplitude and noise term strength for the KPZ equation resulted smoother surface structure [S1, S2, S3].

II. I examined KPZ equation in one spatial dimension using the leapfrog–hopscotch (LH), standard forward time centered space (FTCS) scheme and the Heun methods. All methods are verified with analytical solution from [95] at $t = 1$ as the initial condition and the Dirichlet boundary conditions. I showed that the average and the maximum differences of the methods, namely the FTCS, the Heun and the LH with two different time step sizes Δt. I found that FTCS and the Heun's methods are usually unstable above $\Delta t = 2 \times 10^{-5}$ (the concrete threshold for stability depends on the parameters such as ν, λ, a and Δt), while the LH method was stable in all numerical experiments. It can be unstable only if the nonlinear term λ are much higher than the linear coefficient ν and there are spike-like pillars or grooves. Therefore, even if the LH method is not unconditionally stable for the KPZ equation, it is obvious that it has much better stability properties than the conventional explicit methods [S4].

III. I compared the impact of Gaussian and Brownian noises for the solutions of KPZ equation for various coefficients such as: ν, λ, a and t. I simulated two different noise terms with different parameters like linear, nonlinear and noise term amplitude. The effect of each applied parameter presented and discussed below:
When the noise term amplitude is set to $a = 1$, the Brownian noise term has a greater effect than the Gaussian noise term.

- Increasing the simulation time t_{fin} from 1 to 10 showed that the effect of the Brownian noise term remains stronger than the Gaussian noise term, even at higher noise amplitudes.
- I also examined the impact of parameters ν and λ on the method. When the diffusion term's value is high at ν = 3.0 and the nonlinear term has a low value at λ = 0.1 the surface shape closely resembles a sine wave.
- The Brownian noise term is affected by the increased linear term parameter ν, while the Gaussian noise term remains unchanged [S4].

IV. I discussed and numerically simulated the growth height of the KPZ equation using numerical method proposed by Dasgupta et al. [16]. I used random numbers $R(t)$ as a noise term that vary between $a = -1.0$ and $b = 1.0$. I found out that increasing the values of a and b increases the surface roughness. Consequently, the equal values of a and b results in relatively similar surface formation heights comparing to other researchers [80, 105]. In addition, I compared and investigated impacts of linear, nonlinear term parameters and different time to the height of the function. I got that increase of ν decreases oscillation level but increase the height of the function. In contrast, $\lambda = 0.01 \ldots 10.0$ and time $t = 1.0 \ldots 10.0$ increase the surface roughness [S6].

V. I investigated impacts of ν linear, λ nonlinear parameters and time t to the surface width $W(t)$. I got that increase of ν that decrease surface width but oscillation level rised. The impact of t on the slope of the surface width $W(t)$ for ν and $\lambda = (0.01, 0.05, 0.1, 0.5 \ldots 10)$ simulated and calculated. The numerical results of the slope of surface width $W(t)$ approximates well to the theoretical value $1/3$ which confirms the Vicsek and Family scaling for systems of different sizes. We showed the relationship between different time lengths and smoothing/nonlinear term values and their effect on the surface slope of $W(t)$. The effect of different linear system sizes (L) on the slope of the surface width function is given. The simulation shows that as L decreases, the oscillation starts earlier and is more pronounced [S6].

DOI: 10.14750/ME.2023.031

ACKNOWLEDGEMENTS

While I have made efforts, the achievement of this thesis primarily relies on the guidance and support of several individuals. Thus, I would like to express my appreciation to those who played a vital role in its completion.

My supervisor dear Prof. Dr. Gabriella Vadászné Bognár and second family in Hungary, I would like to express my sincere gratitude for your invaluable guidance, advice, dynamic spirit, support and friendship. This research would not have been possible without your assistance. Your wisdom, diligence, and passion for research have taught me so much. It was an honor to work under your supervision, and I am grateful to have met and collaborated with you. Your contribution has enabled me to acquire a wealth of experience and enhance my research aptitude for the future.

I would like to express my gratitude to my family and daughters, who have been with me and provided unwavering support throughout the years. Without their encouragement, I would not have been able to reach this point, and thus, this thesis is dedicated to them. Additionally, I extend a special thanks to my dear parents, friends who served as a beacon of hope during my prolonged absence.

DOI: 10.14750/ME.2023.031

REFERENCES

[1] M. Kardar, G. Parisi, Y.-C. Zhang, *Dynamic Scaling of Growing Interfaces*, Phys. Rev. Lett., vol. 56, no. 9, pp. 889–892, 1986, doi: 10.1103/PhysRevLett.56.889.

[2] T. Halpin-Healy, Y.-C. Zhang, *Kinetic roughening phenomena, stochastic growth, directed polymers and all that. Aspects of multidisciplinary statistical mechanics*, Physics reports, vol. 254, no. 4–6, pp. 215–414, 1995, https://doi.org/10.1016/0370-1573(94)00087-J

[3] P. Meakin, *The growth of rough surfaces and interface*, Physics Reports, vol. 235, no. 4–5, pp. 189–289, 1993, doi: 10.1016/0370-1573(93)90047-H.

[4] O. Sayfidinov, G. Bognar, *Review on Relationship Between the Universality Class of the Kardar-Parisi-Zhang Equation and the Ballistic Deposition Model*, International Journal of Applied Mechanics and Engineering, vol. 26, no. 4, pp. 206–216, 2021, doi: 10.2478/ijame-2021-0060.

[5] J. G. Amar, F. Family, *Numerical solution of a continuum equation for interface growth in 2+ 1 dimensions*, Physical Review A, vol. 41, no. 6, p. 3399, 1990, https://doi.org/10.1103/PhysRevA.41.3399.

[6] K. Moser, J. Kertész, D. E. Wolf, *Numerical solution of the Kardar-Parisi-Zhang equation in one, two and three dimensions*, Physica A: Statistical Mechanics and its Applications, vol. 178, no. 2, pp. 215–226, 1991, https://doi.org/10.1016/0378-4371(91)90017-7.

[7] K. Moser, D. E. Wolf, *Vectorized and parallel simulations of the Kardar-Parisi-Zhang equation in 3+ 1 dimensions*, Journal of Physics A: Mathematical and General, vol. 27, no. 12, p. 4049, 1994, doi: 10.1088/0305-4470/27/12/013.

[8] M. S. Li, *Surface growth with spatially correlated noise*, Phys. Rev. E, vol. 55, no. 1, pp. 1178–1180, Jan. 1997, doi: 10.1103/PhysRevE.55.1178.

[9] H. Jeong, B. Kahng, D. Kim, *Anisotropic Surface Growth Model in Disordered Media*, Phys. Rev. Lett., vol. 77, no. 25, pp. 5094–5097, 1996, doi: 10.1103/PhysRevLett.77.5094.

[10] Y. Tu, G. Grinstein, M. A. Muñoz, *Systems with Multiplicative Noise: Critical Behavior from KPZ Equation and Numerics*, Phys. Rev. Lett., vol. 78, no. 2, pp. 274–277, 1997, doi: 10.1103/PhysRevLett.78.274.

[11] C. Jayaprakash, F. Hayot, R. Pandit, *Universal properties of the two-dimensional Kuramoto-Sivashinsky equation*, Phys. Rev. Lett., vol. 71, no. 1, pp. 12–15, 1993, doi: 10.1103/PhysRevLett.71.12.

[12] J. Li, L. M. Sander, *Scaling properties of the kuramoto-sivashinsky equation*, Fractals, vol. 03, no. 03, pp. 507–514, 1995, doi: 10.1142/S0218348X95000436.

[13] M. Rost, J. Krug, *Coarsening of surface structures in unstable epitaxial growth*, Phys. Rev. E, vol. 55, no. 4, pp. 3952–3957, 1997, doi: 10.1103/PhysRevE.55.3952.

[14] T. J. Newman, A. J. Bray, *Strong-coupling behaviour in discrete Kardar - Parisi - Zhang equations*, J. Phys. A: Math. Gen., vol. 29, no. 24, pp. 7917–7928, 1996, doi: 10.1088/0305-4470/29/24/016.

[15] C. Dasgupta, S. D. Sarma, J. M. Kim, *Controlled instability and multiscaling in models of epitaxial growth*, Physical Review E, vol. 54, no. 5, p. R4552, 1996, doi: https://doi.org/10.1103/PhysRevE.54.R4552.

[16] C. Dasgupta, J. M. Kim, M. Dutta, S. Das Sarma, *Instability, intermittency, and multiscaling in discrete growth models of kinetic roughening*, Phys. Rev. E, vol. 55, no. 3, pp. 2235–2254, 1997, doi: 10.1103/PhysRevE.55.2235.

[17] C.-H. Lam, F. G. Shin, *Anomaly in numerical integrations of the Kardar-Parisi-Zhang equation*, Phys. Rev. E, vol. 57, no. 6, pp. 6506–6511, Jun. 1998, doi: 10.1103/PhysRevE.57.6506.

[18] J. G. Amar, F. Family, *Deterministic and stochastic surface growth with generalized nonlinearity*, Phys. Rev. E, vol. 47, no. 3, pp. 1595–1603, 1993, doi: 10.1103/PhysRevE.47.1595.

[19] H. S. Wio, J. A. Revelli, R. R. Deza, C. Escudero, M. S. de La Lama, *Discretization-related issues in the KPZ equation: Consistency, Galilean-invariance violation, and fluctuation--dissipation relation*, Phys. Rev. E, vol. 81, no. 6, p. 066706, 2010, doi: 10.1103/PhysRevE.81.066706.

[20] H. S. Wio, M. A. Rodríguez, R. Gallego, J. A. Revelli, A. Alés, R. R. Deza, *d-Dimensional KPZ Equation as a Stochastic Gradient Flow in an Evolving Landscape: Interpretation and Time Evolution of Its Generating Functional*, Front. Phys., vol. 4, 2017, doi: 10.3389/fphy.2016.00052.

[21] H. S. Wio, M. A. Rodríguez, R. Gallego, *Variational approach to KPZ: Fluctuation theorems and large deviation function for entropy production*, Chaos, vol. 30, no. 7, p. 073107, 2020, doi: 10.1063/5.0006121.

[22] O. Niggemann, U. Seifert, *The Two Scaling Regimes of the Thermodynamic Uncertainty Relation for the KPZ-Equation*, J Stat Phys, vol. 186, no. 1, p. 3, 2022, doi: 10.1007/s10955-021-02845-8.

[23] C. Cartes, E. Tirapegui, R. Pandit, M. Brachet, *The Galerkin-truncated Burgers equation: crossover from inviscid-thermalized to Kardar–Parisi–Zhang scaling*, Phil. Trans. R. Soc. A., vol. 380, no. 2219, p. 20210090, 2022, doi: 10.1098/rsta.2021.0090.

[24] T. J. Oliveira, *Surface growth on tree-like lattices and the upper critical dimension of the KPZ class*, EPL, vol. 133, no. 2, p. 28001, 2021, doi: 10.1209/0295-5075/133/28001.

[25] S. W. Robertson, R. O. Ritchie, *In vitro fatigue–crack growth and fracture toughness behavior of thin-walled superelastic Nitinol tube for endovascular stents: A basis for defining the effect of crack-like defects*, Biomaterials, vol. 28, no. 4, pp. 700–709, 2007, doi: 10.1016/j.biomaterials.2006.09.034.

[26] M. R. Jedwab, C. O. Clerc, *A study of the geometrical and mechanical properties of a self-expanding metallic stent—theory and experiment*, J. App. Biomater., vol. 4, no. 1, pp. 77–85, 1993, doi: 10.1002/jab.770040111.

[27] S. Logothetidis *et al.*, *Novel nanostructured biomaterials: implications for coronary stent thrombosis*, IJN, p. 6063, Dec. 2012, doi: 10.2147/IJN.S34320.

[28] Z.-W. Lai, S. Das Sarma, *Kinetic growth with surface relaxation: Continuum versus atomistic models*, Phys. Rev. Lett., vol. 66, no. 18, pp. 2348–2351, 1991, doi: 10.1103/PhysRevLett.66.2348.

[29] A. L. Barabási, H. E. Stanley, *Fractal concepts in surface growth.* Cambridge university press. Cambridge-New York-Melbourne, 1995.

[30] G. Hu, G. Orkoulas, P. D. Christofides, *Modeling and control of film porosity in thin film deposition*, Chemical Engineering Science, vol. 64, no. 16, pp. 3668–3682, 2009, doi: 10.1016/j.ces.2009.05.008.

[31] G. Ritter *et al.*, *Recent Developments in Thin Film Research: Epitaxial Growth and Nanostructures, Electron Microscopy and X-Ray Diffraction*, 1st ed., vol. 69. Strasbourg, 1998.

[32] W. A. Tiller, *The science of crystallization: macroscopic phenomena and defect generation.* Cambridge University Press, Cambridge-New York-Melbourne, 1991.

[33] P. G. Vekilov, J. I. D. Alexander, *Dynamics of Layer Growth in Protein Crystallization*, Chem. Rev., vol. 100, no. 6, pp. 2061–2090, 2000, doi: 10.1021/cr9800558.

[34] K. A. Jackson, *Kinetic processes: crystal growth, diffusion, and phase transitions in materials*. Weinheim, Wiley-VCH, Chichester, 2004.

[35] A. A. Chernov, T. Nishinaga, *Growth shapes and their stability at anisotropic interface kinetics: theoretical aspects for solution growth*, in Morphology of Crystals, Tokyo: Terra Science Publishers, 1987, pp. 207–267.

[36] Y. Saito, *Statistical physics of crystal growth.* World Scientific. Singapore-New Jersey-London-Hong Kon, 1996.

[37] A. Pimpinelli, J. Villain, *Physics of crystal growth.* Cambridge University Press, Cambridge-New York-Melbourne, 1999. https://doi.org/10.1017/CBO9780511622526

[38] T. Michely, J. Krug, *Islands, mounds and atoms.*, vol. 42. Springer Science & Business Media, Springer-Verlag, Berlin-Heidelberg-New York, 2012.

[39] J.-N. Aqua, I. Berbezier, L. Favre, T. Frisch, A. Ronda, *Growth and self-organization of SiGe nanostructures*, Physics Reports, vol. 522, no. 2, pp. 59–189, 2013, doi: 10.1016/j.physrep.2012.09.006.

[40] M. J. Vold, *A numerical approach to the problem of sediment volume*, Journal of Colloid Science, vol. 14, no. 2, pp. 168–174, 1959, doi: 10.1016/0095-8522(59)90041-8.

[41] I. Corwin, *The kardar–parisi–zhang equation and universality class*, Random Matrices: Theory Appl., vol. 01, no. 01, p. 1130001, 2012, doi: 10.1142/S2010326311300014.

[42] C. A. Tracy, H. Widom, *Level-spacing distributions and the Airy kernel*, Commun.Math. Phys., vol. 159, no. 1, pp. 151–174, 1994, doi: 10.1007/BF02100489.

[43] C. A. Tracy, H. Widom, *On orthogonal and symplectic matrix ensembles*, Commun.Math. Phys., vol. 177, no. 3, pp. 727–754, 1996, doi: 10.1007/BF02099545.

[44] J. Villain, *Continuum models of crystal growth from atomic beams with and without desorption*, J. Phys. I France, vol. 1, no. 1, pp. 19–42, Jan. 1991, doi: 10.1051/jp1:1991114.

[45] T. Hwa, M. Kardar, *Avalanches, hydrodynamics, and discharge events in models of sandpiles*, Phys. Rev. A, vol. 45, no. 10, pp. 7002–7023, 1992, doi: 10.1103/PhysRevA.45.7002.

[46] M. Marsili, A. Maritan, F. Toigo, and J. R. Banavar, *Stochastic growth equations and reparametrization invariance*, Rev. Mod. Phys., vol. 68, no. 4, pp. 963–983, 1996, doi: 10.1103/RevModPhys.68.963.

[47] C.-H. Lam, L. M. Sander, *Inverse method for interface problems*, Phys. Rev. Lett., vol. 71, no. 4, pp. 561–564, 1993, doi: 10.1103/PhysRevLett.71.561.

[48] S.-C. Park, D. Kim, J.-M. Park, *Derivation of continuum stochastic equations for discrete growth models*, Phys. Rev. E, vol. 65, no. 1, p. 015102, 2001, doi: 10.1103/PhysRevE.65.015102.

[49] Z. Rácz, M. Siegert, D. Liu, M. Plischke, *Scaling properties of driven interfaces: Symmetries, conservation laws, and the role of constraints*, Phys. Rev. A, vol. 43, no. 10, pp. 5275–5283, 1991, doi: 10.1103/PhysRevA.43.5275.

[50] M. Předota, M. Kotrla, *Stochastic equations for simple discrete models of epitaxial growth*, Phys. Rev. E, vol. 54, no. 4, pp. 3933–3942, 1996, doi: 10.1103/PhysRevE.54.3933.

[51] G. Costanza, *Langevin equations and surface growth*, Phys. Rev. E, vol. 55, no. 6, pp. 6501–6506, 1997, doi: 10.1103/PhysRevE.55.6501.

[52] P. Bántay, I. M. Jánosi, *Avalanche dynamics from anomalous diffusion*, Phys. Rev. Lett., vol. 68, no. 13, pp. 2058–2061, 1992, doi: 10.1103/PhysRevLett.68.2058.

[53] Á. Corral, A. Díaz-Guilera, *Symmetries and fixed point stability of stochastic differential equations modeling self-organized criticality*, Phys. Rev. E, vol. 55, no. 3, pp. 2434–2445, 1997, doi: 10.1103/PhysRevE.55.2434.

[54] T. Tokihiro, D. Takahashi, J. Matsukidaira, J. Satsuma, *From Soliton Equations to Integrable Cellular Automata through a Limiting Procedure*, Phys. Rev. Lett., vol. 76, no. 18, pp. 3247–3250, 1996, doi: 10.1103/PhysRevLett.76.3247.

[55] T. Nagatani, *From ballistic deposition to the Kardar-Parisi-Zhang equation through a limiting procedure*, Phys. Rev. E, vol. 58, no. 1, pp. 700–703, 1998, doi: 10.1103/PhysRevE.58.700.

[56] M. R. Wilby, D. D. Vvedensky, A. Zangwill, *Erratum: Scaling in a solid-on-solid model of epitaxial growth*, Phys. Rev. B, vol. 47, no. 23, pp. 16068–16068, 1993, doi: 10.1103/PhysRevB.47.16068.

[57] C. A. Haselwandter D. D. Vvedensky, *Scaling of ballistic deposition from a Langevin equation*, Phys. Rev. E, vol. 73, no. 4, p. 040101, 2006, doi: 10.1103/PhysRevE.73.040101.

[58] D. D. Vvedensky, *Edwards-Wilkinson equation from lattice transition rules*, Phys. Rev. E, vol. 67, no. 2, p. 025102, 2003, doi: 10.1103/PhysRevE.67.025102.

[59] S. F. Edwards D. R. Wilkinson, *The surface statistics of a granular aggregate*, Proc. R. Soc. Lond. A, vol. 381, no. 1780, pp. 17–31, 1982, doi: 10.1098/rspa.1982.0056.

[60] E. Katzav M. Schwartz, *What is the connection between ballistic deposition and the Kardar-Parisi-Zhang equation?*, Phys. Rev. E, vol. 70, no. 6, p. 061608, 2004, doi: 10.1103/PhysRevE.70.061608.

[61] J. ed. Neyman, *Proceedings of the Fourth Berkeley Symposium on Mathematical Statistics and Probability.*, vol. 4. University of California Press, Berkeley-Los Angelos, 1961, https://doi.org/10.1002/bimj.19640060422.

[62] B. B. Mandelbrot, B. B. Mandelbrot, *The fractal geometry of nature.*, vol. 1. New York: W.H. Freeman, San Francisco,1982, https://doi.org/10.2307/2323761.

[63] F. Family, T. Vicsek, *Scaling of the active zone in the Eden process on percolation networks and the ballistic deposition model*, J. Phys. A: Math. Gen., vol. 18, no. 2, pp. L75–L81, 1985, doi: 10.1088/0305-4470/18/2/005.

[64] R. Jullien, R. Botet, *Surface Thickness in the Eden Model*, Phys. Rev. Lett., vol. 54, no. 18, pp. 2055–2055, 1985, doi: 10.1103/PhysRevLett.54.2055.

[65] P. Meakin, P. Ramanlal, L. M. Sander, R. C. Ball, *Ballistic deposition on surfaces*, Phys. Rev. A, vol. 34, no. 6, pp. 5091–5103, 1986, doi: 10.1103/PhysRevA.34.5091.

[66] P. Freche, D. Stauffer, H. E. Stanley, *Surface structure and anisotropy of Eden clusters*, J. Phys. A: Math. Gen., vol. 18, no. 18, pp. L1163–L1168, 1985, doi: 10.1088/0305-4470/18/18/009.

[67] R. Hirsch, D. E. Wolf, *Anisotropy and scaling of Eden clusters in two and three dimensions*, J. Phys. A: Math. Gen., vol. 19, no. 5, pp. L251–L256, 1986, doi: 10.1088/0305-4470/19/5/007.

[68] P. Meakin, *Universal scaling properties of ballistic deposition and Eden growth on surfaces*, J. Phys. A: Math. Gen., vol. 20, no. 16, pp. L1113–L1119, 1987, doi: 10.1088/0305-4470/20/16/014.

[69] T. Kriecherbauer, J. Krug, *A pedestrian's view on interacting particle systems, KPZ universality and random matrices*, J. Phys. A: Math. Theor., vol. 43, no. 40, p. 403001, 2010, doi: 10.1088/1751-8113/43/40/403001.

[70] B. Derrida, J. L. Lebowitz, *Exact Large Deviation Function in the Asymmetric Exclusion Process*, Phys. Rev. Lett., vol. 80, no. 2, pp. 209–213, 1998, doi: 10.1103/PhysRevLett.80.209.

[71] B. Derrida, C. Appert, *Universal Large-Deviation Function of the Kardar Parisi Zhang Equation in One Dimension*. Journal of statistical physics 94, (1999): 1-30.

[72] D.-S. Lee, D. Kim, *Large deviation function of the partially asymmetric exclusion process*, Phys. Rev. E, vol. 59, no. 6, pp. 6476–6482, 1999, doi: 10.1103/PhysRevE.59.6476.

[73] E. Brunet, B. Derrida, *Microscopic models of traveling wave equations*, Computer Physics Communications, vol. 121–122, pp. 376–381, 1999, doi: 10.1016/S0010-4655(99)00358-6.

[74] D. Stauffer, *Cumulant Ratios of Eden Model Surfaces in 1+1 Dimensions*, Int. J. Mod. Phys. C, vol. 09, no. 07, pp. 1033–1039, 1998, doi: 10.1142/S0129183198000972.

[75] T. Halpin-Healy, Y.-C. Zhang, *Kinetic roughening phenomena, stochastic growth, directed polymers and all that. Aspects of multidisciplinary statistical mechanics*, Physics Reports, vol. 254, no. 4–6, pp. 215–414, 1995, doi: 10.1016/0370-1573(94)00087-J.

[76] M. Myllys, J. Maunuksela, M. Alava, T. Ala-Nissila, J. Merikoski, J. Timonen, *Kinetic roughening in slow combustion of paper*. Physical Review E, *64*(3), 2001. p.036101. doi: 10.1103/PhysRevE.64.036101

[77] C. Appert, *Large deviation function for the Eden model and universality within the one-dimensional Kardar-Parisi-Zhang class*, Phys. Rev. E, vol. 61, no. 2, pp. 2092–2094, 2000, doi: 10.1103/PhysRevE.61.2092.

[78] D. Forster, D. R. Nelson, M. J. Stephen, *Large-distance and long-time properties of a randomly stirred fluid*, Phys. Rev. A, vol. 16, no. 2, pp. 732–749, 1977, doi: 10.1103/PhysRevA.16.732.

[79] H. van Beijeren, R. Kutner, H. Spohn, *Excess Noise for Driven Diffusive Systems*, Phys. Rev. Lett., vol. 54, no. 18, pp. 2026–2029, 1985, doi: 10.1103/PhysRevLett.54.2026.

[80] J. Krug, H. Spohn, *Kinetic roughening of growing interface*, in In Solids far from Equilibrium: Growth, Morphology and Defects, Boston, MA: Cambridge University Press, Cambridge-New York-Melbourne, 1992, pp. 479–582.

[81] H. Spohn, *KPZ Scaling Theory and the Semi-discrete Directed Polymer Model*, 2012, doi: 10.48550/ARXIV.1201.0645.

[82] D. A. Huse, C. L. Henley, D. S. Fisher, *Huse, Henley, and Fisher respond*, Phys. Rev. Lett., vol. 55, no. 26, pp. 2924–2924, 1985, doi: 10.1103/PhysRevLett.55.2924.

[83] Th. M. Nieuwenhuizen, *Trapping and Lifshitz Tails in Random Media, Self-Attracting Polymers, and the Number of Distinct Sites Visited: A Renormalized Instanton Approach in Three Dimensions*, Phys. Rev. Lett., vol. 62, no. 4, pp. 357–360, 1989, doi: 10.1103/PhysRevLett.62.357.

[84] H. K. Janssen, B. Schmittmann, *Field theory of long time behaviour in driven diffusive systems*, Z. Physik B - Condensed Matter, vol. 63, no. 4, pp. 517–520, 1986, doi: 10.1007/BF01726201.

[85] V. Yakhot, Z.-S. She, *Long-time, large-scale properties of the random-force – driven Burgers equation*, Phys. Rev. Lett., vol. 60, no. 18, pp. 1840–1843, 1988, doi: 10.1103/PhysRevLett.60.1840.

[86] S. Zaleski, *A stochastic model for the large scale dynamics of some fluctuating interfaces*, Physica D: Nonlinear Phenomena, vol. 34, no. 3, pp. 427–438, 1989, doi: 10.1016/0167-2789(89)90266-2.

[87] F. W. Olver, D. W. Lozier, R. F. Boisvert, C. W. Clark, *NIST handbook of mathematical functions.* Cambridge university press, Cambridge-New York-Melbourne, 2010.

[88] C. C. Battaile, *The Kinetic Monte Carlo method: Foundation, implementation, and application*, Computer Methods in Applied Mechanics and Engineering, vol. 197, no. 41–42, pp. 3386–3398, 2008, doi: 10.1016/j.cma.2008.03.010.

[89] D. Sergi, A. Camarano, J. M. Molina, A. Ortona, J. Narciso, *Surface growth for molten silicon infiltration into carbon millimeter-sized channels: Lattice–Boltzmann simulations, experiments and models*, Int. J. Mod. Phys. C, vol. 27, no. 06, p. 1650062, 2016, doi: 10.1142/S0129183116500625.

[90] E. A. Rodrigues, B. A. Mello, F. A. Oliveira, *Growth exponents of the etching model in high dimensions*, J. Phys. A: Math. Theor., vol. 48, no. 3, p. 035001, 2015, doi: 10.1088/1751-8113/48/3/035001.

[91]I. F. Barna, G. Bognár, L. Mátyás, M. Guedda, K. Hriczó, *Analytic solutions of the two-dimensional Kardar-Parisi-Zhang growing equation*, AIP Conference Proceedings 2293, 280002, 2020.

[92]G Bognár, I. F. Barna, K Hriczó, *Investigation of roughening in nonlinear surface evaluation models*, AIP Conference Proceedings 2293, 280004, 2020.

[93]I. F. Barna, G. Bognár, L. Mátyás, M. Guedda, K. Hriczó, *Travelling-wave solutions of the Kardar-Parisi-Zhang interface growing equation with different kind of noise terms*, AIP Conference Proceedings 2293, 280005, 2020.

[94]G. Bognár, M. Guedda, K. Hriczó, L. Taourirte, *Instabilities in certain one-dimensional singular interfacial equation*, Physica Scripta vol. 95 no. 3, 035001, 2020.

[95] I. F. Barna, G. Bognár, M. Guedda, L. Mátyás, K. Hriczó, *Analytic self-similar solutions of the Kardar-Parisi-Zhang interface growing equation with various noise terms*, Mathematical Modelling and Analysis, vol. 25, no. 2, pp. 241–256, 2020, doi: 10.3846/mma.2020.10459.

[96] I. F. Barna, G. Bognár, M. Guedda, K. Hriczó, L. Mátyás, *Analytic traveling-wave solutions of the Kardar-Parisi-Zhang interface growing equation with different kind of noise terms*, Springer Proceedings in Mathematics and Statistics, vol. 333, 2020, pp. 239–253. doi: 10.1007/978-3-030-56323-3_19.

[97] F. M. Weiss, F. B. Madsen, T. Töpper, B. Osmani, V. Leung, B. Müller, *Molecular beam deposition of high-permittivity polydimethylsiloxane for nanometer-thin elastomer films in dielectric actuators*, Materials & Design, vol. 105, pp. 106–113, 2016, doi: 10.1016/j.matdes.2016.05.049.

[98] J.-O. Carlsson, P. M. Martin, *Chemical Vapor Deposition*, in Handbook of Deposition Technologies for Films and Coatings, Noyes publications, Park Ridge, New Jersey, William andrew publishing, LLC, Norwich, New York, 2010, pp. 314–363. doi: 10.1016/B978-0-8155-2031-3.00007-7.

[99] A. L.-S. Chua, C. A. Haselwandter, C. Baggio, D. D. Vvedensky, *Langevin equations for fluctuating surfaces*, Phys. Rev. E, vol. 72, no. 5, p. 051103, 2005, doi: 10.1103/PhysRevE.72.051103.

[100] E. Korutcheva, *Advances in Condensed Matter and Statistical Physics*. Nova Publishers, Nova Science Pub Inc, Hauppauge-New York, 2004.

[101] G. Bognár, *Roughening in Nonlinear Surface Growth Model*, Applied Sciences, vol. 10, no. 4, p. 1422, 2020, doi: 10.3390/app10041422.

[102] R. G. da Silva, M. L. Lyra, C. R. da Silva, G. M. Viswanathan, *Roughness scaling and sensitivity to initial conditions in a symmetric restricted ballistic deposition model*, Eur. Phys. J. B, vol. 17, no. 4, pp. 693–697, 2000, doi: 10.1007/s100510070110.

[103] M. Inc, *The approximate and exact solutions of the space- and time-fractional Burgers equations with initial conditions by variational iteration method*, Journal of Mathematical Analysis and Applications, vol. 345, no. 1, pp. 476–484, 2008, doi: 10.1016/j.jmaa.2008.04.007.

[104] I. A. Bukharev, J. M. Kosterlitz, *Influence of initial conditions on KPZ growth*, p. H33.04, 1996, 1996APS..MAR.H3304B.

[105] Y. T. Fukai, K. A. Takeuchi, *Kardar-Parisi-Zhang Interfaces with Curved Initial Shapes and Variational Formula*, Phys. Rev. Lett., vol. 124, no. 6, p. 060601, 2020, doi: 10.1103/PhysRevLett.124.060601.

[106] B. Meerson, P. V. Sasorov, A. Vilenkin, *Nonequilibrium steady state of a weakly-driven Kardar–Parisi–Zhang equation*, J. Stat. Mech., vol. 2018, no. 5, p. 053201, 2018, doi: 10.1088/1742-5468/aabbcc.

[107] I. Corwin, P. Ghosal, *KPZ equation tails for general initial data*, Electron. J. Probab., vol. 25, no. none, 2020, doi: 10.1214/20-EJP467.

[108] I. Corwin, P. Ghosal, *Lower tail of the KPZ equation*, Duke Math. J., vol. 169, no. 7, 2020, doi: 10.1215/00127094-2019-0079.

[109] E. Frey, U. C. Täuber, T. Hwa, *Mode-coupling and renormalization group results for the noisy Burgers equation*, Phys. Rev. E, vol. 53, no. 5, pp. 4424–4438, 1996, doi: 10.1103/PhysRevE.53.4424.

[110] J. Quastel, H. Spohn, *The One-Dimensional KPZ Equation and Its Universality Class*, J Stat Phys, vol. 160, no. 4, pp. 965–984, 2015, doi: 10.1007/s10955-015-1250-9.

[111] M. Hoshino, *KPZ equation with fractional derivatives of white noise*, Stoch PDE: Anal Comp, vol. 4, no. 4, pp. 827–890, 2016, doi: 10.1007/s40072-016-0078-x.

[112] D. Squizzato, L. Canet, *Kardar-Parisi-Zhang equation with temporally correlated noise: A nonperturbative renormalization group approach*, Phys. Rev. E, vol. 100, no. 6, p. 062143, 2019, doi: 10.1103/PhysRevE.100.062143.

[113] H. C. Fogedby, *Kardar-Parisi-Zhang equation in the weak noise limit: Pattern formation and upper critical dimension*, Phys. Rev. E, vol. 73, no. 3, p. 031104, 2006, doi: 10.1103/PhysRevE.73.031104.

[114] P. Le Doussal, *Crossover between various initial conditions in KPZ growth: flat to stationary*, J. Stat. Mech., vol. 2017, no. 5, p. 053210, 2017, doi: 10.1088/1742-5468/aa6f3e.

[115] S. Prolhac, H. Spohn, *Height distribution of the Kardar-Parisi-Zhang equation with sharp-wedge initial condition: Numerical evaluations*, Phys. Rev. E, vol. 84, no. 1, p. 011119, 2011, doi: 10.1103/PhysRevE.84.011119.

[116] T. Sasamoto, H. Spohn, *Exact height distributions for the KPZ equation with narrow wedge initial condition*, Nuclear Physics B, vol. 834, no. 3, pp. 523–542, 2010, doi: 10.1016/j.nuclphysb.2010.03.026.

[117] C. Cosco, S. Nakajima, M. Nakashima, *C. Cosco, S. Nakajima, and M. Nakashima, 'Law of large numbers and fluctuations in the sub-critical and regions L^2 for SHE and KPZ equation in dimension $d \geq 3$*. arXiv, 26, 2020. Accessed: 25, 2022. [Online]. Available: http://arxiv.org/abs/2005.

[118] S. Chhita, P. L. Ferrari, H. Spohn, *Limit distributions for KPZ growth models with spatially homogeneous random initial conditions*, Ann. Appl. Probab., vol. 28, no. 3, 2018, doi: 10.1214/17-AAP1338.

[119] T. Sasamoto, *Spatial correlations of the 1D KPZ surface on a flat substrate*, J. Phys. A: Math. Gen., vol. 38, no. 33, pp. L549–L556, 2005, doi: 10.1088/0305-4470/38/33/L01.

[120] J. Baik and Z. Liu, *Periodic TASEP with general initial conditions*, Probab. Theory Relat. Fields, vol. 179, no. 3–4, pp. 1047–1144, 2021, doi: 10.1007/s00440-020-01004-6.

[121] M. Lässig, *On growth, disorder, and field theory*, J. Phys.: Condens. Matter, vol. 10, no. 44, pp. 9905–9950, 1998, doi: 10.1088/0953-8984/10/44/003.

[122] O. Sayfidinov, G. V. Bognár, *Numerical Solutions of the Kardar-Parisi-Zhang Interface Growing Equation with Different Noise Terms*, in Vehicle and Automotive Engineering 3, K. Jármai and K. Voith, Eds. Singapore: Springer Singapore, 2021, pp. 302–311. doi: 10.1007/978-981-15-9529-5_27.

[123] O. Sayfidinov, G. Bognar, *One Dimensional Kardar-Parisi-Zhang Equation in Various Initial Condition Amplitudes*, J. Adv. App. Comput. Math., vol. 7, pp. 32–37, 2020, doi: 10.15377/2409-5761.2020.07.5.

[124] O. Sayfidinov, G. Bognár, E. Kovács, *Solution of the 1D KPZ Equation by Explicit Methods*, Symmetry, vol. 14, no. 4, p. 699, 2022, doi: 10.3390/sym14040699.

[125] Á. Nagy, I. Omle, H. Kareem, E. Kovács, I. F. Barna, G. Bognar, *Stable, Explicit, Leapfrog-Hopscotch Algorithms for the Diffusion Equation*, Computation, vol. 9, no. 8, p. 92, 2021, doi: 10.3390/computation9080092.

[126] U. M. Ascher, L. R. Petzold, *Computer Methods for Ordinary Di erential Equations and Di erential-Algebraic Equations*, Library of Congress Cataloging-in-Publication Data, Philadelphia, 1998.

[127] E. Kovács, Á. Nagy, M. Saleh, *A Set of New Stable, Explicit, Second Order Schemes for the Non-Stationary Heat Conduction Equation*, Mathematics, vol. 9, no. 18, p. 2284, 2021, doi: 10.3390/math9182284.

[128] J. Muñoz-Matute, V. M. Calo, D. Pardo, E. Alberdi, K. G. van der Zee, *Explicit-in-time goal-oriented adaptivity*, Computer Methods in Applied Mechanics and Engineering, vol. 347, pp. 176–200, 2019, doi: 10.1016/j.cma.2018.12.028.

[129] P. Gordon, *Nonsymmetric Difference Equations*, Journal of the Society for Industrial and Applied Mathematics, vol. 13, no. 3, pp. 667–673, Sep. 1965, doi: 10.1137/0113044.

[130] A. R. Gourlay, *Hopscotch: a Fast Second-order Partial Differential Equation Solver*, IMA J Appl Math, vol. 6, no. 4, pp. 375–390, 1970, doi: 10.1093/imamat/6.4.375.

[131] M. Saleh, E. Kovács, *New Explicit Asymmetric Hopscotch Methods for the Heat Conduction Equation*, in The 1st International Electronic Conference on Algorithms, 2021, p. 22. doi: 10.3390/IOCA2021-10902.

[132] Á. Nagy, M. Saleh, I. Omle, H. Kareem, E. Kovács, *New Stable, Explicit, Shifted-Hopscotch Algorithms for the Heat Equation*, MCA, vol. 26, no. 3, p. 61, 2021, doi: 10.3390/mca26030061.

[133] O. Sayfidinov, G. Bognár, *Kardar-Parisi-Zhang interface growing equation with different noise terms*, presented at the International conference of numerical analysis and applied mathematics ICNAAM 2020, Rhodes, Greece, 2022, p. 290006. doi: 10.1063/5.0081584.

[134] G. Ódor, B. Liedke KH. Heinig, *Directed d-mer diffusion describing the Kardar-Parisi-Zhang-type surface growth*. Physical Review E. 2010 Mar 12;81(3):031112. https://doi.org/10.1103/PhysRevE.81.031112

[135] A. Halperin, , A. Buhot, Y. Zhong, M. Kardar, Interface roughening, growth exponents, and the Kardar-Parisi-Zhang equation. Physical Review E, 1995. 52(2), R1277–R1280. https://doi.org/10.1103/PhysRevE.52.R1277

[136] E. Ben-Jacob, I. Cohen, I. Golding, D. L. Gutnick, M. Tcherpakov, *Generic modelling of cooperative growth patterns in bacterial colonies*. Nature, 1994. 368(6466), 46–49. https://doi.org/10.1038/368046a0

[137] J. Chevrier, V. Le Thanh, R. Buys, and J. Derrien. *A RHEED study of epitaxial growth of iron on a silicon surface: experimental evidence for kinetic roughening*. Europhysics Letters 16, no. 8 (1991): 737 . https://doi.org/10.1209/0295-5075/16/8/006

[138] Y-L. He, H-N. Yang, T-M. Lu, G. C. Wang. *Measurements of dynamic scaling from epitaxial growth front: Fe film on Fe (001).* Physical review letters 69, no. 26 (1992): 3770 https://doi.org/10.1103/PhysRevLett.69.3770

[139] J. Wang, G. Li, P. Yang, M. Cui, X. Jiang, B. Dong, H. Liu. *X-ray reflectivity and scanning-tunneling-microscopy study of surface roughness scaling of molybdenum films*. Europhysics Letters 42, no. 3 (1998): 283. https://doi.org/10.1209/epl/i1998-00243-1

[140] R. Mustafa, Ayhan Elmali, E. Thomas, F. Hartmut, H. Horst. *Evolution of the surface roughness (dynamic scaling) and microstructure of sputter-deposited Ag75Co25 granular films.* Journal of Physics: Condensed Matter 12, no. 44 (2000): 9237 https://doi.org/10.1088/0953-8984/12/44/306

DOI: 10.14750/ME.2023.031

LIST OF PUBLICATIONS RELATED TO THE TOPIC OF THE RESEARCH FIELD

S1. [4] O. Sayfidinov, G. Bognar, *Review on Relationship Between the Universality Class of the Kardar-Parisi-Zhang Equation and the Ballistic Deposition Model*, International Journal of Applied Mechanics and Engineering, vol. 26, no. 4, pp. 206–216, 2021, doi: 10.2478/ijame-2021-0060.

S2. [118] O. Sayfidinov, G. V. Bognár, *Numerical Solutions of the Kardar-Parisi-Zhang Interface Growing Equation with Different Noise Terms*, in Vehicle and Automotive Engineering 3, K. Jármai and K. Voith, Eds. Singapore: Springer Singapore, 2021, pp. 302–311. doi: 10.1007/978-981-15-9529-5_27.

S3. [119] O. Sayfidinov, G. Bognar, *One Dimensional Kardar-Parisi-Zhang Equation in Various Initial Condition Amplitudes*, J. Adv. App. Comput. Math., vol. 7, pp. 32–37, 2020, doi: 10.15377/2409-5761.2020.07.5.

S4. [120] O. Sayfidinov, G. Bognár, E. Kovács, *Solution of the 1D KPZ Equation by Explicit Methods*, Symmetry, vol. 14, no. 4, p. 699, 2022, doi: 10.3390/sym14040699.

S5. [129] O. Sayfidinov, G. Bognár, *Kardar-Parisi-Zhang interface growing equation with different noise terms*, presented at the International conference of numerical analysis and applied mathematics ICNAAM 2020, Rhodes, Greece, 2022, p. 290006. doi: 10.1063/5.0081584.

S6. O. Sayfidinov, G. Bognár, *Dynamics of surface roughening in 1+1 dimensional Kardar-Parisi-Zhang growth with a random noise term*. Submitted to the journal.

DOI: 10.14750/ME.2023.031

CONFERENCES

1. Vehicle and Automotive Engineering 3, Numerical Solutions of the Kardar-Parisi-Zhang Interface Growing Equation with Different Noise term, October 23-25, 2020, University of Miskolc, Hungary
2. ICNAAM 2020, 18th International Conference of Numerical Analysis and Applied Mathematics. Kardar-Parisi-Zhang Interface Growing Equation with Different Noise Terms, September 17-23, 2020, Rhodes, Greece
3. 36th Conference of Machine and Product Designers, Review on universality class of the Kardar-Parisi-Zhang equation, November 5-6, 2020, University of Miskolc, Hungary
4. II. International Conference on Mathematics and Its Applications in Science and Engineering (ICMASE 2021), Numerical Simulation of the Improved Kardar-Parisi-Zhang DiscretizationEquation with Gaussian Noise Term, July 1-2, 2021, Salamanca, Spain
5. ICNAAM 2021, 19th International Conference of Numerical Analysis and Applied Mathematics. The Impact of Noise Terms on Solutions of the Kardar-Parisi-Zhang Equation, September 20-26, 2021, Rhodes, Greece
6. The 17th Miklós Iványi PhD & DLA Symposium: Comparison of Numerical Simulations using Different Discretizations for the Kardar-Parisi-Zhang Equation, 25th-26th October, 2021, University of Pecs, Hungary
7. 37th Conference of Machine and Product Designers, Numerical simulation of discretized kardar-parisi-zhang equation with gaussian noise term, November 4-5, 2021, University of Miskolc, Hungary
8. ICNAAM 2022, 20th International Conference of Numerical Analysis and Applied Mathematics. Random noise term effect on discretized Kardar-Parisi-Zhang equation, September 19-24, 2021, Heraklion, Crete, Greece